



**UNIVERSIDAD DE INVESTIGACION DE  
TECNOLOGÍA EXPERIMENTAL YACHAY**

**Escuela de Ciencias Físicas y Nanotecnología**

**TÍTULO: Density-functional theory studies on the diamond surfaces  
and effect of hydrogenation and surface carbon vacancies on the  
atomic and electronic structure**

Trabajo de integración curricular presentado como requisito para la  
obtención del título de Físico

**Autor:**

Narváez Adams Roberth Mateo

**Tutor:**

Pinto Esperanza Henry Paul, Ph.D.

**Co-Tutor:**

Jani Mona, Ph.D.

Urcuquí, julio de 2021

**SECRETARÍA GENERAL**  
**(Vicerrectorado Académico/Cancillería)**  
**ESCUELA DE CIENCIAS FÍSICAS Y NANOTECNOLOGÍA**  
**CARRERA DE FÍSICA**  
**ACTA DE DEFENSA No. UITEY-PHY-2021-00016-AD**

A los 25 días del mes de junio de 2021, a las 11:00 horas, de manera virtual mediante videoconferencia, y ante el Tribunal Calificador, integrado por los docentes:

<b>Presidente Tribunal de Defensa</b>	Dra. GONZALEZ VAZQUEZ, GEMA , Ph.D.
<b>Miembro No Tutor</b>	Dr. MOWBRAY , DUNCAN JOHN , Ph.D.
<b>Tutor</b>	Dr. PINTO ESPARZA, HENRY PAUL , Ph.D.

El(la) señor(ita) estudiante **NARVAEZ ADAMS, ROBERTH MATEO**, con cédula de identidad No. **0401557129**, de la **ESCUELA DE CIENCIAS FÍSICAS Y NANOTECNOLOGÍA**, de la Carrera de **FÍSICA**, aprobada por el Consejo de Educación Superior (CES), mediante Resolución **RPC-SO-39-No.456-2014**, realiza a través de videoconferencia, la sustentación de su trabajo de titulación denominado: **Density-functional theory studies on the diamond surfaces and effect of hydrogenation and surface carbon vacancies on the atomic and electronic structure**, previa a la obtención del título de **FÍSICO/A**.

El citado trabajo de titulación, fue debidamente aprobado por el(los) docente(s):

<b>Tutor</b>	Dr. PINTO ESPARZA, HENRY PAUL , Ph.D.
--------------	---------------------------------------

Y recibió las observaciones de los otros miembros del Tribunal Calificador, las mismas que han sido incorporadas por el(la) estudiante.

Previamente cumplidos los requisitos legales y reglamentarios, el trabajo de titulación fue sustentado por el(la) estudiante y examinado por los miembros del Tribunal Calificador. Escuchada la sustentación del trabajo de titulación a través de videoconferencia, que integró la exposición de el(la) estudiante sobre el contenido de la misma y las preguntas formuladas por los miembros del Tribunal, se califica la sustentación del trabajo de titulación con las siguientes calificaciones:

Tipo	Docente	Calificación
Presidente Tribunal De Defensa	Dra. GONZALEZ VAZQUEZ, GEMA , Ph.D.	10,0
Tutor	Dr. PINTO ESPARZA, HENRY PAUL , Ph.D.	10,0
Miembro Tribunal De Defensa	Dr. MOWBRAY , DUNCAN JOHN , Ph.D.	9,9

Lo que da un promedio de: **10 (Diez punto Cero)**, sobre 10 (diez), equivalente a: **APROBADO**

Para constancia de lo actuado, firman los miembros del Tribunal Calificador, el/la estudiante y el/la secretario ad-hoc.

Certifico que *en cumplimiento del Decreto Ejecutivo 1017 de 16 de marzo de 2020, la defensa de trabajo de titulación (o examen de grado modalidad teórico práctica) se realizó vía virtual, por lo que las firmas de los miembros del Tribunal de Defensa de Grado, constan en forma digital.*

NARVAEZ ADAMS, ROBERTH MATEO  
**Estudiante**



Dra. GONZALEZ VAZQUEZ, GEMA , Ph.D.  
**Presidente Tribunal de Defensa**

GEMA  
**GONZALEZ VAZQUEZ**  
Digitally signed by GEMA GONZALEZ VAZQUEZ  
 Date: 2021.06.25 12:14:08 -05'00'

Dr. PINTO ESPARZA, HENRY PAUL , Ph.D.  
**Tutor**

HENRY  
**PAUL PINTO ESPARZA**  
Digitally signed by HENRY PAUL PINTO ESPARZA  
 Date: 2021.06.25 12:50:49 -05'00'

Dr. MOWBRAY , DUNCAN JOHN , Ph.D.  
**Miembro No Tutor**



Firmado electrónicamente por:  
**DUNCAN JOHN  
MOWBRAY .**

CIFUENTES TAFUR, EVELYN CAROLINA  
**Secretario Ad-hoc**

EVELYN  
CAROLINA  
CIFUENTES  
TAFUR

Digitally signed by  
EVELYN CAROLINA  
CIFUENTES TAFUR  
Date: 2021.06.25  
12:13:39 -05'00'

## **Autoría**

Yo, **Roberth Mateo Narváez Adams**, con cédula de identidad **0401557129**, declaro que las ideas, juicios, valoraciones, interpretaciones, consultas bibliográficas, definiciones y conceptualizaciones expuestas en el presente trabajo, así como los procedimientos y herramientas utilizadas en la investigación, son de absoluta responsabilidad del autor del trabajo de integración curricular. Así mismo, me acojo a los reglamentos internos de la Universidad de Investigación de Tecnología Experimental Yachay.

Urcuquí, julio del 2021.



Roberth Mateo Narváez Adams  
C.I. 0401557129

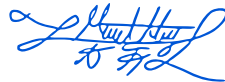


## **Autorización de publicación**

Yo, **Roberth Mateo Narváez Adams**, con cédula de identidad **0401557129**, cedo a la Universidad de Tecnología Experimental Yachay, los derechos de publicación de la presente obra, sin que deba haber un reconocimiento económico por este concepto. Declaro además que el texto del presente trabajo de titulación no podrá ser cedido a ninguna empresa editorial para su publicación u otros fines, sin contar previamente con la autorización escrita de la Universidad.

Asimismo, autorizo a la Universidad para que realice la digitalización y publicación de este trabajo de integración curricular en el repositorio virtual, de conformidad a lo dispuesto en el Art. 144 de la Ley Orgánica de Educación Superior.

Urcuquí, julio del 2021.



Roberth Mateo Narváez Adams  
C.I. 0401557129





## **Agradecimientos**

Este proyecto de investigación fue posible gracias a la guía y todo el apoyo del Dr. Henry Pinto. Me gustaría agradecerle por aceptarme en su grupo de investigación y por la oportunidad de trabajar en una investigación con una supercomputadora. Le agradezco profundamente por ser mi guía, mi profesor y mi amigo durante todo este proceso de formación profesional como científico. También, este trabajo no hubiese sido posible sin el apoyo oportuno de mi co-tutora la Dra. Mona Jani, quien con sus observaciones aportó a la mejora de esta investigación, mi agradecimiento profundo.

Agradezco a mis padres, Roberth Narváez y Olga Adams, quienes me han enseñando mis principios, han confiado en mí y me han apoyado con cada decisión que he tomado a lo largo de toda mi vida. Quiero pensar que parte de todo su esfuerzo y sacrificio está reflejado en este logro académico. Agradezco a mis hermanos, Matías y Gabriel, quienes han visto en mí un ejemplo y siempre me han motivado a seguir adelante con sus pequeñas acciones. Agradezco a mi abuela Blanca Esmeralda, por siempre preocuparse por mí y velar por mi salud a lo largo de toda mi carrera.

Además, quiero agradecer de forma especial a todos mis amigos más cercanos durante la universidad: Jennifer Sanchez, Samantha Naranjo, Eduardo Jami, Gabriela Ibarra, Diego Jimenez, Jonathan Recalde y Luis Pilicita, quienes me brindaron su apoyo y siempre me recordaron que el trabajo duro al final siempre trae grandes recompensas. Finalmente, quiero agradecerle a mi persona especial en estos últimos años, Carolina Ibarra, quién siempre confió en mí y me brindó todo su amor y compañía en todo mi transcurso por Yachay Tech.



## Resumen

Comprender las propiedades físico-químicas de las superficies de nanodiamantes (ND) es de fundamental importancia con muchas aplicaciones potenciales como administración de fármacos, nanoelectrónica molecular y semillas para hacer crecer películas delgadas de diamantes. El control atómico en la superficie ND es la clave para aplicaciones exitosas, como la administración de fármacos y la catálisis química. A continuación, presentamos un estudio de la estructura atómica y electrónica de las superficies de diamante (111) y (110). Se han realizado simulaciones de la teoría funcional de la densidad (DFT) con el fin de calcular la estructura atómica y electrónica de la estructura cristalina y las reconstrucciones de las superficies. En estos cálculos de DFT, también se empleó la polarización de espín para explorar posibles configuraciones magnéticas. Además, también proporcionamos espectros de fotoelectrones ultravioleta (UPS), imágenes simuladas de microscopía de túnel de barrido (STM) y funciones de trabajo de las superficies energéticamente más favorables. Finalmente, las superficies de los diamantes muestran interesantes propiedades electrónicas y magnéticas al interactuar con los átomos de hidrógeno.

**Palabras clave:** DFT, SCAN+rVV10, VASP, C(111), C(110), PDOS, energía de superficie, STM, UPS, función de trabajo.



## Abstract

Understanding the physical-chemical properties of nanodiamond (ND) surfaces is of fundamental importance with many potential applications as drug delivery, molecular nanoelectronics, and seeds to grow diamond thin films. Atomic control on the ND surface is the key to successful applications, such as drug delivery and chemical catalysis. Here, we present a study of the atomic and electronic structure of diamond surfaces (111) and (110). Density-functional theory (DFT) simulations have been performed in order to compute the atomic and electronic structure of bulk and surface reconstructions. In these DFT calculations, spin-polarization was also employed to explore possible magnetic configurations. Moreover, we also provide ultraviolet photoelectron spectra (UPS), simulated scanning tunneling microscopy (STM) images, and work functions of the most energetically favorable surfaces. Finally, the diamond surfaces show interesting electronic and magnetic properties on interaction with hydrogen atoms.

**Keywords:** DFT, SCAN+rVV10, VASP, C(111), C(110), PDOS, surface energy, STM, UPS, work function.



# Contents

<b>List of Figures</b>	<b>xv</b>
<b>List of Tables</b>	<b>xix</b>
<b>1 Introduction</b>	<b>1</b>
1.1 Problem Statement . . . . .	2
1.2 General and Specific Objectives . . . . .	2
<b>2 Theoretical Background</b>	<b>5</b>
2.1 Density Functional Theory . . . . .	5
2.1.1 Many-body Schrödinger equation . . . . .	5
2.1.2 Atomic units . . . . .	7
2.1.3 The Born-Oppenheimer approximation . . . . .	9
2.1.4 The independent electrons approximation . . . . .	10
2.1.5 Hartree-Fock theory . . . . .	11
2.1.6 Hohenberg-Kohn theorem . . . . .	14
2.1.7 Kohn-Sham theory . . . . .	16
2.1.8 Spin in density-functional theory . . . . .	17
2.1.9 Self-consistent calculations . . . . .	18
2.2 Exchange-correlational functionals . . . . .	19
2.2.1 The local spin-density approximation . . . . .	20
2.2.2 The generalized gradient approximation . . . . .	21
2.2.3 The meta-GGA . . . . .	21
2.3 Modelling Extended Systems . . . . .	22
2.3.1 Periodic systems . . . . .	22

2.3.2	Plane-wave expansion . . . . .	24
2.3.3	The $k$ -points mesh . . . . .	25
2.3.4	Pseudopotentials . . . . .	26
2.3.5	The projector augmented-wave method . . . . .	27
2.4	Scanning Tunneling Microscopy STM . . . . .	28
2.4.1	Working principle . . . . .	28
2.4.2	Tersoff-Hamann approximation . . . . .	29
2.5	Ultraviolet Photoelectron Spectroscopy UPS . . . . .	30
2.5.1	Working principle . . . . .	31
<b>3</b>	<b>Methodology</b>	<b>33</b>
3.1	Computational details . . . . .	33
3.2	Surface model simulations . . . . .	34
3.2.1	Crystal optimization . . . . .	34
3.2.2	Surfaces optimization . . . . .	37
<b>4</b>	<b>Results &amp; Discussion</b>	<b>43</b>
4.1	The diamond crystal . . . . .	43
4.2	The C(110) diamond surfaces . . . . .	44
4.2.1	The C(110) surface energies and electronic properties . . . . .	44
4.2.2	The C(110)-(1×1) surface . . . . .	47
4.2.3	The C(110)-(1×1)H surface . . . . .	49
4.2.4	The C(110)-(2×1)H+2H <sub>v</sub> surface . . . . .	52
4.2.5	The C(110)-(2×1)H+2H <sub>v</sub> -AFM surface . . . . .	55
4.2.6	The C(110)-(2×1)H+3H <sub>v</sub> -M1 surface . . . . .	60
4.2.7	The C(110)-(2×1)H+3H <sub>v</sub> -M2 surface . . . . .	61
4.3	The C(111) diamond surfaces . . . . .	65
4.3.1	The C(111) surface energies and electronic properties . . . . .	65
4.3.2	The C(111)-(2×1) surface . . . . .	68
4.3.3	The C(111)-(1×1)H surface . . . . .	70
<b>5</b>	<b>Conclusions &amp; Outlook</b>	<b>75</b>



<b>A</b>	<b>VASP working principle</b>	<b>77</b>
A.0.1	VASP inputs . . . . .	77
A.0.2	VASP outputs . . . . .	78
<b>B</b>	<b>bSKAN working principle</b>	<b>81</b>
B.0.1	bSKAN inputs . . . . .	81
B.0.2	bSKAN outputs . . . . .	82
<b>C</b>	<b>Input and output files examples</b>	<b>83</b>
<b>D</b>	<b>Computed work functions for all the selected surfaces</b>	<b>87</b>
<b>E</b>	<b>Computed PDOS for all the selected surfaces</b>	<b>93</b>
<b>F</b>	<b>IMFP and Cross-section used for UPS spectra simulations</b>	<b>101</b>
	<b>Bibliography</b>	<b>103</b>



# List of Figures

2.1	Jacob's ladder of density functional approximations to the exchange-correlation energy . . .	20
2.2	STM operating modes . . . . .	29
3.1	Diamond crystal structure . . . . .	34
3.2	Cut-off energy convergence plot . . . . .	35
3.3	$k$ -points mesh convergence plot . . . . .	36
3.4	Diamond crystal EOS . . . . .	37
3.5	Diamond crystal cut by the (110) and (111) cleaving planes. . . . .	38
3.6	Surface vacuum convergence plot . . . . .	39
3.7	Pristine, passivated, and hydrogenated slab example for the (110) diamond family plane. . .	42
4.1	Total and partial DOS computed with the SCAN+rVV10 functional for the fcc diamond crystal structure. . . . .	45
4.2	Surface energy diagram of the (110) surfaces structures. . . . .	46
4.3	Surface energy diagram of the most stable (110) surfaces structures. . . . .	47
4.4	Atomic and electronic structure computed with the SCAN+rVV10 functional for the C(110)-(1×1) surface structure. . . . .	48
4.5	Computed UPS spectra for the C(110)-(1×1) surface structure. . . . .	49
4.6	Computed constant current mode STM image and linescan plots for the C(110)-(1×1) surface. . . . .	50
4.7	Atomic and electronic structure computed with the SCAN+rVV10 functional for the C(110)-(1×1)H surface structure. . . . .	51
4.8	Computed UPS spectra for the C(110)-(1×1)H surface structure. . . . .	52
4.9	Computed constant current mode STM image and linescan plots for the C(110)-(1×1)H surface. . . . .	53

4.10	Atomic and electronic structure computed with the SCAN+rVV10 functional for the C(110)-(2×1)H+2H <sub>v</sub> surface structure. . . . .	54
4.11	Computed UPS spectra for the C(110)-(2×1)H+2H <sub>v</sub> surface structure. . . . .	55
4.12	Computed constant current mode STM image and linescan plots for the C(110)-(2×1)H+2H <sub>v</sub> surface. . . . .	56
4.13	Atomic and electronic structure computed with the SCAN+rVV10 functional for the C(110)-(2×1)H+2H <sub>v</sub> -AFM surface structure. . . . .	57
4.14	Computed UPS spectra for the C(110)-(2×1)H+2H <sub>v</sub> -AFM surface structure. . . . .	58
4.15	Computed constant current mode STM image and linescan plots for the C(110)-(2×1)H+2H <sub>v</sub> -AFM surface. . . . .	59
4.16	Atomic and electronic structure computed with the SCAN+rVV10 functional for the C(110)-(2×1)H+3H <sub>v</sub> -M1 surface structure. . . . .	61
4.17	Computed UPS spectra for the C(110)-(2×1)H+3H <sub>v</sub> -M1 surface structure. . . . .	62
4.18	Computed constant current mode STM image and linescan plots for the C(110)-(2×1)H+3H <sub>v</sub> -M1 surface. . . . .	63
4.19	Atomic and electronic structure computed with the SCAN+rVV10 functional for the C(110)-(2×1)H+3H <sub>v</sub> -M2 surface structure. . . . .	64
4.20	Computed UPS spectra for the C(110)-(2×1)H+3H <sub>v</sub> -M2 surface structure. . . . .	65
4.21	Computed constant current mode STM image and linescan plots for the C(110)-(2×1)H+3H <sub>v</sub> -M2 surface. . . . .	66
4.22	Surface energy diagram of the most stable (111) surfaces structures. . . . .	67
4.23	Atomic and electronic structure computed with the SCAN+rVV10 functional for the C(111)-(2×1) surface structure. . . . .	69
4.24	Computed UPS spectra for the C(111)-(2×1) surface structure. . . . .	70
4.25	Computed constant current mode STM image and linescan plots for the C(111)-(2×1) surface. . . . .	71
4.26	Atomic and electronic structure computed with the SCAN+rVV10 functional for the C(111)-(1×1)H surface structure. . . . .	72
4.27	Computed UPS spectra for the C(111)-(1×1)H surface structure. . . . .	73
4.28	Computed constant current mode STM image and linescan plots for the C(111)-(1×1)H surface. . . . .	74
C.1	INCAR file example . . . . .	83

C.2	POSCAR file example . . . . .	84
C.3	KPOINTS file example . . . . .	85
C.4	DOSCAR file example . . . . .	85
C.5	INSCAN file example . . . . .	86
D.1	Computed work function for the C(110)-(1×1) surface. . . . .	87
D.2	Computed work function for the C(110)-(1×1)H surface. . . . .	88
D.3	Computed work function for the C(110)-(1×1)H+2H <sub>v</sub> surface. . . . .	88
D.4	Computed work function for the C(110)-(1×1)H+2H <sub>v</sub> -AFM surface. . . . .	89
D.5	Computed work function for the C(110)-(1×1)H+3H <sub>v</sub> -M1 surface. . . . .	89
D.6	Computed work function for the C(110)-(1×1)H+3H <sub>v</sub> -M2 surface. . . . .	90
D.7	Computed work function for the C(111)-(2×1) surface. . . . .	90
D.8	Computed work function for the C(111)-(1×1)H surface. . . . .	91
E.1	Detailed PDOS for the C(110)-(1×1) surface. . . . .	93
E.2	Detailed PDOS for the C(110)-(1×1)H surface. . . . .	94
E.3	Detailed PDOS for the C(110)-(1×1)H+2H <sub>v</sub> surface. . . . .	95
E.4	Detailed PDOS for the C(110)-(1×1)H+2H <sub>v</sub> -AFM surface. . . . .	96
E.5	Detailed PDOS for the C(110)-(1×1)H+3H <sub>v</sub> -M1 surface. . . . .	97
E.6	Detailed PDOS for the C(110)-(1×1)H+3H <sub>v</sub> -M2 surface. . . . .	98
E.7	Detailed PDOS for the C(111)-(2×1) surface. . . . .	99
E.8	Detailed PDOS for the C(111)-(1×1)H surface. . . . .	100
F.1	Inelastic mean free path fitting. . . . .	101
F.2	Photoionization cross-section interpolations for the C and H atoms. . . . .	102



# List of Tables

4.1	Computed crystal structure and mechanical properties for fcc diamond crystal . . . . .	44
4.2	Computed work functions and bandgaps for the most stable (110) surfaces structures. . . .	46
4.3	Computed work functions and energy bandgaps for the most stable (111) surfaces structures.	68





# Chapter 1

## Introduction

The study of nanomaterials has become one of the fastest-growing fields of materials science and engineering. The manipulation of materials on a nanometric scale has made it possible to obtain new and better material properties such as fluorescence, extreme anisotropy of electrical and mechanical properties, high electron mobility, tunable band-gap, and other unique properties that have not been successfully studied at larger scales<sup>1</sup>. Thanks to all these novel properties, the use of nanomaterials in science and technology development has had a notable influence, from the miniaturization and improvement of existing technologies such as high computer performance chips to enable new technologies such as nano-based drug delivery systems<sup>2</sup>. The combination of diverse material properties with potential applications and low fabrication costs has meant that carbon nanomaterials occupy a special place in the large family of nanomaterials. Among the most famous carbon nanomaterials can be found graphene, nanotubes, nanodiamonds, and fullerenes<sup>1</sup>.

Nanodiamonds (NDs) have been recognized among the most promising materials for bio-applications due to their excellent bio-compatibility and versatility<sup>3,4</sup>. Among the most attractive characteristics of NDs stands out their capacity to be functionalized by surface modification<sup>5,6</sup>.

The lattice structure of NDs is similar to that of bulk diamond and has more frequent cubic variant phases (in some cases with an admixture of hexagonal phases). With respect to bulk diamonds, a slight shift in the lattice constant and broadening of the signals is observed when examined using various spectroscopic and crystallographic methods. Based on the size of the NDs, strain within particles and altered bonding situations close to their surface are observed. At the surface of NDs there is a large amount of highly reactive dangling bonds that causes the surface reconstruction giving rise to  $sp^2$  hybridization and graphitization. However, surface reconstruction largely depends on the method of preparation, such as detonation or shock

wave synthesis. Yet, the exact surface structure of NDs is not yet completely understood. For application purposes, surface modifications and pre-treatments are highly recommended. One of these methods is hydrogenation of the ND's surface. Hydrogenation treatments lead to a reproducible surface with large C-H bonds and prevent the formation of  $sp^2$  species by etching.

Diamond surface modifications can be studied from the experimental point of view, using some microscopic and spectroscopic techniques such as scanning tunneling microscopy (STM), ultraviolet photoelectron spectroscopy (UPS), transmission electron microscopy (TEM), and x-ray photoelectron spectroscopy (XPS).

From the theoretical point of view, diamond surface modifications can be studied using some advanced theories such as the density-functional theory (DFT), this theory is considered one of the most powerful theoretical tools for studying nanomaterials at the quantum mechanical level, allowing us to replicate experiments and providing fundamental insights<sup>7</sup>. However, to perform a DFT simulation, it is necessary to consider two essential aspects, the computational cost required to achieve the simulation and how precise results are needed<sup>8</sup>. In this sense, satisfying both previous aspects, the simulation of diamond surfaces using DFT has become an ideal option for investigating the diamond surface properties.

## **1.1 Problem Statement**

Although DFT has dramatically improved the way it performs material surface simulations over the past thirty years, diamond surface research has not been entirely explored for the theoretical modeling community. For this reason, we can find a large number of scientific publications that report new and better methods of synthesizing, characterizing, and functionalizing diamond surfaces without theoretical modeling that validates these results. It is becoming more clear—within the scientific community—that with the help of theoretical modeling, it is possible to investigate in greater depth the type of diamond surfaces that can be found in nature and could lead to the pinpointing of properties to improve characterization. For these reasons, it would be ideal to carry out a DFT study with cutting edge simulation methods to explore a wide variety of diamond surfaces that could be possible to synthesize experimentally.

## **1.2 General and Specific Objectives**

The general objective of this work is to perform a DFT study of the atomic and electronic structure of the diamond surface reconstructions with hydrogenation and carbon vacancy defects using a state-of-the-art DFT functional. For this, it is necessary to satisfy the following specific objectives:

- 
- Explain the theoretical background needed to understand how DFT performs material simulations, specifically with the state-of-the-art strongly constrained and appropriately normed semilocal density functional (SCAN) with Van der Waals corrections (rVV10).
  - Study the atomic and electronic structure of the bulk system of diamond.
  - Design the ideal methodology for the study of pristine, hydrogenated, and carbon vacancy diamond surfaces.
  - Study the atomic and electronic structure of pristine diamond surfaces (111) and (110) as well as fully hydrogenated including hydrogen and carbon vacancies.
  - Investigate possible magnetic solutions and the effect of H or C vacancies on these properties.
  - Perform STM simulation images of the most energetically favourable surfaces.
  - Perform UPS simulation spectra of the most energetically favourable surfaces.
  - Raise some conclusions and remarks about all the work done in the light of experimental evidence.



# Chapter 2

## Theoretical Background

### 2.1 Density Functional Theory

#### 2.1.1 Many-body Schrödinger equation

This chapter begins with the basic concepts of quantum mechanics and the theory of materials. It aims to study the non-relativistic interactions on atomic systems, electrons, and nuclei, in the quantum regime. For this, we have to consider the many-body Schrödinger equation, which is a handy equation to describe the motion of a quantum mechanical particle system<sup>8</sup>

$$[\hat{T} + \hat{V}] \Psi = E_{tot} \Psi \quad (2.1)$$

where  $\hat{T}$  ( $\hat{V}$ ) is the kinetic (potential) energy operator,  $E_{tot}$  is the total energy, and  $\Psi$  is the wavefunction for the many-body system. For a system of many atoms,  $N$  electrons' positions will be labeled as  $\mathbf{r}_1, \mathbf{r}_2, \dots, \mathbf{r}_N$  and  $M$  nuclei positions will be labeled as  $\mathbf{R}_1, \mathbf{R}_2, \dots, \mathbf{R}_M$ . With this notation, we can express the kinetic energy operator as<sup>8,9</sup>:

$$\hat{T} = - \sum_{i=1}^N \frac{\hbar^2}{2m_e} \nabla_i^2 - \sum_{I=1}^M \frac{\hbar^2}{2M_I} \nabla_I^2, \quad (2.2)$$

where  $\hbar$  is the reduced Planck constant,  $m_e$  is the electron mass,  $M_I$  represents the nuclei masses and  $\nabla^2$  is the Laplacian that acts with respect to each nucleus  $I$  and electron  $i$  position; in rectangular coordinates, it will be:

$$\nabla_i^2 = \frac{\partial^2}{\partial x_i^2} + \frac{\partial^2}{\partial y_i^2} + \frac{\partial^2}{\partial z_i^2}. \quad (2.3)$$

Regarding the potential energy operator, we should consider the Coulomb interactions between electrons (ee), nuclei (nn), and electron-nuclei (en)<sup>8,9</sup>. First, for the electron-electron interaction, we have a Coulomb repulsion because both charges are negative:

$$V_{ee} = \frac{1}{2} \sum_{i \neq j} \frac{e^2}{4\pi\epsilon_0} \frac{1}{|\mathbf{r}_i - \mathbf{r}_j|}, \quad (2.4)$$

where  $\epsilon_0$  is the permeability of free space,  $e$  is the electron charge and  $|\mathbf{r}_i - \mathbf{r}_j|$  is the distance between electron pairs. It is essential to mention that  $i$  should not be equal to  $j$  because there does not exist Coulomb repulsion between one electron and itself. Also, the sum is divided by two because we are considering just one contribution per electron pair.

Next, for the nuclei-nuclei interaction, also we have a Coulomb repulsion because both charges are positive:

$$V_{nn} = \frac{1}{2} \sum_{I \neq J} \frac{e^2}{4\pi\epsilon_0} \frac{Z_I Z_J}{|\mathbf{R}_I - \mathbf{R}_J|}, \quad (2.5)$$

where  $Z_I$  and  $Z_J$  are the atomic numbers of the nuclei  $I$  and  $J$ . The form of this equation is entirely similar to the previous one but with nuclei instead of electrons.

Then, for the electron-nuclei interaction, we have a Coulomb attraction because both charges are opposite:

$$V_{en} = - \sum_{i,I} \frac{e^2}{4\pi\epsilon_0} \frac{Z_I}{|\mathbf{r}_i - \mathbf{R}_I|}, \quad (2.6)$$

where  $|\mathbf{r}_i - \mathbf{R}_I|$  is the electron-nuclei distance, and the minus sign is due to the electrons' contribution.

Finally, using equation 2.1, we can obtain the full many-body Schrödinger equation<sup>8-10</sup>:

$$\left[ - \sum_{i=1}^N \frac{\hbar^2}{2m_e} \nabla_i^2 - \sum_{I=1}^M \frac{\hbar^2}{2M_I} \nabla_I^2 + \frac{1}{2} \sum_{i \neq j} \frac{e^2}{4\pi\epsilon_0} \frac{1}{|\mathbf{r}_i - \mathbf{r}_j|} + \frac{1}{2} \sum_{I \neq J} \frac{e^2}{4\pi\epsilon_0} \frac{Z_I Z_J}{|\mathbf{R}_I - \mathbf{R}_J|} - \sum_{i,I} \frac{e^2}{4\pi\epsilon_0} \frac{Z_I}{|\mathbf{r}_i - \mathbf{R}_I|} \right] \Psi = E_{tot} \Psi. \quad (2.7)$$

To discuss the many-body Schrödinger equation with all its electrons and nuclei, we should include a wavefunction containing each electron and nuclei position information, so this wavefunction is called the many-body wavefunction. Then, the wavefunction for  $N$  electrons and  $M$  nuclei will be:

$$\Psi = \Psi(\mathbf{r}_1, \mathbf{r}_2, \dots, \mathbf{r}_N; \mathbf{R}_1, \mathbf{R}_2, \dots, \mathbf{R}_M) . \quad (2.8)$$

where the probability of finding  $N$  electrons concurrently at positions  $\mathbf{r}_1, \mathbf{r}_2, \dots, \mathbf{r}_N$  respectively is given by  $|\Psi|^2$ . The electron number density, the probability of finding any electron at position  $\mathbf{r}$ , is given by<sup>8</sup>:

$$n(\mathbf{r}) = N \int |\Psi|^2 d\mathbf{r}_2 \dots d\mathbf{r}_N d\mathbf{R}_1 \dots d\mathbf{R}_M . \quad (2.9)$$

Here we have normalized the wavefunction  $\Psi$  to unity, so we have:

$$\int |\Psi|^2 d\mathbf{r}_1 \dots d\mathbf{r}_N d\mathbf{R}_1 \dots d\mathbf{R}_M = 1 . \quad (2.10)$$

Then, integrating the electron number density, we will obtain the number of electrons that the system has:

$$\int n(\mathbf{r}) d\mathbf{r} = N . \quad (2.11)$$

Now, we know all the elements that correspond to the many-body Schrödinger equation. Additionally, it is essential to mention that equation 2.7 has no analytical solution for a system of more than two particles and for real systems the numerical solution is very expensive computationally<sup>8</sup>. Thus, some approaches have been proposed to tackle the complexity barrier, such as DFT.

### 2.1.2 Atomic units

In order to simplify the full many-body Schrödinger equation, we need to consider the fundamental physical constants involved in this equation. These constants were experimentally determined and do not depend on any particular material:

$$\begin{aligned} \hbar &= 1.05457163 \cdot 10^{-34} \text{J} \cdot \text{s} , \\ m_e &= 9.10938291 \cdot 10^{-31} \text{kg} , \\ m_p &= 1.67262164 \cdot 10^{-27} \text{kg} , \\ e &= 1.60217649 \cdot 10^{-19} \text{C} , \\ \epsilon_0 &= 8.85418782 \cdot 10^{-12} \text{F/m} . \end{aligned} \quad (2.12)$$

Considering the Bohr radius  $a_0 = 0.529 \text{ \AA}$ , which is the most probable distance between the electron and proton of the hydrogen atom in its fundamental state (i.e., the peak position in the electron number

density), we can have a sense of the order of magnitudes involved in the energy calculations of equation 2.7<sup>8</sup>. In this sense, we can calculate the average Coulomb energy for an electron-proton pair (eq. 2.13) and notice that the inter-atomic interactions will give the related potential energies in Hartree units (Ha)

$$E_{\text{Ha}} = \frac{e^2}{4\pi a_0 \epsilon_0}. \quad (2.13)$$

Now, for the kinetic energies, we can consider a semi-classical argument. In the Bohr model of the Hydrogen atom, the ground-state angular momentum is given by:

$$a_0 v m_e = \hbar, \quad (2.14)$$

where  $v$  is the electron velocity.

Additionally, the balance between the centrifugal force and nuclear attraction is:

$$m_e \frac{v^2}{a_0} = \frac{e^2}{4\pi \epsilon_0 a_0^2}. \quad (2.15)$$

By combining the equations 2.14 and 2.15, we obtain the relation:

$$\frac{e^2}{4\pi a_0 \epsilon_0} = \frac{\hbar^2}{a_0^2 m_e}. \quad (2.16)$$

And, by combining the equations 2.13 and 2.15, we obtain the second relation:

$$\frac{1}{2} m_e v^2 = \frac{1}{2} E_{\text{Ha}}. \quad (2.17)$$

The two previous relationships say that kinetic energy also has the order of  $E_{\text{Ha}}$ . Acknowledging that potential and kinetic energies have the order of  $E_{\text{Ha}}$ , we can divide equation 2.7 by  $E_{\text{Ha}}$  to obtain a considerable notation simplification

$$\left[ - \sum_{i=1}^N \frac{1}{2} a_0^2 \nabla_i^2 - \sum_{I=1}^M \frac{1}{2(M_I/m_e)} a_0^2 \nabla_I^2 + \frac{1}{2} \sum_{i \neq j} \frac{a_0}{|\mathbf{r}_i - \mathbf{r}_j|} + \frac{1}{2} \sum_{I \neq J} Z_I Z_J \frac{a_0}{|\mathbf{R}_I - \mathbf{R}_J|} - \sum_{i,I} Z_I \frac{a_0}{|\mathbf{r}_i - \mathbf{R}_I|} \right] \Psi = \frac{E_{\text{tot}}}{E_{\text{Ha}}} \Psi. \quad (2.18)$$



This equation is one of the most simplified forms that we have obtained. However, using the following units, we can simplify the equation a little more:

$$\begin{aligned} 1 \text{ Ha} &= 27.2114 \text{ eV} = 4.3597 \cdot 10^{-18} \text{ J}, \\ 1 \text{ bohr} &= 0.529177 \text{ \AA} = 0.529177 \cdot 10^{-10} \text{ m}, \\ 1 \text{ a.u. of mass} &= 9.10938291 \cdot 10^{-31} \text{ kg}. \end{aligned} \quad (2.19)$$

Using these units and setting the electronic charge,  $e = 1$ , we are forming the so-called Hartree atomic units system, which simplifies equation 2.18 in the simple form<sup>8</sup>:

$$\left[ -\sum_{i=1}^N \frac{1}{2} \nabla_i^2 - \sum_{I=1}^M \frac{1}{2M_I} \nabla_I^2 + \frac{1}{2} \sum_{i \neq j} \frac{1}{|\mathbf{r}_i - \mathbf{r}_j|} + \frac{1}{2} \sum_{I \neq J} \frac{Z_I Z_J}{|\mathbf{R}_I - \mathbf{R}_J|} - \sum_{i,I} \frac{Z_I}{|\mathbf{r}_i - \mathbf{R}_I|} \right] \Psi = E_{tot} \Psi. \quad (2.20)$$

This many-body Schrödinger equation shows that there are just two needed parameters to complete the equation depending on the material to be analyzed: the atomic numbers ( $Z_I$ ) and the atomic masses ( $M_I$ ).

### 2.1.3 The Born-Oppenheimer approximation

The Born-Oppenheimer approximation, also known as the adiabatic approximation, is an approximation that states the total electron-nuclear wavefunction (eq.2.8) may be separated into a part depending explicitly on only the electron coordinates, and the nuclear coordinates parametrically, and a part depending only on the nuclear coordinates. We will consider the wavefunction  $\Psi_e$  for electron coordinates and  $\chi_n$  for the nuclear coordinates<sup>9,11</sup>:

$$\Psi(\mathbf{r}_1, \mathbf{r}_2, \dots, \mathbf{r}_N; \mathbf{R}_1, \mathbf{R}_2, \dots, \mathbf{R}_M) = \Psi_e(\mathbf{r}_1, \mathbf{r}_2, \dots, \mathbf{r}_N) \chi_n(\mathbf{R}_1, \mathbf{R}_2, \dots, \mathbf{R}_M). \quad (2.21)$$

Nuclei masses are more than three orders of magnitude bigger than the electron's mass. Consequently, electrons follow the motion of the nuclei almost instantaneously so that the electronic states are consistently in their ground state on the time scale of nuclear motion<sup>9</sup>. In this sense, the nuclei kinetic energy contribution can be neglected setting  $M_I = \infty$ <sup>8</sup>.

Considering that Coulomb repulsion between nuclei is a constant, for convenience, we can define the following energy to simplify the equation 2.20

$$E = E_{tot} - \frac{1}{2} \sum_{I \neq J} \frac{Z_I Z_J}{|\mathbf{R}_I - \mathbf{R}_J|}. \quad (2.22)$$

By fixing constant the nuclei positions of the Coulomb potential of the electron-nuclei interaction, we can redefine the potential just with an electronic spatial dependence

$$V_n(r) = - \sum_I \frac{Z_I}{|\mathbf{r} - \mathbf{R}_I|}. \quad (2.23)$$

Substituting equations 2.21, 2.22 and 2.23 into equation 2.20, we can obtain the electronic structure fundamental equation

$$\left[ - \sum_{i=1}^N \frac{1}{2} \nabla_i^2 + \sum_i V_n(\mathbf{r}_i) + \frac{1}{2} \sum_{i \neq j} \frac{1}{|\mathbf{r}_i - \mathbf{r}_j|} \right] \Psi_e = E \Psi_e. \quad (2.24)$$

Thanks to the Born-Oppenheimer approximation, we have decoupled the electronic structure fundamental equation from the complete many-body Schödinger equation. This equation has just a dependence on the positions of the electrons being convenient to perform electronic structures analysis<sup>8</sup>.

#### 2.1.4 The independent electrons approximation

In order to study behavior of the electronic structure, from equation 2.24, we can define the many-electron Hamiltonian, which involves the Coulomb interaction between electrons

$$\hat{H}(\mathbf{r}_1, \dots, \mathbf{r}_N) = - \sum_{i=1}^N \frac{1}{2} \nabla_i^2 + \sum_i V_n(\mathbf{r}_i) + \frac{1}{2} \sum_{i \neq j} \frac{1}{|\mathbf{r}_i - \mathbf{r}_j|}. \quad (2.25)$$

Similarly, we can also define the single-electron Hamiltonian, which only has the single electron-nuclei Coulomb interaction

$$\hat{H}_0(\mathbf{r}) = -\frac{1}{2} \nabla^2 + V_n(\mathbf{r}). \quad (2.26)$$

By combining equation 2.26 into equation 2.25, we obtain the many-electron Hamiltonian in the following form:

$$\hat{H}(\mathbf{r}_1, \dots, \mathbf{r}_N) = \sum_{i=1}^N \hat{H}_0(\mathbf{r}_i) + \frac{1}{2} \sum_{i \neq j} \frac{1}{|\mathbf{r}_i - \mathbf{r}_j|}. \quad (2.27)$$

Recognizing that the Coulomb interaction between electrons carries significant complications to solve equation 2.24, we may switch off this interaction and use equation 2.27 to obtain<sup>8</sup>:

$$\sum_{i=1}^N \hat{H}_0(\mathbf{r}_i) \Psi = E \Psi, \quad (2.28)$$

where the probability of finding an electron  $i$  at  $\mathbf{r}_i$  is independent of each other,  $|\phi_i(\mathbf{r}_i)|^2$ . Then, the wavefunction  $\Psi$  can be rewritten as the product of the independent electron wavefunctions<sup>8</sup>:

$$\Psi(\mathbf{r}_1, \mathbf{r}_2, \dots, \mathbf{r}_N) = \phi_1(\mathbf{r}_1) \cdots \phi_N(\mathbf{r}_N). \quad (2.29)$$

Thus, using these wavefunctions, equation 2.28 becomes:

$$\left[ \sum_{i=1}^N \hat{H}_0(\mathbf{r}_i) \right] \phi_1(\mathbf{r}_1) \cdots \phi_N(\mathbf{r}_N) = E \phi_1(\mathbf{r}_1) \cdots \phi_N(\mathbf{r}_N), \quad (2.30)$$

where the total energy  $E$ , is the sum of all the eigenvalues ( $\varepsilon_1 + \cdots + \varepsilon_N$ ) of each independent wavefunction  $\phi_i$ .

This result means that when we fill the lowest energy eigenstates with one electron in each state, starting from the lowest eigenvalue, we will obtain the system's lowest energy configuration. At this point, it is essential to mention that this approximation has two several problems<sup>8</sup>. The first one is that equation 2.29 does not satisfy the Pauli exclusion principle. While, the second one is that the eliminated Coulomb term has the same order of magnitude as the rest of the terms, so it cannot be ignored. Both problems will be solved in the next section.

### 2.1.5 Hartree-Fock theory

The previous section found some complications concerning the Pauli exclusion principle and the electron Coulomb repulsion term. The Pauli exclusion principle states that two electrons with opposite spin can occupy the same energy state and the resulting antisymmetric wave function<sup>10</sup>. Then, to solve this problem, we should consider that we have to change the sign of the many-body wave function when exchanging the electron positions and finally introduce a Slater determinant that satisfies the antisymmetry property, replacing the equation 2.29 by:

$$\Psi_{HF} = \frac{1}{\sqrt{N!}} \begin{vmatrix} \phi_1(\mathbf{r}_1) & \phi_1(\mathbf{r}_2) & \cdots & \phi_1(\mathbf{r}_N) \\ \phi_2(\mathbf{r}_1) & \phi_2(\mathbf{r}_2) & \cdots & \phi_2(\mathbf{r}_N) \\ \vdots & \vdots & \ddots & \vdots \\ \phi_N(\mathbf{r}_1) & \phi_N(\mathbf{r}_2) & \cdots & \phi_N(\mathbf{r}_N) \end{vmatrix}, \quad (2.31)$$

where  $N$  is the number of electrons in the system and HF denotes to Hartree-Fock. For the next calculations, we will consider that perhaps the interaction of the electrons is not too strong to take into account the spin terms. Also, it is important to remember that the wavefunction should be correctly normalized using

$$\int |\Psi_{HF}|^2 d\mathbf{r}_1 \cdots d\mathbf{r}_N = 1. \quad (2.32)$$

Regarding the electron number density is considered as one of the three main HF equations; it is calculated by adding up the probabilities of finding electrons in each occupied state  $i$ <sup>8</sup>:

$$n(\mathbf{r}) = \sum_i |\phi_i(\mathbf{r})|^2. \quad (2.33)$$

Once we solved the Pauli exclusion principle problem, we now need to add a term that replaces the electron Coulomb repulsion term in  $\hat{H}_0$ , maintaining the single-particle approximation saw in the previous chapter. For this, we should consider the distribution of the electronic charge  $n(\mathbf{r})$  from the classical electrostatics point of view. This electronic charge will generate an electrostatic potential that is described by Poisson's equation, which in Hartree units is given by<sup>8</sup>:

$$\nabla^2 V_H(\mathbf{r}) = 4\pi n(\mathbf{r}), \quad (2.34)$$

where  $V_H(\mathbf{r}) = -\varphi(\mathbf{r})$  is the Hartree potential that have the electrons immersed in the electrostatic potential  $\varphi(\mathbf{r})$ , generated by  $n(\mathbf{r})$ . The formal solution for the Hartree potential is:

$$V_H(\mathbf{r}) = \int d\mathbf{r}' \frac{n(\mathbf{r}')}{|\mathbf{r} - \mathbf{r}'|} = \sum_j \int d\mathbf{r}' \frac{|\phi_j(\mathbf{r}')|^2}{|\mathbf{r} - \mathbf{r}'|}, \quad (2.35)$$

where  $d\mathbf{r}'$  is an element of volume that describes the charge  $dQ = -n(\mathbf{r}')d\mathbf{r}'$  that generates a Coulomb potential  $dQ/|\mathbf{r} - \mathbf{r}'|$  at position  $\mathbf{r}$ .

This is the mean-field approximation. It is essential to mention that Poisson's equation in Hartree units is also considered one of the three main HF equations that significantly simplifies the many-body Schrödinger equation. Using both previous corrections, we can write the single-particle Schrödinger equation with the Hartree potential

$$\left[ -\frac{1}{2}\nabla^2 + V_n(\mathbf{r}) + V_H(\mathbf{r}) \right] \phi_i(\mathbf{r}) = \varepsilon_i \phi_i(\mathbf{r}). \quad (2.36)$$

In order to find the single-particle wavefunctions  $\phi_i$ , we need to use the variational principle considering that  $\Psi_{HF}$  is a solution for the electronic ground-state energy<sup>8,9</sup>. To simplify the notation, from now on, we will use the Dirac notation:

$$E_{HF}[\phi_i] = \langle \Psi_{HF} | \hat{H} | \Psi_{HF} \rangle = \int d\mathbf{r}_1 \cdots d\mathbf{r}_N \Psi_{HF}^* \hat{H} \Psi_{HF}, \quad (2.37)$$

where the  $\hat{H}$  comes from the fundamental equation of the electronic structure theory (eq. 2.24) and  $E$  is the ground-state energy. It is important to note that  $\phi_i$  wavefunctions should be orthonormal, which means that they should be orthogonal and normalized; this will simplify enormously the calculations considering its requirement:

$$\langle \phi_i | \phi_j \rangle = \delta_{ij}. \quad (2.38)$$

Before minimizing the ground-state energy, we can notice that  $E_{HF}[\phi_i]$  has a dependence on  $\phi_i$ . It means that  $E_{HF}[\phi_i]$  is a functional of  $\phi_i$ . Considering this, we can use the Lagrange multipliers method, which introduces the functional  $E_{HF}[\phi_i]$  with the incorporated constraints<sup>8,9</sup>

$$L[\phi_{i,j}, \varepsilon_{ij}] = E_{HF}[\phi_i] - \sum_{i=1}^N \varepsilon_{ij} [\langle \phi_i | \phi_j \rangle - \delta_{ij}] = 0, \quad (2.39)$$

where  $\varepsilon_i$  act as Lagrange multipliers ensuring the normalization of the eigenfunctions.

In the Lagrange multipliers method, we can pass from the constrained minimization problem of  $\delta E / \delta \phi_i = 0$  to the unconstrained minimization problem given by<sup>8</sup>:

$$\frac{\delta L}{\delta \phi_i} = 0, \quad i = 1, \dots, N, \quad (2.40)$$

and

$$\frac{\delta L}{\delta \varepsilon_{ij}} = 0, \quad i, j = 1, \dots, N. \quad (2.41)$$

Note that differentiating equation 2.39 with respect to the Lagrange multipliers, we obtain the same equation as 2.38. Concerning to equation 2.40, we evaluate the derivatives with respect to  $\phi_i^*$ , obtaining:

$$\frac{\delta L}{\delta \phi_i^*} = \hat{H}_0(\mathbf{r})\phi_i(\mathbf{r}) + \sum_j \int d\mathbf{r}' \frac{|\phi_j(\mathbf{r}')|^2}{|\mathbf{r} - \mathbf{r}'|} \phi_i(\mathbf{r}) - \sum_j \int d\mathbf{r}' \frac{\phi_j^*(\mathbf{r}')\phi_j(\mathbf{r})}{|\mathbf{r} - \mathbf{r}'|} \phi_i(\mathbf{r}') - \varepsilon_{ii}\phi_i(\mathbf{r}) = 0, \quad (2.42)$$

where  $i \neq j$  and  $j$  runs over the occupied single particle states. Here, we find two fundamental expressions known as the Hartree potential (eq. 2.35) and Fock exchange potential<sup>8</sup>:

$$V_X(\mathbf{r}, \mathbf{r}') = - \sum_j \frac{\phi_j^*(\mathbf{r}')\phi_j(\mathbf{r})}{|\mathbf{r} - \mathbf{r}'|}. \quad (2.43)$$

Generalizing all the results that we have obtained in this section, we can write the single-particle Schrödinger equation as:

$$\left[ -\frac{1}{2}\nabla^2 + V_n(\mathbf{r}) + V_H(\mathbf{r}) \right] \phi_i(\mathbf{r}) - \int d\mathbf{r}' V_X(\mathbf{r}, \mathbf{r}') \phi_i(\mathbf{r}') = \varepsilon_i \phi_i(\mathbf{r}). \quad (2.44)$$

Finally, the three main equations given by the Hartree-Fock theory are: 2.33, 2.34 and 2.44. With these three main equations, we may create a self-consistent system in the following way<sup>9</sup>:

1. Propose an initial guess of  $\phi_i$ .
2. Use  $\phi_i$  to calculate  $n(\mathbf{r})$ ,  $V_H$  and  $V_X$ .
3. Get a solution of the single-particle Schrödinger equation.
4. Use the new set of orbitals to calculate again  $n(\mathbf{r})$ .
5. Iterate the procedure until we obtain convergence.

But, even with this system, the problem arises when Fock's exchange potential incorporates the integration of a new variable  $\mathbf{r}'$ , complicating the calculations and preventing it from being a practical solution<sup>8</sup>.

### 2.1.6 Hohenberg-Kohn theorem

In order to reduce the complexity of the computational calculations, Hohenberg and Kohn developed a theory that calculates the ground-state energy,  $E_0$ , using the electron density instead of wavefunctions. This theory is based on the idea that  $E_0$  is a functional that only depends on the electron density ( $E = F[n]$ ), while excited energy states (greater states than  $E_0$ ) necessarily depend on the many-body wavefunction ( $E = F[\Psi]$ ). This statement is based on two essential theorems: Uniqueness and the Variational Principle<sup>12,13</sup>.

1. **Uniqueness** theorem states that the ground-state electron number density is uniquely determined by the external potential of the nuclei  $V_n$ <sup>12</sup>. To prove this theorem, we need to introduce the following notation to make it more straightforward to manipulate the equations:

$$\hat{T} = -\frac{1}{2} \sum_i \nabla_i^2, \quad \hat{W} = -\frac{1}{2} \sum_{i \neq j} \frac{1}{|\mathbf{r}_i - \mathbf{r}_j|}. \quad (2.45)$$

Using this notation to write the energy corresponding to equation 2.24, we obtain:

$$E = F[n] = \langle \Psi | \hat{T} + \hat{W} | \Psi \rangle + \int d\mathbf{r} n(\mathbf{r}) V_n(\mathbf{r}), \quad (2.46)$$

In this equation, we can assume that  $\Psi$  is the ground-state wavefunction of the potential  $V_n$ , which generates the density  $n(\mathbf{r})$  and the ground-state energy  $E$ . In the same way, we can suppose another potential  $V'_n$  different than  $V_n$ , which generates the same density  $n(\mathbf{r})$  but with another wavefunction  $\Psi'$ , and ground-state energy  $E'$ . Using the potential  $V'_n$ , with a wavefunction that does not correspond to its ground-state, we can obtain the following equation:

$$E' < \langle \Psi | \hat{T} + \hat{W} | \Psi \rangle + \int d\mathbf{r} n(\mathbf{r}) V'_n(\mathbf{r}). \quad (2.47)$$

Solving the equation 2.46 with respect to the bra-kets term and replacing it in equation 2.47, we would obtain:

$$E' - E > \int d\mathbf{r} n(\mathbf{r}) [V'_n(\mathbf{r}) - V_n(\mathbf{r})]. \quad (2.48)$$

Repeating the same procedure for  $V_n$  instead of  $V'_n$ ,  $\Psi'$  instead of  $\Psi$  and  $E$  instead of  $E'$ , we would find:

$$E - E' > \int d\mathbf{r} n(\mathbf{r}) [V_n(\mathbf{r}) - V'_n(\mathbf{r})]. \quad (2.49)$$

By subtracting equation 2 from equation 3, we obtain a contradiction,  $0 > 0$ . This means that the supposition of the potential  $V'_n$  different than  $V_n$ , which generates the same density  $n(\mathbf{r})$ , is not valid. Thus, demonstrating that the ground-state electron number density  $n(\mathbf{r})$  is uniquely determined by the external potential of the nuclei  $V_n$ <sup>12,13</sup>.

2. **Variational Principle** theorem states that the ground-state energy  $E_0$  can be found by using the functional of energy  $E = F[n]$ , with the electron number density  $n(\mathbf{r})$  that minimizes it<sup>12</sup>. It is an alternative to the Schrödinger equation expressed only in terms of  $n(\mathbf{r})$ . Taking into account that  $E = F[n]$ , the mathematical expression for this statement will be:

$$\left. \frac{\delta F[n]}{\delta n} \right|_{n_0} = 0. \quad (2.50)$$

### 2.1.7 Kohn-Sham theory

The presentation of the two essential Hohenberg-Kohn theorems gives a proper perspective on calculating the ground-state energy using the total energy as a functional of the electron number density. However, these theorems did not provide any idea on how to construct that functional. In this sense, Kohn and Sham proposed some equations that builds the functional, reducing the many-body problem to a single-particle system with an additional exchange and correlation term. This new system is a fictitious system of non-interacting electrons whose ground-state electron number density is exactly the same as the fully-interacting electron number density<sup>8</sup>.

In order to develop the Kohn-Sham equations that describe how to construct the functional, we will start by splitting equation 2.46 into the kinetic and Coulomb energy of independent electron, as in equation 2.36, and adding up the additional exchange and correlation term:

$$E = F[n] = \int d\mathbf{r} n(\mathbf{r})V_n(\mathbf{r}) - \sum_i \int d\mathbf{r} \phi_i^*(\mathbf{r}) \frac{\nabla^2}{2} \phi_i(\mathbf{r}) + \frac{1}{2} \int \int d\mathbf{r} d\mathbf{r}' \frac{n(\mathbf{r})n(\mathbf{r}')}{|\mathbf{r} - \mathbf{r}'|} + E_{xc}[n]. \quad (2.51)$$

The first three terms of this equation represent the known contributions taken from the independent electrons approximation and corresponding to external potential energy, kinetic energy, and Hartree energy. However, the last term corresponds to the unknown many-body contributions, better known as exchange and correlation energy<sup>8,9</sup>. It is important to mention that if we knew precisely the exchange and correlation energy value, we could calculate the ground-state energy's exact value using the electron number density. The electron number density for this system can be calculated using equation 2.33 with the Kohn-Sham wavefunctions. Recognizing that the total energy,  $E$ , reaches its minimum value using the ground-state electron number density, we can use the variational principle theorem of Hohenberg and Kohn to obtain the following condition for the orbitals:

$$\frac{\delta F}{\delta \phi_i^*} = \frac{\delta F}{\delta n} \frac{\delta n}{\delta \phi_i^*} = 0. \quad (2.52)$$

This condition establishes a problem similar to the minimization problem solved in the Hartree-Fock theory, where it was convenient that the wavefunctions satisfy the orthonormality conditions,  $\langle \phi_i | \phi_j \rangle = \delta_{ij}$ . Similarly, as in the Hartree-Fock theory, we can use the Lagrange multipliers method to solve the constrained optimization problem of equation 2.52, using as functional  $E = F[n]$ , and Lagrange multipliers  $\varepsilon_{ii}$ <sup>8,9</sup>. After a straightforward mathematical manipulation, we will get:



$$\left[ -\frac{\nabla^2}{2} + V_n(\mathbf{r}) + \int d\mathbf{r}' \frac{n(\mathbf{r}')}{|\mathbf{r} - \mathbf{r}'|} + \frac{\delta E_{xc}}{\delta n} \right] \phi_i(\mathbf{r}) = \sum_j \varepsilon_{ij} \phi_j(\mathbf{r}), \quad (2.53)$$

where the four terms of the right side, from left to right, are already known as kinetic energy, external nuclear potential, Hartree potential, and exchange-correlation potential. The exchange and correlation potential is given by:

$$V_{xc}(\mathbf{r}) = \left. \frac{\delta E_{xc}[n]}{\delta n} \right|_{n(\mathbf{r})}. \quad (2.54)$$

where  $E_{xc}[n]$  is known as the exchange-correlation functional. Rewriting equation 2.53 in a more compact form, considering that the Lagrange multipliers can be diagonalized since the Hamiltonian is hermitian, then, one of the most characteristic Kohn-Sham equation is<sup>8,9</sup>:

$$\left[ -\frac{\nabla^2}{2} + V_n(\mathbf{r}) + V_H(\mathbf{r}) + V_{xc}(\mathbf{r}) \right] \phi_i(\mathbf{r}) = \varepsilon_i \phi_i(\mathbf{r}). \quad (2.55)$$

In summary, the Kohn-Sham theory describes a fictitious system of only electrons that interact through the external potential. In this way, all many-body interaction effects are contained in the equations from the theorem. Instead, the unknown many-body contributions are represented in the exchange and correlation energy  $E_{xc}$ , and potential  $V_{xc}$ . Finally, we could mention that the importance of constructing a useful approximation for the  $E_{xc}$  will determine how accurate the DFT results would be. Currently, the exact form of the functional,  $E_{xc}$ , is unknown for general systems. For this reason, the approximations are very useful due to their utility<sup>8</sup>.

### 2.1.8 Spin in density-functional theory

DFT calculations for magnetic materials, it is common to neglect the electron current density, which can be treated separately when one is interested in diamagnetic effects or electric polarization. Considering only the electron density  $n(\mathbf{r})$  and the spin density  $s(\mathbf{r})$ , by neglecting the current and the minor components of the Dirac spinors, we refer to the ‘spin-density functional theory’ (spin-DFT). The extension of the Hohenberg–Kohn theorem to spin-DFT can be summarized as the total energy as a functional of the electron density and spin density<sup>8,14</sup>,

$$E = G[n(\mathbf{r}), \mathbf{s}(\mathbf{r})]. \quad (2.56)$$

The quantities  $n(\mathbf{r})$  and  $\mathbf{s}(\mathbf{r})$  are commonly written in terms a the compact object called the density matrix, defined as follows:

$$n_{\alpha\beta}(\mathbf{r}) = \sum_i \phi_i^*(\mathbf{r}; \alpha) \phi_i(\mathbf{r}; \beta). \quad (2.57)$$

where  $\alpha$  and  $\beta$  takes the values 1 or 2 in order to identify the spinor components.

According to Barth and Hedin (1972)<sup>14</sup>, considering the simplest situation where there is no external magnetic field, we have exactly  $N$  electrons and the spinors are orthonormal, then the Kohn–Sham equation (eq. 2.55) in spin-DFT can be written as:

$$\left[ -\frac{\nabla^2}{2} + V_n(\mathbf{r}) + V_H(\mathbf{r}) \right] \phi_i(\mathbf{r}, \alpha) + \sum_{\beta} \vartheta_{\alpha\beta}^{xc}(\mathbf{r}) \phi_i(\mathbf{r}; \beta) = \varepsilon_i \phi_i(\mathbf{r}; \alpha), \quad (2.58)$$

where  $\vartheta_{\alpha\beta}^{xc}(\mathbf{r})$  is the exchange and correlation potential, in this case is a matrix of functions defined in the following way:

$$\vartheta_{\alpha\beta}^{xc}(\mathbf{r}) = \left. \frac{\delta E_{xc}}{\delta n_{\alpha\beta}} \right|_{n_{\alpha\beta}(\mathbf{r})}. \quad (2.59)$$

In order to make more understandable this quantity, it is helpful to proceed as follows. We define:

$$V_{xc} = \frac{\vartheta_{11}^{xc} + \vartheta_{22}^{xc}}{2}, \quad B_x^{xc} = \frac{\vartheta_{12}^{xc} + \vartheta_{21}^{xc}}{2\mu_B}, \quad B_y^{xc} = i \frac{\vartheta_{12}^{xc} - \vartheta_{21}^{xc}}{2\mu_B}, \quad B_z^{xc} = \frac{\vartheta_{11}^{xc} - \vartheta_{22}^{xc}}{2\mu_B} \quad (2.60)$$

so that the exchange and correlation matrix can be written as<sup>15</sup>

$$\vartheta_{\alpha\beta}^{xc}(\mathbf{r}) = V_{xc}(\mathbf{r}) \mathbf{1} + \mu_B \boldsymbol{\sigma} \cdot \mathbf{B}_{xc}(\mathbf{r}) \quad (2.61)$$

where  $\boldsymbol{\sigma}$  represents the Pauli matrices,  $\mu_B = 1/2$  in Hartree units and  $\mathbf{B}_{xc}(\mathbf{r})$  is an effective magnetic field generated by the many electrons, also called exchange-correlation magnetic field; this extra field tends to align the spin of the electrons of the system that could lead to a magnetic order<sup>8</sup>.

### 2.1.9 Self-consistent calculations

The fundamental idea behind standard DFT is to use self-consistency procedures to determine, as accurate as possible, the ground-state electron number density  $n_0(\mathbf{r})$ , and energy  $E_0[n]$ . In this sense, we can use the well known Kohn-Sham equations (2.23, 2.33, 2.34, 2.54 and 2.55) to construct a self-consistent algorithm that will calculate the optimal  $n_0(\mathbf{r})$  and  $E_0[n]$ <sup>8</sup>:

1. Calculate the nuclear potential ( $V_n$ ), equation 2.23, using the nuclear coordinates of the system. Usually, the system itself provides crystallographic information such as nuclear coordinates.

2. Propose an initial guess for the electron number density,  $n(\mathbf{r})$ . A helpful approximation to construct the initial guess can be by adding up the electron density of the isolated atoms arranged in the system's atomic positions.
3. Use  $n(\mathbf{r})$  to calculate an estimate of the Hartree, and exchange and correlation potentials ( $V_H$  and  $V_{xc}$ ), equations 2.34 and 2.54. Notice that once obtained these potentials, the equation 2.55 is already complete with all its potentials terms.
4. Proceed to solve the Kohn-Sham equation 2.55 to find the new wavefunctions,  $\phi_i$ .
5. Use  $\phi_i$  through equation 2.33 to construct a better estimate of  $n(\mathbf{r})$  and equation 2.55.
6. Finally, compare the newly calculated electron number density with that used to generate the potentials. If they are within a certain threshold of each other, the system is converged. Otherwise, mix the new density and the old density to obtain a new guess for the electronic density and begin the procedure once again.

## 2.2 Exchange-correlational functionals

To fully address the theory of electronic structure, DFT has been developing a series of methods to model real problems with exact or approximate solutions. In this way, we can find the Kohn-Sham theory, which, although it introduces orbitals that increase the computational cost in DFT by some orders of magnitude, is considered one of the most accurate and applied theories in many areas of physics and chemistry<sup>7</sup>. In this theory, the only unknown term is the exchange-correlation functional,  $E_{xc}[n]$ , which is often represented by the sum of the exchange and correlation terms. In the efforts to find an accurate functional that satisfies most material systems' modeling, hundreds of non-empirical and semi-empirical density functionals have been developed<sup>7</sup>. Within all this large number of functionals, there is a possible hierarchy developed by John Perdew and represented as a Jacob's ladder (see Figure 2.1)<sup>16,17</sup>. This ladder is based on the Hartree theory, where the exchange-correlation energy is zero, and the electron-electron interaction is provided by classical electrostatics<sup>7</sup>. In the following subsections, we will describe the first three rungs of Jacob's ladder, paying special attention to the third rung. This rung contains the SCAN functional, which is the functional used in this work.

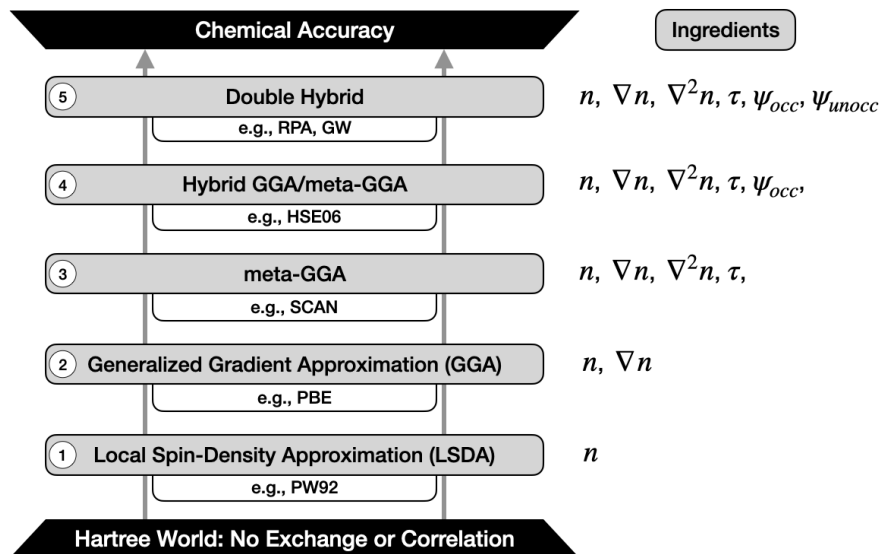


Figure 2.1: Jacob’s ladder of density-functional theory approximations to the exchange-correlation energy. The ladder has five rungs distributed according to the precision and the number of ingredients used by the functional. The ladder starts from the Hartree theory (earth) and ends in chemical accuracy (heaven). In this way, moving up the ladder introduces additional ingredients into the functional form, increasing the results’ accuracy. This Figure was adapted from the work of Mandirossian and Head-Gordon<sup>7</sup>.

### 2.2.1 The local spin-density approximation

The first rung of Jacob’s ladder has the simplest approximation for the exchange-correlation energy. This approximation is known as the local spin-density approximation (LSDA)<sup>16–18</sup>,

$$E_{xc}^{\text{LSDA}}[n_{\uparrow}, n_{\downarrow}] = \int d^3r n(\mathbf{r}) e_{xc}^{\text{unif}}(n_{\uparrow}, n_{\downarrow}), \quad (2.62)$$

where  $e_{xc}^{\text{unif}}(n_{\uparrow}, n_{\downarrow})$  is the exchange-correlation energy per electron for the uniform gas, which uses only local spin densities  $n_{\uparrow}$  and  $n_{\downarrow}$ . For this reason, the functionals that use this approximation are exact for uniform electron gas calculations but are highly inaccurate for molecular properties, considering most real systems have inhomogeneous densities distributions<sup>7,17</sup>. In other words, we can say that LSDA is a descent approximation for solids but less useful for atoms and molecules.

### 2.2.2 The generalized gradient approximation

The second rung of Jacob's ladder contains an improved version of LSDA, the so-called generalized gradient approximation (GGA)<sup>16–18</sup>,

$$E_{xc}^{GGA}[n_{\uparrow}, n_{\downarrow}] = \int d^3r n(\mathbf{r}) e_{xc}^{unif}(n) F_{xc}(n_{\uparrow}, n_{\downarrow}, \nabla n_{\uparrow}, \nabla n_{\downarrow}), \quad (2.63)$$

where  $F_{xc}$  is the enhancement factor. This approximation arises from the second-order gradient expansion (GEA) problem, where it violates the key properties of the exchange-correlation hole<sup>16</sup>. To satisfy the exchange-correlation hole's key properties and solve the inhomogeneous density distribution problem presented in LSDA, the GGA introduces the ingredients of the normalized gradient of the density  $\nabla n_{\uparrow}$  and  $\nabla n_{\downarrow}$ <sup>16,19</sup>. The GGA overestimates lattice constants but surface energies are better than LSDA for exchange alone and correlation alone but worse for their sum, and improved atomization energies with errors of about 10 kcal/mol on average<sup>17</sup>. In general, many GGA xc functionals (e.g., LYP, PW91, PBE, and PBEsol) are designed to improve particular kinds of calculations at the expense of others; that is, the GGA can be accurate for structure calculations as lattice constants or energy calculations, but not both.

### 2.2.3 The meta-GGA

Increasing the computational accuracy by using an extra natural set of semilocal ingredients, the next rung in Jacob's ladder is the meta-GGA<sup>16,17,20</sup>,

$$E_{xc}^{MGGA}[n_{\uparrow}, n_{\downarrow}] = \int d^3r n(\mathbf{r}) e_{xc}^{unif}(n) F_{xc}(n_{\uparrow}, n_{\downarrow}, \nabla n_{\uparrow}, \nabla n_{\downarrow}, \nabla^2 n_{\uparrow}, \nabla^2 n_{\downarrow}, \tau_{\uparrow}, \tau_{\downarrow}). \quad (2.64)$$

Which additionally contains the Laplacian of the density,  $\nabla^2 n$ , and the Kohn-Sham orbital kinetic energy densities  $\tau_{\sigma}$  that appear in the Taylor expansion of the exchange hole density about  $|\mathbf{r}' - \mathbf{r}| = 0$ ,

$$\tau_{\sigma}(\mathbf{r}) = \frac{1}{2} \sum_i^{\text{occ.}} |\nabla \phi_{i\sigma}(\mathbf{r})|^2, \quad (2.65)$$

where  $\sigma = \uparrow, \downarrow$  and  $n_{\sigma} = \sum_i |\nabla \phi_{i\sigma}|^2$ . Although  $\tau_{\sigma}$  is a nonlocal functional of the density, it is accessible in every calculation<sup>20</sup>. There are two formal deductions for the incorporation of  $\tau$ . The first deduction arises naturally in the Taylor expansion of the exact spherically averaged exchange hole near the reference point<sup>21</sup>. In contrast, the second comes from the idea that  $\tau$  presents a simple and straightforward way to make a correlation functional exactly one-electron self-interaction free<sup>22</sup>. Thanks to the kinetic energy densities, meta-GGA has the flexibility to satisfy more exact constraints and break the idea that the functionals

are accurate just for structures or energies. The Meta-GGA is considered a semilocal functional that is expected to work best when the exact exchange-correlation hole is well localized around its electron. It is slowly varying for compact electron densities<sup>16</sup>. Using the following dimensionless variable:

$$\alpha = \frac{(\tau - \tau^w)}{\tau^{\text{unif}}}, \quad (2.66)$$

where  $\tau^{\text{unif}}$  is the kinetic energy density of the uniform electron gas and  $\tau^w = |\nabla n|^2 / 8n$  is the von Weizsäcker kinetic energy density that is exact for single-orbital systems, meta-GGA can identify different chemical bonds. The metallic bonds with  $\alpha \approx 1$ , slowly varying densities. The covalent single bonds with  $\alpha = 0$ , the single-orbital systems. And the noncovalent bonds with  $\alpha \gg 1$  between two closed shells<sup>17,23</sup>.

### **Strongly constrained and appropriately normed semilocal density functional (SCAN)**

In the 2015 year, Jianwei Sun, Adrienn Ruzsinszky, and John P. Perdew developed a new nonempirical functional called strongly constrained and appropriately normed semilocal density functional (SCAN)<sup>23,24</sup>. This meta-GGA functional can successfully predict accurate geometries and energies of diversely bonded molecules and materials, including covalent, metallic, ionic, hydrogen, and van der Waals bonds. Moreover, SCAN often has the capacity to match or improve the accuracy of a computationally expensive hybrid functional at a much lower cost such as a GGA<sup>24</sup>. SCAN is the first semilocal functional that is completely constrained, obeying the exact 17 known constraints that a semilocal functional can fulfill, including the tight lower bound, rare-gas atoms, and nonbonded interaction<sup>17,23,24</sup>. The satisfaction of many universal constraints makes SCAN more predictive than GGAs or meta-GGAs that satisfy fewer exact constraints. Using the dimensionless variable  $\alpha$ , previously defined, SCAN provides a different and appropriate GGA description in each of the three limits or bonding situations, making significant and systematic improvements at comparable efficiency over its predecessors, the GGAs<sup>17</sup>.

## **2.3 Modelling Extended Systems**

### **2.3.1 Periodic systems**

The study of large atomic systems, such as whole crystals, can be a tedious and computationally expensive work as the number of atoms increases. For this reason, periodically repeated systems can be studied using a Bravais lattice. The Bravais lattice is an infinite array of discrete points constructed from the unit cell's translation described by the vector  $\mathbf{R}^{25-27}$ ,

$$\mathbf{R} = n_1 \mathbf{a}_1 + n_2 \mathbf{a}_2 + n_3 \mathbf{a}_3, \quad (2.67)$$

where  $\mathbf{a}_{1,2,3}$  are the linearly independent primitive vectors and  $n_{1,2,3}$  are integer numbers that give the total number of unit cells spanned by  $\mathbf{R}$  in all the three directions in real space. The vector  $\mathbf{R}$  can specify each atom location in the crystal lattice. If we get the Fourier transform of the Bravais lattice, we will get the so-called reciprocal lattice, described by the vector  $\mathbf{G}$ , in the same way as  $\mathbf{R}$  describes the Bravais lattice.

$$\mathbf{G} = m_1 \mathbf{b}_1 + m_2 \mathbf{b}_2 + m_3 \mathbf{b}_3, \quad (2.68)$$

where  $m_{1,2,3}$  gives the total number of unit cells spanned by  $\mathbf{G}$  in the three directions in reciprocal space, and  $\mathbf{b}_{1,2,3}$  are lattice vectors defined by:

$$\mathbf{b}_1 = 2\pi \frac{\mathbf{a}_2 \times \mathbf{a}_3}{\mathbf{a}_1 \cdot \mathbf{a}_2 \times \mathbf{a}_3}, \quad \mathbf{b}_2 = 2\pi \frac{\mathbf{a}_3 \times \mathbf{a}_1}{\mathbf{a}_1 \cdot \mathbf{a}_2 \times \mathbf{a}_3}, \quad \mathbf{b}_3 = 2\pi \frac{\mathbf{a}_1 \times \mathbf{a}_2}{\mathbf{a}_1 \cdot \mathbf{a}_2 \times \mathbf{a}_3}. \quad (2.69)$$

We can describe electrons in crystal lattices using plane waves based on the idea that the system's potential contains the periodicity of the lattice. In other words, the potential has the following invariance property under any translation  $\mathbf{R}$ <sup>25,26</sup>:

$$U(\mathbf{r} + \mathbf{R}) = U(\mathbf{r}), \quad (2.70)$$

where  $\mathbf{r}$  is a given position of interest, and  $\mathbf{R}$  represents all the possible Bravais vectors.

This potential suggests the study of a fundamental theorem for crystallographic systems called the **Bloch's theorem**. The Bloch's theorem states that the eigenfunctions of the Schrödinger equation in a periodic potential,  $U(\mathbf{r})$ , are composed of two fundamental functions: a plane wave  $e^{i\mathbf{k}\cdot\mathbf{r}}$  and a function  $u_{n\mathbf{k}}(\mathbf{r})$  with the crystal lattice periodicity  $\mathbf{R}$ <sup>25-27</sup>. Therefore, the eigenfunctions can be written in the following form:

$$\phi_{n\mathbf{k}}(\mathbf{r}) = e^{i\mathbf{k}\cdot\mathbf{r}} u_{n\mathbf{k}}(\mathbf{r}), \quad (2.71)$$

where  $n$  and  $\mathbf{k}$  are the quantum numbers (band index  $n$  and crystal momentum  $\mathbf{k}$ ).

It is important to mention that for each value of  $\mathbf{k}$ , there is an associated wave function  $\phi_{n\mathbf{k}}$  and energy  $\varepsilon_{n\mathbf{k}}$  that can be used to obtain the system's density of states. If we use Bloch's theorem in the Kohn-Sham equation (2.55) for a single electron system, we will get<sup>10</sup>

$$\left[ -\frac{1}{2}(\nabla + i\mathbf{k})^2 + V_n(\mathbf{r}) + V_H(\mathbf{r}) + V_{xc}(\mathbf{r}) \right] u_{n\mathbf{k}}(\mathbf{r}) = \varepsilon_{n\mathbf{k}} u_{n\mathbf{k}}(\mathbf{r}), \quad (2.72)$$

where the electron number density can be written as:

$$n(\mathbf{r}) = \sum_n \int_{\text{BZ}} \frac{d\mathbf{k}}{\Omega_{\text{BZ}}} f_{n\mathbf{k}} |u_{n\mathbf{k}}(\mathbf{r})|^2, \quad (2.73)$$

where  $\Omega_{\text{BZ}}$  is the volume of the first Brillouin zone, and  $f_{n\mathbf{k}}$  is equal to 1 for occupied states and 0 for unoccupied states.

All the previous equations suggest that a system that can be represented by some periodic arrangement can be successfully studied by a cell that represents the whole system. In this sense, the repetition of the cell in all directions will build and describe the entire system. Adding to this, the aid of characteristic parameters such as plane wave functions, quantum numbers, and translation vectors as  $\mathbf{R}$  and  $\mathbf{G}$  that fully describes the periodicity of the system along all the space. In our case, we will use these concepts about periodicity to simulate infinite carbon surfaces represented by supercells with thick enough slabs and appropriate vacuum thickness.

### 2.3.2 Plane-wave expansion

A possible solution of the Kohn-Sham equations consists of representing the wavefunctions using a Fourier series in combination with periodic boundary conditions, as we have seen previously. The Fourier expansion of the electron's wavefunction proceeds using the reciprocal lattice vector  $\mathbf{G}$  with its primitive vectors  $b_{1,2,3}$ . Since the function  $u_{n\mathbf{k}}(\mathbf{r})$  (in equation 2.71) satisfies periodic boundary conditions,  $u_{n\mathbf{k}}(\mathbf{r})$  can be expanded as a linear combination of plane waves<sup>8,28</sup>,

$$u_{n\mathbf{k}}(\mathbf{r}) = \sum_{\mathbf{G}} c_{n\mathbf{k}}^{\mathbf{G}} e^{i\mathbf{G}\cdot\mathbf{r}}, \quad (2.74)$$

where the sum runs over the  $\mathbf{G}$  vectors.

Using the plane-wave expansion to rewrite the Kohn-Sham wavefunctions with Bloch's theorem (equation 2.71), we will obtain:

$$\phi_{n\mathbf{k}}(\mathbf{r}) = \sum_{\mathbf{G}} c_{n\mathbf{k}}^{\mathbf{G}} e^{i(\mathbf{G}+\mathbf{k})\cdot\mathbf{r}}. \quad (2.75)$$

Commonly, in packages that use plane waves basis set calculations (such as VASP), there is one parameter called the plane wave kinetic energy cutoff that specifies such waves. This parameter is defined as the quantum mechanical kinetic energy associated with the plane waves<sup>8,28,29</sup>,



$$E_{\text{cut}} = \frac{1}{2} \mathbf{G}_{\text{max}}^2 = \left\langle e^{i\mathbf{G}_{\text{max}} \cdot \mathbf{r}} \left| -\frac{1}{2} \nabla^2 \right| e^{i\mathbf{G}_{\text{max}} \cdot \mathbf{r}} \right\rangle, \quad (2.76)$$

where  $\mathbf{G}_{\text{max}}$  is the largest  $\mathbf{G}$  vector. This equation shows the relationship between the cutoff energy and the  $\mathbf{G}$  vectors in a plane-wave basis set calculation. In other words, the relationship represents the number of plane-waves used in a DFT calculation for a cutoff energy given. On the one hand, if we increase the cutoff energy value, we will increase the number of plane-waves used in the calculations giving a highly detailed electronic structure description but at a high cost computationally. On the other hand, if we reduce the cutoff energy value, we will decrease the number of plane-waves used in the calculations giving a poorer electronic structure description but at a lower cost computationally. For these reasons, we will explore the optimal value of cutoff energy to obtain a detailed enough electronic structure description, but at not too high a cost computationally<sup>8</sup>.

### 2.3.3 The $k$ -points mesh

The evaluation of physical quantities, such as energy and density, is more convenient in reciprocal space ( $k$ -space) than in real space. Because basis sets of plane-waves scale better with the number of  $k$ -points than the number of particles, it is preferable to compute on the primitive cell of the system rather than the unit cell allowing the reduction of calculation load<sup>10</sup>. Besides, the use of  $k$ -points is advantageous computationally because they allow the problem to be well-parallelized when solving the independent-particle Schrödinger equation, with the results needing to be brought together only when calculating the electron density; this makes the calculations highly parallelizable. The first Brillouin zone is defined as the primitive cell in the reciprocal space. Therefore, the volume of the first Brillouin zone can be defined by the primitive vectors  $\mathbf{b}_{1,2,3}$  in the following way<sup>8</sup>:

$$\Omega_{\text{BZ}} = |\mathbf{b}_1 \cdot \mathbf{b}_2 \times \mathbf{b}_3|. \quad (2.77)$$

The first Brillouin zone is very important in electronic structure calculations because it can help us to simplify some integration problems, as the plane wave expansion of the electron number density in the reciprocal space,

$$n(\mathbf{r}) = \sum_n \int_{\text{BZ}} d\mathbf{k} |u_{n\mathbf{k}}(\mathbf{r})|^2, \quad (2.78)$$

where the density  $n(\mathbf{r})$  is obtained by integrating over all the first Brillouin zone. The problem with solving these types of continuous integrals is that they are computationally very expensive, so Monkhorst and Pack

developed a solution for these types of problems<sup>30</sup>. The solution consists of a uniformly spaced division of the primitive vectors  $\mathbf{b}_{1,2,3}$  to form a mesh of discrete and equidistant  $k$  points, separated by  $\Delta k$ . This mesh is so-called the **Monkhorst-Pack mesh** and is determined by a simple formula valid for any crystal structure<sup>30</sup>:

$$\mu_r = \frac{2r - q_r - 1}{2q_r}, \quad (2.79)$$

where  $r = 1, 2, \dots, q_r$  and  $q_r$  determines the number of  $k$ -points along the  $\mathbf{r}$ -direction.

It is important to mention that by changing the length of the unit cell in real space, we can find two different alterations in the change of the  $k$ -points mesh<sup>29</sup>: if we increase (decrease) the unit cell length, the number of  $k$ -points in the mesh will decrease (increase). For these reasons, it is recommendable to do a convergence test of the system's energy with respect to the number of  $k$ -points in the mesh. This is done with the goal of knowing what is the optimal number of  $k$ -points. The Monkhorst-Pack method is commonly used in sophisticated simulation packages, including VASP<sup>28</sup>.

### 2.3.4 Pseudopotentials

As we have seen in the previous sections, the electronic structure study can be very precise using plane-waves basis sets. However, when we perform calculations with all the electrons of each atom (all-electrons calculations), the modeling requires an extremely high plane-wave cutoff, or a very dense real-space grid, to represent the highly oscillatory states of the core electrons, which are localized around the atom. For this reason, we need to introduce pseudopotentials to reduce the number of plane-waves necessary in a calculation<sup>28,29</sup>. The pseudopotentials' definition consists of replacing the full nuclear potential and the core electrons with a new potential that reproduces the same behavior for outer electrons (valence electrons)<sup>8,28,29</sup>. This definition arises from the idea that valence electrons will be the most sensitive to changes in the chemical bonding environment. In contrast, core electrons will be relatively immune to such changes. Therefore, valence electrons are essential in defining chemical bonding and other physical properties of materials. In this sense, we can completely freeze the core electrons for our description and save considerable computational effort<sup>8</sup>. The strategy on the pseudopotentials method lies in the construction of a modified nuclear potential that satisfies the following conditions<sup>8</sup>:

1. Outside the pseudization region, the modified potential should coincide with the original Kohn–Sham potential obtained from a calculation including all the electrons.

2. Inside the pseudization region, the potential should be modified in such a way that the solution of the Kohn–Sham equation yields the pseudo-wavefunction precisely.

It is important to mention that the distinction between core and valence electrons is not rigorous and depends on the accuracy that one is trying to achieve and the computational cost that one is willing to pay<sup>8</sup>. In DFT simulations, the details of a pseudopotential define a minimum energy cutoff used in the calculations. Pseudopotentials that require high cutoff energies are hard, while more computationally efficient pseudopotentials with low cutoff energies are soft<sup>28</sup>. Besides, as a final remark, it is essential to notice that the field of pseudopotentials is constantly evolving today and involves many other very advanced methods.

### 2.3.5 The projector augmented-wave method

The utilization of hard or ultrasoft pseudopotentials to perform DFT calculations is not ideal. It can require a high cutoff energy radius and not restore the actual valence wavefunction, as we saw earlier. To avoid these disadvantages, Blöchl proposed the projector augmented-wave (PAW) method<sup>31</sup>, where the central idea is the exact partitioning of the electron wavefunctions. This method allows a full wave function calculation (all-electron calculation) instead of only considering the valence electrons, giving access to the full wave function information<sup>29,32</sup>, while performing calculations using smooth pseudo-wave functions. With this in mind, we can describe the PAW method considering the all-electron (AE) valence wavefunctions formed from pseudo (PS) wave functions through a linear transformation given by<sup>33</sup>:

$$|\psi_{n\mathbf{k}}^{AE}\rangle = |\psi_{n\mathbf{k}}^{PS}\rangle + \sum_i (|\phi_i^{AE}\rangle - |\phi_i^{PS}\rangle) \langle p_i^{PS} | \psi_{n\mathbf{k}}^{PS} \rangle. \quad (2.80)$$

this expression can be re-written using tildes following the notation used in the original work by Blöchl<sup>31</sup>, so that

$$|\psi_{n\mathbf{k}}\rangle = |\tilde{\psi}_{n\mathbf{k}}\rangle + \sum_i (|\phi_i\rangle - |\tilde{\phi}_i\rangle) \langle \tilde{p}_i | \tilde{\psi}_{n\mathbf{k}} \rangle, \quad (2.81)$$

where the pseudo-orbitals  $\tilde{\psi}_{n\mathbf{k}}$  are the variational quantities expanded in plane waves in VASP as

$$\tilde{\psi}_{n\mathbf{k}}(\mathbf{r}) = \langle \mathbf{r} | \tilde{\psi}_{n\mathbf{k}} \rangle = \frac{1}{\sqrt{\Omega}} \sum_{\mathbf{G}} C_{n\mathbf{k}\mathbf{G}} e^{i(\mathbf{G}+\mathbf{k})\cdot\mathbf{r}}. \quad (2.82)$$

As a final point, it is important to mention that the PAW method was adapted for plane-wave calculations by Kresse and Joubert<sup>34</sup>, giving place to accurate DFT results implemented in DFT codes such as VASP.

## 2.4 Scanning Tunneling Microscopy STM

Binnig and Rohrer invented the scanning tunnel microscope (STM) in 1982<sup>35</sup>, winning the Nobel Prize in 1986 for this invention. Today, this microscopy has become one of the most important nanoscience tools due to the quality of information and resolution that it can obtain down to the atomic scales in real space<sup>36</sup>. Some of the advantages of STM over other microscopy measurements are ultra-high resolution in lateral (0.1 nm) and depth (0.01 nm) space. It is versatile, allowing its use in ultrahigh vacuum and room to low-temperature conditions; it provides an atomically precise positioning system that allows very accurate atomic-scale manipulation and the analysis of a multitude of characteristics such as roughness, surface defect, molecule size, and conformation<sup>37</sup>. In this section, we will study the working principle of STM and how it can be simulated using the Tersoff–Hamann approximation.

### 2.4.1 Working principle

STM is based on the quantum mechanical concept called quantum tunneling, where a wavefunction can propagate through a potential barrier. In STM, a bias voltage is applied between a tip and a conducting sample, both separated by a certain vacuum distance that makes it possible to generate a tunneling current (electrons tunnel through the vacuum between the tip-sample distance). The tunneling current generally can be defined as<sup>38</sup>:

$$I \propto e^{-2s/\hbar \sqrt{2m\varphi}}, \quad (2.83)$$

where  $m$  is the mass of the electron,  $s$  is the width of the barrier, and  $\varphi$  is the height of the barrier. According to this equation, as the tunneling current increases, the tip-sample distance decreases, and vice versa. Similarly, the tunnel current sensitivity is explained by the exponential relation between the current and tip-sample distance<sup>36</sup>. The tip is located with such high accuracy using piezoelectric actuator elements. The mechanical extension of these actuator elements is proportional to the voltage applied to their electrodes. In this way, the tip can be moved in  $x$ ,  $y$ , and  $z$  directions with sub-angstrom resolution<sup>36</sup>.

There are two operation modes for STM<sup>37</sup>: the constant-current mode and the constant-height mode. On the one hand, in the constant-current mode, the feedback mechanism constantly adjusts the tip height by approaching or retracting the tip to a tip-sample distance at which the tunneling current remains constant. It leads to the image formation from the tip topography across the sample. On the other hand, in the constant-height mode, the current changes to maintain the voltage and height constants. It leads to an image made of current changes over the surface related to charge density. For our case, we will simulate the constant-height mode to study the topography of the diamond surfaces. It is important to mention that

the different electronic properties of each element will affect the tip-sample distance. In the case of a high conductive element, a larger tip-sample distance, and vice versa<sup>36</sup>.

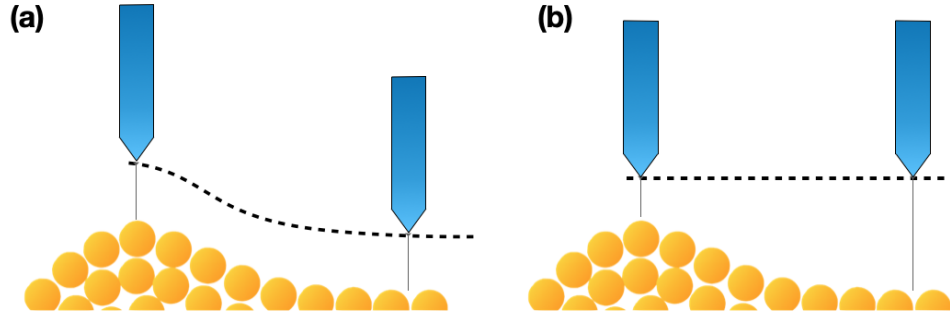


Figure 2.2: Two typical STM operating modes: (a) constant-current mode and (b) constant-height mode.

### 2.4.2 Tersoff-Hamann approximation

The tunneling current which flows between the tip and the sample depends on the voltage difference between the tip and sample. If the sample is biased by a negative voltage  $-V$  with respect to the tip, this effectively raises the sample electrons' Fermi level with respect to the tip electrons. Electrons will tend to flow out of the sample's filled states into the empty states of the tip<sup>38</sup>. The elastic tunneling current from the sample to the tip for states of energy  $\epsilon$  (with respect to the Fermi level of the sample) is:

$$I_{\text{sample} \rightarrow \text{tip}} = -2e \cdot \frac{2\pi}{\hbar} |M|^2 (\rho_s(\epsilon) \cdot f(\epsilon)) (\rho_t(\epsilon + eV) \cdot [1 - f(\epsilon + eV)]), \quad (2.84)$$

where the factor of 2 out front is for spin,  $-e$  is the electron charge,  $2\pi/\hbar$  comes from the time dependent perturbation theory,  $|M|^2$  is the matrix element,  $f(\epsilon)$  is the Fermi distribution function,  $(\rho_s(\epsilon) \cdot f(\epsilon))$  represents the filled sample states we are tunneling from, and  $(\rho_t(\epsilon + eV) \cdot [1 - f(\epsilon + eV)])$  denotes the empty tip states we are tunneling to.

Even though the dominant tunnel current for the negative sample voltage  $-V$  will be from sample to tip, there will also be a smaller electron tunnel current from tip to sample, which can be written similarly. When we add these two contributions and integrate all the energies, we arrive at the total tunnel current from the sample to the tip<sup>38</sup>:

$$I = \frac{-4\pi e}{\hbar} \int_{\epsilon_F}^{\infty} |M|^2 \rho_s(\epsilon) \rho_t(\epsilon + eV) \{f(\epsilon)[1 - f(\epsilon + eV)] - [1 - f(\epsilon)]f(\epsilon + eV)\} d\epsilon. \quad (2.85)$$

We can simplify this expression in different ways<sup>38</sup>. First, if the measurements are made at low temperature, the Fermi function cuts off very sharply at the Fermi surface, allowing that the integral breaks into 3 parts; where the most relevant range to find the tunneling current is between the Fermi energy levels of the sample and tip ( $-eV < \varepsilon < 0$ ). Second, we pick a tip material that has a flat density of states within the energy range of the Fermi surface that we wish to study so that  $\rho_t(\varepsilon + eV)$  can be treated as a constant and taken outside the integral. Third, considering the realistic assumptions of Bardeen, we can take the matrix element outside the integral and treat it as a constant. The Bardeen assumptions show that (1) the tip and the sample each have their own independent density of states, (2) each of their wavefunctions fall exponentially to zero in the tunneling barrier, and (3) the overlap is small enough (i.e. tip-sample separation is large enough) that each side is insignificantly influenced by the tail of the wavefunction from the other side, then the matrix element for tunneling will be virtually independent of the energy difference between the two sides of the barrier. The matrix element comes from the assumption that both tip and sample wavefunctions fall off exponentially into the vacuum gap. Basically, we assume that the vacuum barrier is a square barrier, and if we make a Wentzel-Kramers-Brillouin (WKB) approximation<sup>39</sup>, we will find that the tilt of the barrier will be much smaller than the height of the barrier, making it negligible. Following the WKB approximation, we find that the tunneling probability through a barrier will be  $|M|^2 = e^{-2\gamma}$  with:

$$\gamma = \int_0^s \sqrt{\frac{2m\varphi}{\hbar^2}} dx = \frac{s}{\hbar} \sqrt{2m\varphi}. \quad (2.86)$$

where  $m$  is the mass of the electron,  $s$  is the width of the barrier, and  $\varphi$  is the height of the barrier, which is actually some mixture of the work functions of the tip and sample. Notice that we can measure the work function by recording the tunneling current as a function of tip-sample separation (eq. 2.83).

Finally, considering all the previous assumptions and simplifications, we can write the tunnelling current in the following way<sup>38</sup>:

$$I \approx \frac{4\pi e}{\hbar} e^{-s \sqrt{\frac{8m\varphi}{\hbar^2}}} \rho_t(0) \int_{-eV}^0 \rho_s(\varepsilon) d\varepsilon. \quad (2.87)$$

## 2.5 Ultraviolet Photoelectron Spectroscopy UPS

Ultraviolet photoelectron spectroscopy (UPS) is a technique based on the photoelectric effect. UPS provides information about orbital energies, where ionization energies can be directly measured of orbital energies in the neutral atom or molecule and can therefore be used to construct a molecular orbital diagram. Frequently, especially for molecules in the gas phase, UPS can resolve the vibrational and rotational

structure<sup>40</sup>. The electronic spectra tend to be more difficult to resolve because it has a dependence on the symmetries of the electronic spectra involved. In comparison, the electronic spectra for the vibrational structure do not need all the vibrational frequencies active. Besides, UPS is handy for the characterization of solids because it helps determine the material's work function<sup>40</sup>. This spectroscopy technique can be successfully simulated using the density of states (DOS), inelastic mean free path (IMFP), and energy levels cross-sections of the studied material.

### 2.5.1 Working principle

UPS measures the ionization energies of the atoms or molecules when electrons are ejected from different orbitals by absorption of a photon with greater or equal energy<sup>41</sup>. This process can be represented by:



where  $M$  is the initial atom with all its corresponding electrons,  $h\nu$  represents the incident photon of the incident beam,  $M^+$  is the ionized atom after the process, and  $e^-$  is the ejected electron. The excess energy from photoionization can appear either as electron kinetic energy, ion internal energy (vibrational and rotational), or a combination of the two. Because of conservation of energy, when a photon ionizes a sample, the energy of the incident photon  $h\nu$  must be equal to the sum of the ionization energy of the sample and the kinetic energy of the photoelectron<sup>40</sup>. The ionization energy depends on which electron is being removed from which orbital. For example: if we remove a weakly bound electron, we will get the highest kinetic energy. Whereas if we remove a tightly bound electron, we will get a lower kinetic energy. To reach higher ionic states, shorter wavelengths are required, wavelengths that fall in the vacuum ultraviolet and can only be properly generated by noble gas resonance lamp sources. The most used material for the lamp sources is helium because it is an economical gas with high photon energy, allowing the photoionization process of the most atoms and molecules. This gas has its principal emission line at 21.218 eV<sup>40</sup>. The electron kinetic energy spectrum is obtained by passing the ejected electrons from the photoelectric process through an energy analyzer. Commonly, the energy analyzers are based on an electric or magnetic field. There are two main analyzer types, retarding field and deflection analyzers<sup>40</sup>. On the one hand, the retarding field analyzers transmit only those electrons with energies higher than the retarding potential, and to obtain a spectrum, the retarding potential should be scanned. This analyzer is less commonly used today. On the other hand, the deflection analyzers separate electrons by forcing them to follow different paths according to their velocities. This separation can be done using electric and magnetic fields along the path that follows the ionized electrons. Once the electrons reach the analyzer,

the electron multipliers amplify their current, converting them into electrons with enough current flow to be measurable by a picoammeter or other sensitive current measurement devices<sup>40</sup>. As a final point, it is essential to mention that a photoelectron spectrometer must be kept under vacuum and should have at least three separate pumping regions, the resonance lamp, the sample chamber, and the analyzer chamber.

In order to correctly calculate a simulated UPS spectrum, we have to consider the depth of surface sensitivity in which the incident photon energy can penetrate the surface sample. The depth of surface sensitivity is related to the inelastic mean free path (IMFP) for the ejected photoelectrons from which electrons can escape without significant scattering or energy loss to the surrounding lattice<sup>42</sup>. The probability of generating a photoelectron from a given orbital depends on its angular momentum, orientation, and dispersion within the crystal as well as the photon energy<sup>43,44</sup>. The simulated UPS spectra consider the computed partial density of states weighted with the tabulated theoretical photoionization cross-sections for each atomic orbital at photoexcitation energy of 40.82 eV, for this study. The photoionization cross sections for the outermost atomic subshells for C were taken from Yeh and Lindau<sup>43</sup>.



## Chapter 3

# Methodology

In this chapter we provide a detailed description of all the procedures done in this work. It is separated into two main sections: (i) computational details section will present all the necessary details for reproducing the calculations performed using VASP and bSKAN. (ii) The surfaces development section will explain the criteria used to optimize the structures with all their specific details and modifications.

### 3.1 Computational details

The calculations were performed using the plane-wave Viena *ab initio* Simulation Package (VASP)<sup>45</sup>, where the projector augmented wave method (PAW) was used to describe the core electrons, and the strongly constrained and appropriately normed semilocal density functional with van der Waals corrections (SCAN+rVV10) was used to describe the valence electrons. The PAW potential for hydrogen H atoms was generated in the electron configuration  $1s^1$  and for carbon C atoms in  $[\text{He}] 2s^2 2p^2$ , where square brackets denote the core electron configurations. A cutoff energy of 1000 eV combined with a  $k$ -point mesh separation equal to  $0.042 \text{ \AA}^{-1}$  and an electronic temperature of 0 K were used to converge the total energy to less than 1 meV/atom. All the structures were fully relaxed until all the forces were  $< 0.02 \text{ eV/\AA}$ . Additionally, the STM images were calculated using the Tersoff-Hamann approximation as implemented in bSKAN<sup>46</sup>. This allows computing the STM images using input wavefunctions from VASP.

## 3.2 Surface model simulations

In order to properly simulate the atomic and electronic structure of a diamond surfaces on VASP and bSKAN, it was necessary to find out the optimal parameters for diamond systems. For this, we had to examine the convergence of parameters such as cut-off energy,  $k$ -points, optimal volume, vacuum size and slab thickness. The following subsections are classified according to the optimization of the crystal and surfaces.

### 3.2.1 Crystal optimization

The diamond crystal is a well-known material with an face-centered cubic fcc lattice. The primitive basis has two identical C atoms associated with each point of the fcc lattice. Thus, the conventional unit cell contains eight C atoms<sup>26</sup>. With this information about the structure (see Figure 3.1), we were able to begin the calculations about the convergence of the cut-off energy,  $k$ -points, and optimal cell volume. Before starting the convergence tests, it was essential to consider that the errors in the energies with cut-off energy and  $k$ -points mesh should be in the range of  $< 1$  meV/atom to yield and useful DFT simulations.

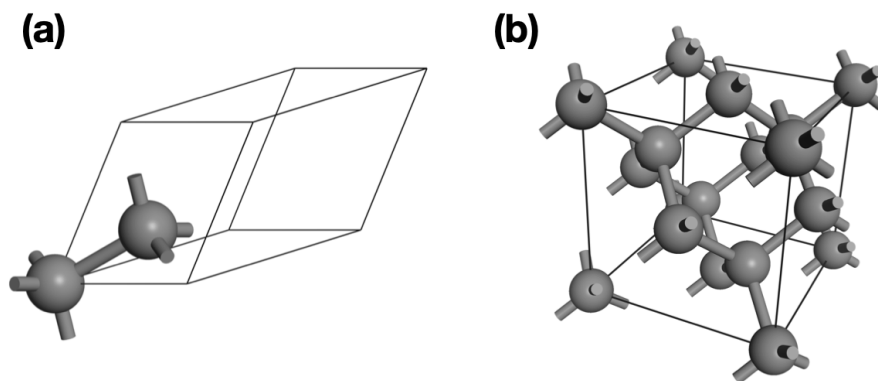


Figure 3.1: Diamond crystal structure. a) Primitive cell with only 2 C atoms. b) Conventional unit cell (cube) with eight C atoms. In both figures, the black lines delimit the size of the cell.

#### The cut-off energy

The first parameter used in the convergence test was the cut-off energy. To analyze the optimal convergence value, we had to vary the cut-off energy with a fixed  $k$ -points mesh of  $12 \times 12 \times 12$ , equivalent to  $\Delta k = 0.04 \text{ \AA}^{-1}$  for this structure. Although we did not know the optimal value of the  $k$ -points mesh for the diamond

structure, we knew that the value of the  $k$ -points mesh used is enough to yield reasonable results. Figure 3.2 shows the obtained cut-off energy values and their behavior until they get convergence in the range of  $< 1$  meV/atom. According to Figure 3.2, we could establish that  $E_{cut} = 1000$  eV will be used for further calculations.

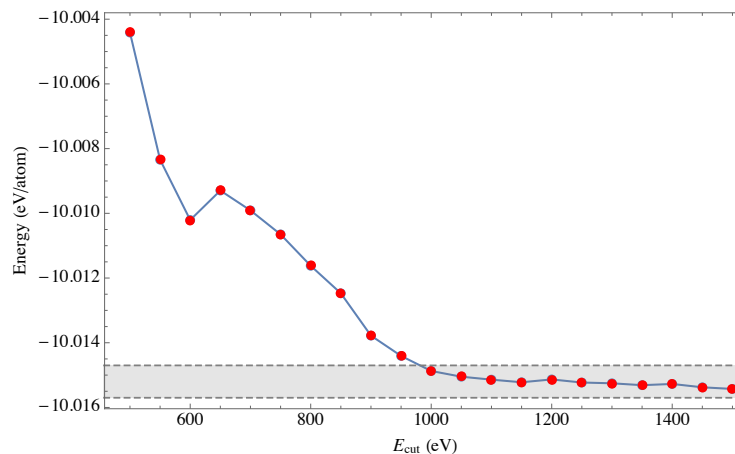


Figure 3.2: Cut-off energy convergence plot for diamond crystal. The energies begin to converge from 1000 eV according to the  $< 1$  meV/atom criteria. The gray dashed region shows the allowed convergence range.

### The $k$ -points mesh

The second parameter used in the convergence test was the Gamma-centered  $k$ -point mesh in order to employ the tetrahedron method with Blöchl corrections. For this, we varied the  $k$ -points mesh using the cut-off energy obtained in the previous test for this structure to analyze the optimal convergence value. Figure 3.3 shows the obtained  $k$ -points mesh values and their behavior until they get convergence in the range of  $< 1$  meV/atom. According to Figure 3.3, we could establish that the  $k$ -points mesh of  $10 \times 10 \times 10$ , equivalent to  $\Delta k = 0.042 \text{ \AA}^{-1}$  will be used for further calculations.

### The equation of state EOS

Once the cut-off energy and  $k$ -points converged values been determined, the last test of optimization is for the cell volume vs. the total energy. In this way, we varied the diamond crystal cell volume until we got enough data to fit and find the optimal cell volume which yields the lowest total energy. These results were

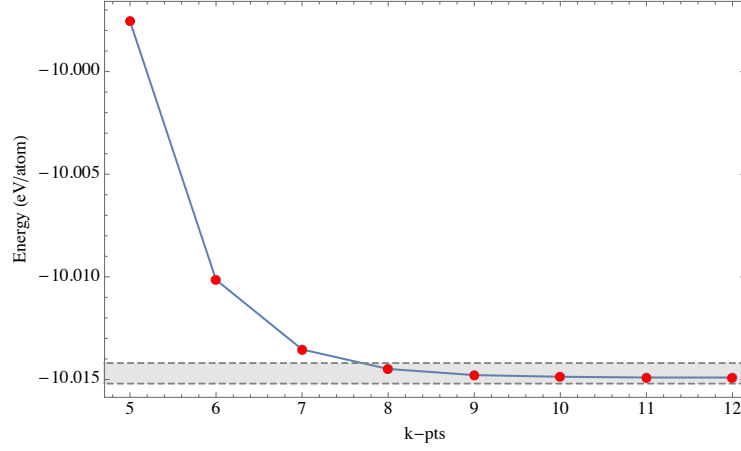


Figure 3.3:  $k$ -points mesh convergence plot for diamond crystal. The energies begin to converge from  $8 \times 8 \times 8$   $k$ -points mesh according to the  $< 1$  meV/atom criteria, but for more accurate results we use a  $k$ -points mesh of  $10 \times 10 \times 10$ . The gray dashed region shows the allowed convergence range.

obtained using the cut-off energy and  $k$ -points mesh obtained in the previous tests. The equation used for fitting the obtained data was the Birch-Murnaghan equation of state (EOS)<sup>47</sup>,

$$E(V) = E_0 + \frac{9V_0B_0}{16} \left\{ \left[ \left( \frac{V_0}{V} \right)^{2/3} - 1 \right]^3 B'_0 + \left[ \left( \frac{V_0}{V} \right)^{2/3} - 1 \right]^2 \left[ 6 - 4 \left( \frac{V_0}{V} \right)^{2/3} \right] \right\}, \quad (3.1)$$

where  $V$  is the cell volume,  $E_0$  is the ground state energy,  $V_0$  is the ground state volume,  $B_0$  is the bulk modulus and  $B'_0$  is the bulk modulus pressure derivative. To make the fit, as easiest as possible, we can simplify (3.1) in the following way:

$$E(V) = k_1 + k_2V^{-2} + k_3V^{-4/3} + k_4V^{-2/3}, \quad (3.2)$$

where  $k_{1,2,3,4}$  are constants assuming that  $E_0$ ,  $V_0$ ,  $B_0$  and  $B'_0$  are also constants.

Using equation 3.2 to fit the obtained data of the volume cell, we obtained the data shown in Figure 3.4. This Figure shows the change of the total energy of diamond fcc with the volume. To calculate the numerical values of  $E_0$ ,  $V_0$ ,  $B_0$ , and  $B'_0$  explicitly, we could use the fitting parameters  $k_{1,2,3,4}$  to solve the system of four equations with four unknowns, as provided in (3.3). Once the numerical values of  $E_0$ ,  $V_0$ ,  $B_0$ , and  $B'_0$  are determined, they were compared directly with experimental values, taking into account that both values should were in the same units.

$$\begin{aligned}
k_1 &= E_0 + \frac{27}{8}B_0V_0 - \frac{9}{16}B'_0B_0V_0, \\
k_2 &= -9B_0V_0^{5/3} + \frac{27}{16}B'_0B_0V_0^{5/3}, \\
k_3 &= \frac{63}{8}B_0V_0^{7/3} - \frac{27}{16}B'_0B_0V_0^{7/3}, \\
k_4 &= -\frac{9}{4}B_0V_0^3 + \frac{9}{16}B'_0B_0V_0^3.
\end{aligned} \tag{3.3}$$

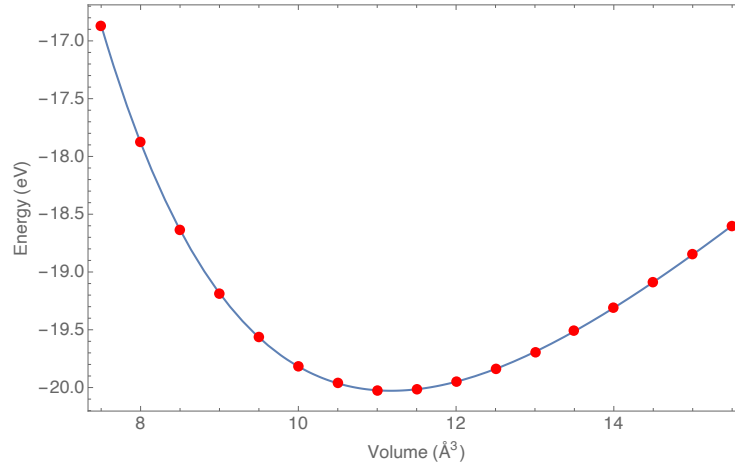


Figure 3.4: Computed SCAN+rVV10 equation of state for diamond fcc. The red dots show the computed energies and the blue line is the Birch-Murnaghan EOS fitting. In this plot the optimal or equilibrium volume of bulk diamond lattice corresponds to the lowest total energy volume.

### 3.2.2 Surfaces optimization

In order to completely characterize the atomic and electronic properties of the diamond surfaces (pristine, hydrogenated, and surfaces with carbon vacancies), the diamond crystal can be cleaved by some families of planes to get some surface structures, in our case the (110) and (111) family of planes, see Figure 3.5. The atomic structure of the diamond surface was easily constructed starting from its crystalline structure. However, there were some crucial factors that we needed to take into account to properly simulate the surfaces. These factors are the vacuum space between slabs, the slab thickness and surface passivisation.

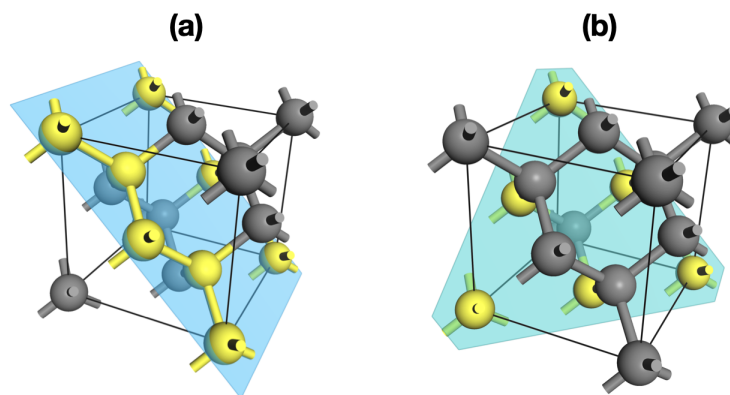


Figure 3.5: Two different cleaving planes cutting the diamond crystal in (a) plane (110) and in (b) the plane (111). The spheres in yellow are the C atoms intersected by the planes

### Optimal vacuum and slab thickness

The criteria used to determine the appropriate vacuum value between two slabs along  $z$ -direction is the self interaction energy between images, the vacuum has to be large enough to prevent the slab self interaction. Then, to calculate the optimal vacuum value of the surface, we performed a total energy convergence test varying the vacuum value. It is important to mention that the atomic structure of the surface was ready for this calculation, and it was contained in the POSCAR file. Figure 3.6 shows the data obtained for the possible optimal vacuum values. For our case, we decided to select the 15 Å of vacuum space between slabs that converge the energy to  $< 1$  meV/f.u. (f.u.= formula unit)

The criteria used to select the optimal slab thickness is that there should not be any interaction between the topmost atoms and the lower atoms within the slab. In other words, the slab should be thick enough that electrons at the topmost part of the slab do not feel the existence of the electrons at the lower part of the slab. For this reason, we had to vary the thickness of the slab until we found a specific thickness from which the electronic structure of the topmost layers (surface) does not change if the slab thickness is increased. In our case, we decided to work with nineteen layers slab for the (110) surface and with six layers slab for the (111) surface.

### Slab passivation

Once we obtain the optimal values for the slab thickness and vacuum, ideally we were ready to perform any surface calculations. However, exploring a wide variety of possible surfaces using complete slab structures

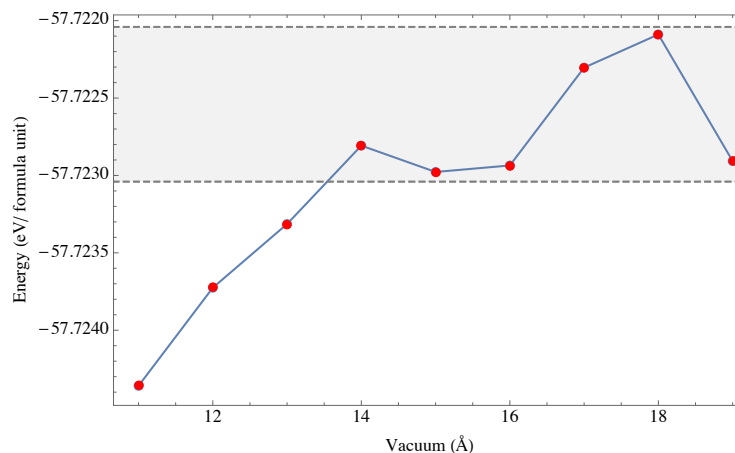


Figure 3.6: Change of system's total energy with respect to the vacuum between surfaces. The vacuum begin to converge from 14 Å. The shaded area shows the 1 meV/f.u. convergence.

(two surface faces) is not recommendable because it is very expensive computationally. For this reason, we used passivated slabs. The passivated surfaces were constructed by cleaving the entire slab in half (across the  $z$ -direction) and attaching two H atoms in each C left on the bottom of the slab, these H atoms passivate the dangling bonds of those C atoms. Once the H atoms were attached, they were relaxed and subsequently fixed with the first layer of C atoms of the same face. All of this to emulate a bulk behavior in the cut face side. In our case, we used nine layers of slab thickness (including the fixed C layer) for the (110) family. The passivated surface behavior could be verified by calculating the PDOS for the two types of surface, passivated and non-passivated. In our case, both PDOS were practically the same, which means that the passivated surface describes the same results as the non-passivated one. In the case that the PDOS for both calculations were not the same, it is recommendable to increase the thickness of the surface with unfrozen C layers. Finally, we assign the initial spin state of 3 (1.5) to the outermost layers of the unfixed C (H) atoms and allow the spin states to vary during the calculations. In this way, we were ready to perform surface calculations using the passivated surface structures and explore all its variations.

### The surface energy $\gamma$ calculation

The surface energy of a solid,  $\gamma$ , is one of the most fundamental properties that helps to identify which surface composition and geometry are the most stable and expected to be observed in nature. This energy measures the energy cost of increasing the surface area; therefore, all the normal solids should have positive

surface energy; otherwise, the solids would disintegrate<sup>48</sup>. Commonly, the surface energy equation used for slab systems composed of C and H atoms has the following form that depends on the temperature  $T$  and pressure  $p$ <sup>49,50</sup>:

$$\gamma(T, p) = \frac{1}{2A} [E_{slab} - n_C \mu_C(T, p) - n_H \mu_H(T, p)] , \quad (3.4)$$

where  $A$  is the area of the surface unit cell,  $E_{slab}$  is the energy of the slab,  $n_C$  ( $n_H$ ) is the number of C (H) atoms present in the slab;  $\mu_C$  and  $\mu_H$  is the chemical potential for C and H, respectively. In diamond surfaces,  $\mu_C = -10.015$  eV/atom, is the SCAN+rVV10 computed energy per atom of the optimal fcc structure of diamond. The chemical potential of H depends on the source gas that the surface is in equilibrium with; therefore in our simulations, we are interested on the change of  $\gamma$  with respect to  $\mu_H$ ; an appropriate upper limit for H chemical potential is when  $\mu_H = -3.426$  eV/atom that corresponds to  $1/2 E_{H_2}^{total}$ , where  $E_{H_2}^{total}$  is the total energy of a free isolated  $H_2$  molecule at  $T = 0K$  that is  $-6.852$  eV computed with SCAN+rVV10. High (low) values of  $\mu_H$  means high (low) gas pressure. Finally, (3.4) is divided by two times the area  $A$ , because the slab model presents two surfaces, one at the top and one at the bottom.

However, the previous equation cannot be used to calculate  $\gamma$  of a slab with pristine-passivated surfaces because both slab surfaces are not equivalent. So, in order to calculate the energy of any modified-passivated surfaces using equation 3.4, we had to developed the following equations. Considering a slab with two equivalent pristine surfaces (P), see Figure 3.7, the surface's energy can be calculated using equation 3.4 or the following equivalent expression:

$$\gamma_{PP} = \frac{1}{2} [\gamma_P + \gamma_P] = \gamma_P , \quad (3.5)$$

where  $\gamma_{PP}$  is the pristine-pristine surface energy.

In the same way, considering a slab made up of a pristine and a passivated surface (S), see Figure 3.7, we assume that we can completely decouple the pristine-passivated energy surface in two individual surface energies:

$$\gamma_{PS} = \frac{1}{2} [\gamma_P + \gamma_S] , \quad (3.6)$$

where  $\gamma_P$  and  $\gamma_S$  are the surface energies of the pristine and passivated surfaces correspondingly.

Following the same reasoning than the two previous equations, the surface's energy of any modified-passivated surfaces can be obtained using the equation:



$$\gamma_{MS} = \frac{1}{2} [\gamma_M + \gamma_S], \quad (3.7)$$

where  $\gamma_M$  is the energy of any modified surface of interest, see Figure 3.7. Using equations 3.6 and 3.5, we could rewrite the equation 3.7 in the following form:

$$\gamma_M = 2\gamma_{MS} - 2\gamma_{PS} + \gamma_P, \quad (3.8)$$

where all the surface energies  $\gamma$  are calculated with the equation 3.4. We used the equation 3.8 to calculate all the modified surfaces energies of the diamond slabs with a passivated surface. Although that this equation needs the computed values of the pristine surface's energy ( $\gamma_P$ ) and the pristine-passivated surface's energy ( $\gamma_{PS}$ ), the equation avoided the costly and exhaustive calculation of the slabs without passivation and agree with our computational simulations.

It is important to stress that this approximation is reliable when the slabs used in the calculations have reached convergence of both surface energy and electronic structure at the surface with respect to the slab thickness; moreover, the electronic structure at the middle of the slab reproduces the electronic structure of the bulk.

### Special study for selected surfaces

Once we calculated the surface energies of all the investigated slabs, we were able to select the most stable surfaces in order to perform a particular study calculating the energy work function and simulating different experimental techniques, such as UPS and STM.

1. To calculate the **work function** of all the selected surfaces, we began performing a DFT calculation of the total local potential of a structure in the  $z$ -direction. For this, we used the help of VASP and the LVTOT command. Next, we plotted the total local potential averaged on the  $xy$  plane along the  $z$ -direction, the plateau of the plot indicates the location of the vacuum level above the surface. Finally, we subtracted the vacuum level from the Fermi energy obtaining the energy work function  $\Phi$  of the studied structure.
2. In order to simulate the **UPS** spectra of the most stable surfaces, we performed the following procedure. First, we began using the NIST simulation software with the objective to obtain the inelastic mean free path region (IMFP) for a diamond surface. For this, we had to fit the energy and IMFP data obtained from NIST software<sup>51</sup> and get the minimum value of the fitting. Next, we used the photoionization cross-section data of C and H atoms obtained from Yeh and Lindau<sup>43</sup> to obtain

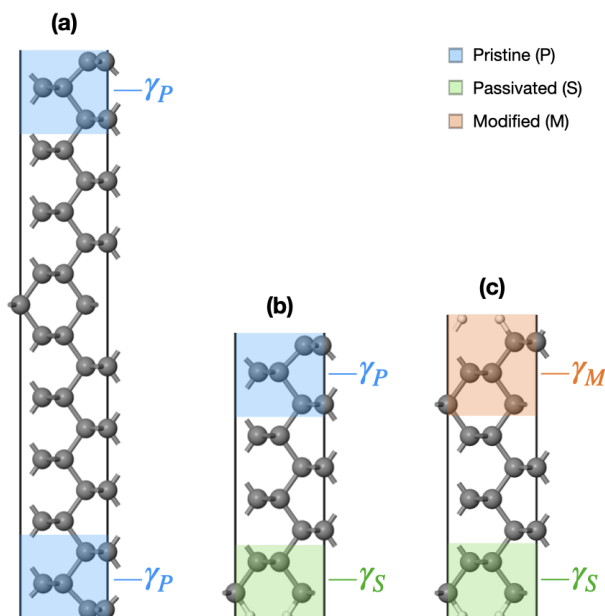


Figure 3.7: Slab examples for the (110) diamond family plane. (a) Slab composed of two equivalent pristine surfaces. (b) Slab composed of a pristine and a passivated surface. (c) Slab composed of a hydrogenated and a passivated surface. In the last case, we also called it modified structure because it is neither a pristine nor a passivated structure. In the Figure appears some  $\gamma$ 's referring to the surface's energy of each structure.

the optimal cross-section value. We combine these parameters with the previously computed PDOS of the most stable surfaces to obtain the simulated spectrum. Finally, using 40.82 eV photons which correspond to photoelectrons generated within approximately 5.74 Å of the outermost surface layers (3, 4, and 5 layers), we obtained the UPS spectra for the selected surfaces.

3. In order to obtain the simulated constant current mode **STM** images, we first had to use the bSKAN simulation software to perform a Tersoff-Hamann approximation with the output obtained from the VASP calculations. It is important to mention that some values of bias voltage were needed to perform a bSKAN simulation. Those values were selected based on the electronic structure analysis of the DOS of the selected surface. The outcome of the TH calculation using bSKAN were interpolated, from a 3D contour plot, we finally obtained the simulated constant current mode STM images with their respective line scan plots.

## Chapter 4

# Results & Discussion

### 4.1 The diamond crystal

The starting point of these studies is the prediction of the structural, electronic and mechanical properties of pristine bulk fcc diamond crystal using the SCAN+rVV10 xc functional. Table 4.1 summarizes the properties calculated according to the EOS and compares them with the properties obtained experimentally.

The electronic structure of the fcc diamond crystal was studied using the DOS and PDOS obtained from the wave-function projection of the valence electrons onto spherical harmonics. Figure 4.1 displays the SCAN+rVV10 computed DOS and PDOS for fcc diamond crystal. The system presents an insulator behavior because a bandgap  $E_g$  of 4.5 eV exists between the valence and conduction band. At this point, it is important to mention that the calculated bandgap presents an underestimation of 20%, which was already expected. The underestimation presented is because the quasiparticle bandgap (bandgap obtained experimentally) differs by a constant of  $\Delta_{xc}$  from the Kohn-Sham bandgap. Commonly, the underestimation is of 40% for LDA xc functionals and it can be reduced by the use of more accurate xc functionals such as hybrids. Moreover, it is important to mention that the C 2p state's contribution is greater than the C 2s states in regions near the Fermi energy level  $E_F$  (cf. Figure 4.1). Finally, the expected sp<sup>3</sup> hybridization between C 2s and C 2p orbitals for the atomic structure was successfully obtained.

Table 4.1: SCAN+rVV10 computed crystal structure and mechanical properties for fcc diamond crystal in comparison with experimental data. Here it is reported the lattice parameters ( $a$ ,  $b$ , and  $c$ ), lattice angles ( $\alpha$ ,  $\beta$ , and  $\gamma$ ), optimal volume ( $V_0$ ), bulk modulus ( $B_0$ ), bulk modulus pressure derivative ( $B'_0$ ), energy bandgap ( $E_g$ ), and the fractional sites ( $u$ ,  $v$ ,  $w$ ).

Property	Calculated (SCAN+rVV10)			Experiment <sup>26,52</sup>		
Space group	Fd $\bar{3}$ m			Fd $\bar{3}$ m		
$a = b = c$ (Å)	3.5490			3.5668		
$\alpha = \beta = \gamma$ (°)	90			90		
$V_0$ (Å <sup>3</sup> )	11.175			11.344		
$B_0$ (GPa)	458.8			443.0		
$B'_0$	3.65			3.67 <sup>53</sup>		
$E_g$ (eV)	4.5			5.4		
Fractional sites	$u$	$v$	$w$	$u$	$v$	$w$
C (1)	0.00	0.00	0.00	0.00	0.00	0.00
C (2)	0.25	0.25	0.25	0.25	0.25	0.25

## 4.2 The C(110) diamond surfaces

### 4.2.1 The C(110) surface energies and electronic properties

In the first step of the C(110) surface calculations, we explored different surface structure reconstructions. In general, the surfaces explored were: pristine, pristine with surface C vacancies, surface hydrogenated, hydrogenated with surface H and C vacancies. The pristine surface structure C(110)-(1×1) did not present any variation in their structure or surface energy with respect to reconstructions such as the C(110)-(1×2) and the C(110)-(2×2), then we use the pristine C(110)-(1×1) structure as reference pristine surface to explore all the defective surface structures and reconstructions.

To determine which surfaces have the lower surface energy  $\gamma$  and hence the more stable surfaces for any given chemical potential of H ( $\mu_H$ ), a surface energy was computed according to Equations 3.4 and 3.8. Figure 4.2 displays the SCAN+rVV10 computed surface energies for all the reconstructions and defective surfaces considered in this study.

The most expected surface for  $\mu_H < -5.7$  eV is the pristine C(110)-(1×1) while for  $\mu_H > -4.9$  eV is

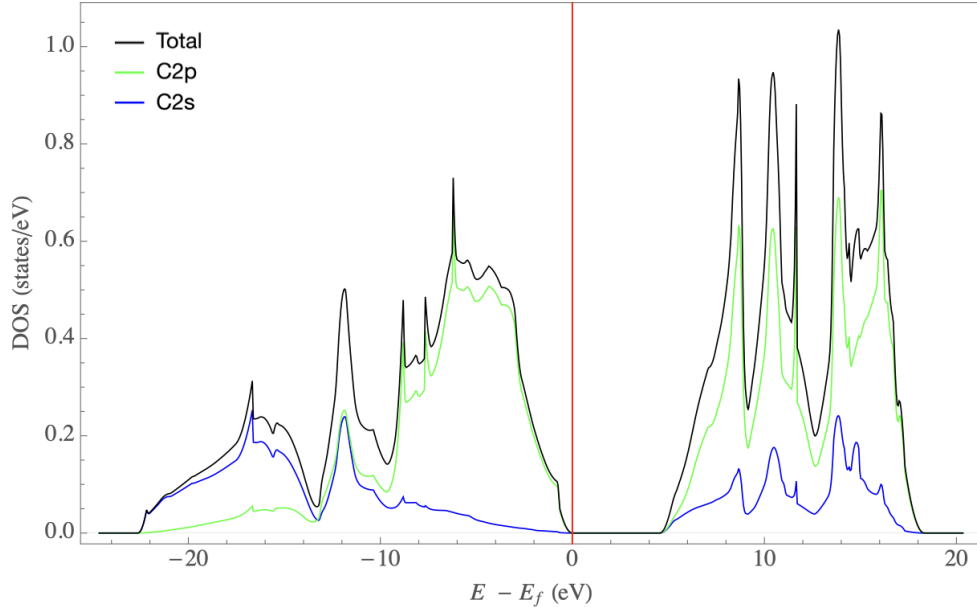


Figure 4.1: SCAN+rVV10 computed DOS and PDOS for the fcc diamond crystal structure. In this Figure, the green (blue) line represents the PDOS of C 2p (C 2s) states; and the black line is the total DOS. The Fermi energy level  $E_F$  is shifted to 0 eV and it is represented by the vertical red line.

the fully hydrogenated surface C(110)-(1×1)H. Within the range of  $-5.7 < \mu_H < -4.9$  eV, we observe the most stable surface reconstructions show magnetization at the surface. Moreover, within this region exist some competitive magnetic phases; these results are better visualized in Figure 4.3. Based in these results, the following sections will analyse in detail the electronic structure of C(110)-(1×1), C(110)-(1×1)H, C(110)-(2×1)H+2H<sub>v</sub>, C(110)-(2×1)H+2H<sub>v</sub>-AFM, C(110)-(2×1)H+3H<sub>v</sub>-M1 and C(110)-(2×1)H+3H<sub>v</sub>-M2 surfaces; here M and AFM stands for magnetic and antiferromagnetic solutions. Table 4.2 shows a summary of the SCAN+rVV10 predictions for the work functions and bandgaps; the C(110)-(1×1) and C(110)-(2×1)H+2H<sub>v</sub> surfaces have metallic state and in all the cases,  $E_g$  is lower than the  $E_g$  of diamond of 4.5 eV. It is important to stress that despite C(110)-(2×1)H+2H<sub>v</sub> and C(110)-(2×1)H+2H<sub>v</sub>-AFM have practically the same atomic structure, the latter is an insulator. This interesting prediction could be tested with scanning tunneling spectroscopy. Moreover, notice that  $\Phi$  for the pristine C(110)-(1×1) surface has the highest value of 6.03 eV and we observe a trend where the fully hydrogenated surface, C(110)-(1×1)H, has the lowest  $\Phi$  and it increases as the H coverage is decreased.

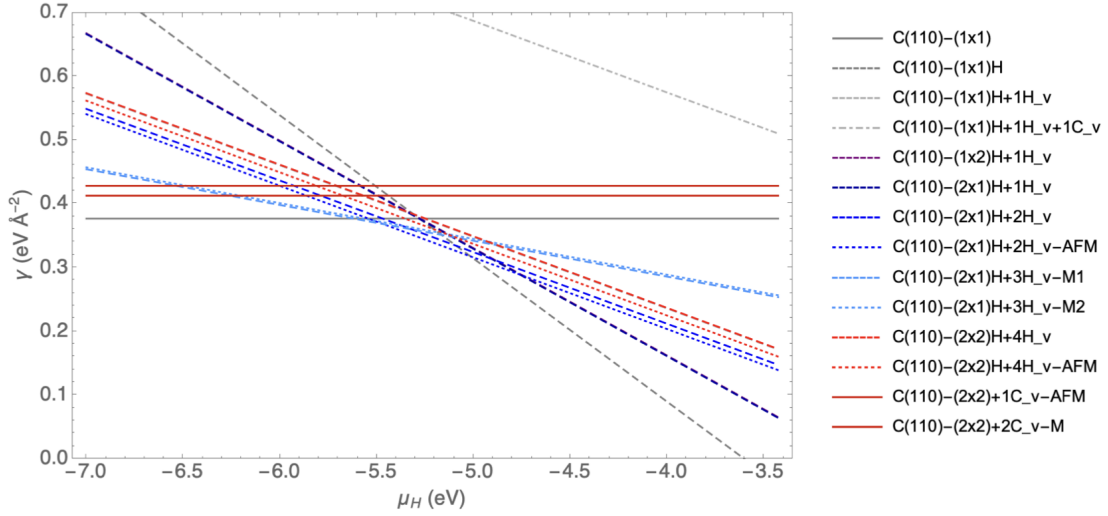


Figure 4.2: SCAN+rVV10 computed surface energy of the C(110) surfaces considered in this study. The different colors (gray, purple, blue, and red) denote the number of cell repetitions ( $1\times 1$ ,  $1\times 2$ ,  $2\times 1$ , and  $2\times 2$ ) in the  $x$  and  $y$ -direction. The structures that only have carbon atoms on the surface are represented by solid energy lines; while the dashed or dotted lines represent the surfaces with carbon and hydrogen atoms. In the inset, the surface notation for surface carbon and hydrogen vacancies is  $C_v$  and  $H_v$ , respectively.

Table 4.2: SCAN+rVV10 computed work functions ( $\Phi$ ) and bandgaps ( $E_g$ ) for the C(110) surfaces considered in this study. Additionally keep in mind that predicted  $E_g$  for bulk fcc diamond is 4.5 eV and the experimental value is 5.4 eV.

Surface	$\Phi$ (eV)	$E_g$ (eV)
C(110)-(1 $\times$ 1)	6.03	0.00
C(110)-(1 $\times$ 1)H	3.18	2.51
C(110)-(2 $\times$ 1)H+2H <sub>v</sub>	4.23	0.00
C(110)-(2 $\times$ 1)H+2H <sub>v</sub> -AFM	4.70	1.36
C(110)-(2 $\times$ 1)H+3H <sub>v</sub> -M1	4.79	0.73
C(110)-(2 $\times$ 1)H+3H <sub>v</sub> -M2	4.81	0.86

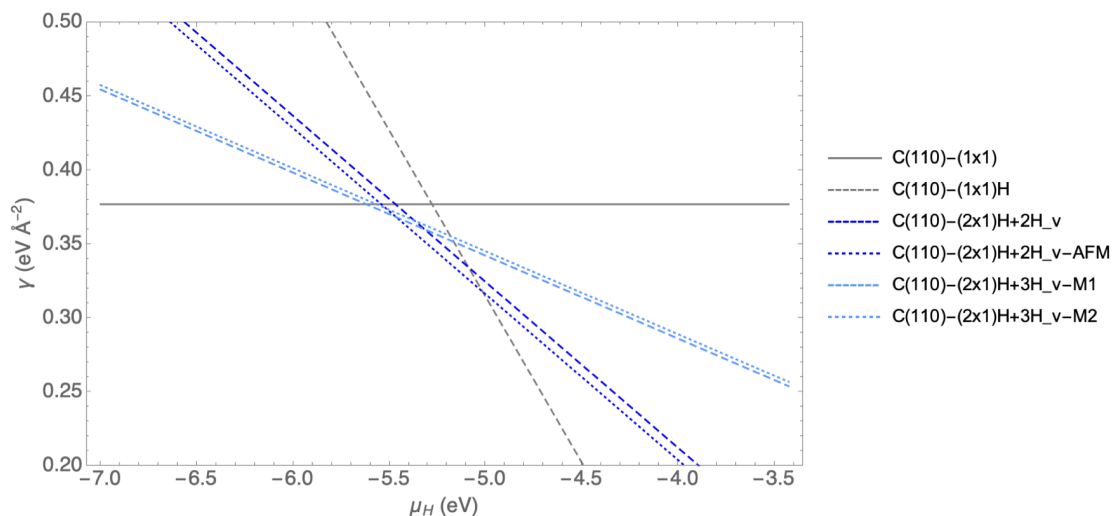


Figure 4.3: Close-up of SCAN+rVV10 computed surface energy featuring the most stable C(110) surface structures. The different colors (gray and blue) denote the number of cell repetitions ( $1\times 1$  and  $2\times 1$ ) in the  $x$  and  $y$ -direction. The structures that only have carbon atoms on the surface are represented by solid energy lines; while the dashed or dotted lines represent the surfaces with carbon and hydrogen atoms. In the inset, the surface notation for surface carbon and hydrogen vacancies is  $C_v$  and  $H_v$ , respectively.

## 4.2.2 The C(110)-(1 $\times$ 1) surface

### Atomic and electronic structure

Figure 4.4 displays the computed results of the atomic and electronic structure of the C(110)-(1 $\times$ 1) surface. Figure 4.4(a) and (b) show the atomic reconstruction at the surface. After full relaxation, the atomic configuration shows that the inter-atomic bond lengths of the surface were shorter compared with the bulk structure. Note the inward relaxation of the topmost L1 layer. Figure 4.4(c) shows the computed PDOS for layers L1, L2 and L3 corresponding to Figure 4.4(b). The results exhibit a metallic behavior but the bulk bandgap is restored for deeper layers (not shown in Fig. 4.4(c)). The electronic structure of L1 at  $E_F$  is mainly composed of C 2p states and minor contribution of C 2s states.

### Simulated ultraviolet photoelectron spectroscopy UPS for the C(110)-(1 $\times$ 1) surface

Figure 4.5 displays the simulated UPS spectrum for the C(110)-(1 $\times$ 1) surface using 40.82 eV photons which correspond to photoelectrons generated within approximately 5.74 Å of the outermost surface layers—i.e.,

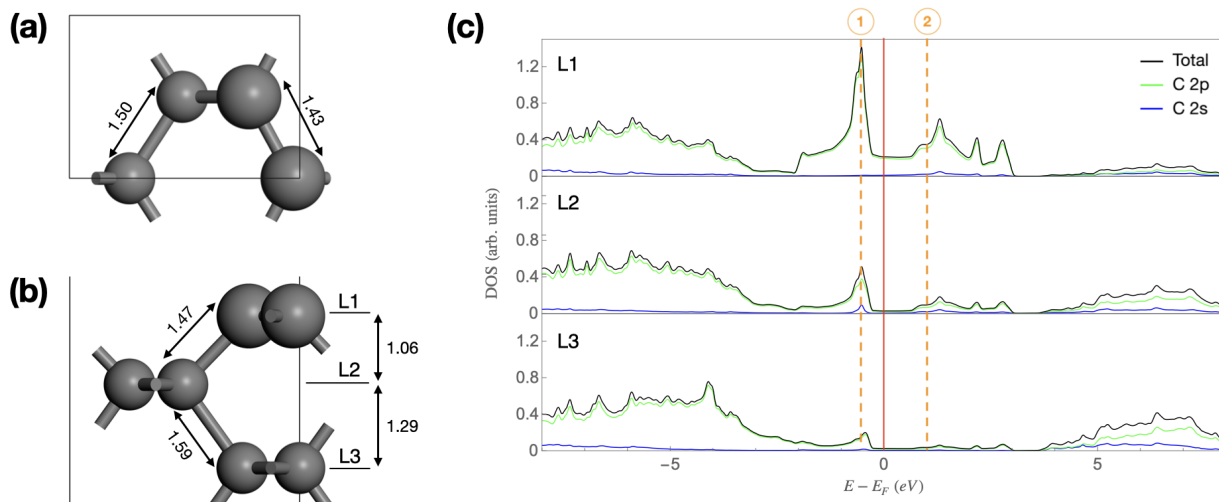


Figure 4.4: SCAN+rVV10 computed atomic and electronic structure of C(110)-(1 $\times$ 1). (a) top and (b) side view of the three first topmost layers; the C atoms are represented by grey spheres and the surface C atoms are depicted by bigger spheres to contrast with the subsurface C atoms; the black lines delimits the surface unit cell. (c) PDOS of the three surface layers, the surface has metallic character. The Fermi level is shifted to 0 eV and is represented by the vertical red line. The ranges of integrated energies to obtain the STM images (a and b) are represented from Fermi level to the dashed orange lines (1 and 2).

the five outermost atomic layers. The spectrum shows main peaks at  $\sim -0.8$  eV,  $-5.7$  eV and  $-12.6$  eV; as well as a shoulder at  $-9.5$  eV. The decomposed UPS predicts that the spectrum is composed mainly by C 2p states; while below  $-14.2$  eV, the spectrum has a major contribution of C 2s states. The simulated UPS nicely reproduces the experimental UPS spectrum by Franz et al.<sup>54</sup> obtained from a natural diamond (110) with 40.82 eV photons after hydrogen-plasma annealing at 870 °C, as depicted in the same Figure 4.5. These results provide a strong support to the level of prediction of the method applied in this study.

### Simulated constant current mode STM images for the C(110)-(1 $\times$ 1) surface

Figure 4.6 displays the simulated constant current mode STM images and linescans for the C(110)-(1 $\times$ 1) surface. The STM topography for  $V_{\text{BIAS}} = -0.6$  V (Fig. 4.6(a)) shows an arrangement of bright spots that are assigned to the topmost C atoms in alternating sites along the  $y$ -direction; the dark spots are assigned to alternating sites where either no surface or subsurface C atoms are present. A detailed analysis of the electronic structure for the occupied states attributes the bright spots to C 2p<sub>z</sub> surface states that protrudes



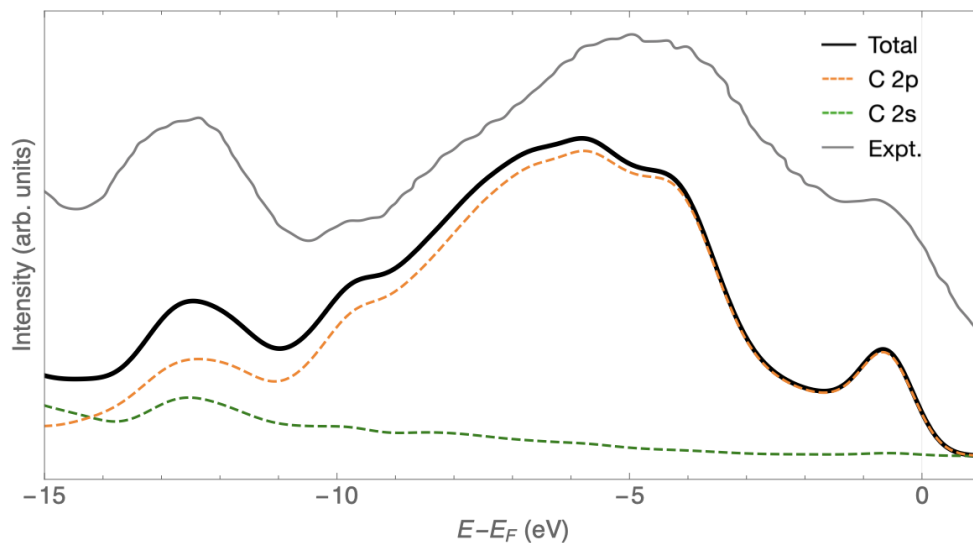


Figure 4.5: Simulated UPS spectrum for the C(110)-(1 $\times$ 1) surface using 40.82 eV photons. The experimental spectrum obtained with the same photons energy (gray line) was adapted from Ref. 54 and displayed for direct comparison.

into the vacuum. The corresponding linescan along the A-A' profile (Fig. 4.6(c)) shows a corrugation of  $\sim 0.3$  Å. The STM topography for  $V_{\text{BIAS}} = +1.0$  V (Fig. 4.6(b)), the bright columns along  $y$ -direction are identified as subsurface C sites and the corresponding linescan along A-A' profile (Fig. 4.6(d)) reveals a corrugation of 0.4 Å. Comparing the simulated STM topographies for positive and negative bias, we observe a change of contrast.

### 4.2.3 The C(110)-(1 $\times$ 1)H surface

#### Atomic and electronic structure

Figure 4.7 displays the computed results of the atomic and electronic structure of the C(110)-(1 $\times$ 1)H surface. This surface is fully covered by H atoms on the surface. Figure 4.7(a) and (b) show the atomic reconstruction at the surface. After full relaxation, the atomic configuration shows that the inter-atomic bond lengths of the surface were shorter compared with the bulk structure, notice the inward relaxation of the topmost L1 layer. The H atoms are bonded to the surface C atoms with a distance of 1.09 Å and tilted an angle of  $57^\circ$  with respect to the  $x$ -axis. Figure 4.7(c) shows the computed PDOS for layers L1, L2 and L3 corresponding to Figure 4.7(b); the results exhibit a bandgap opening at the surface of 2.51 eV

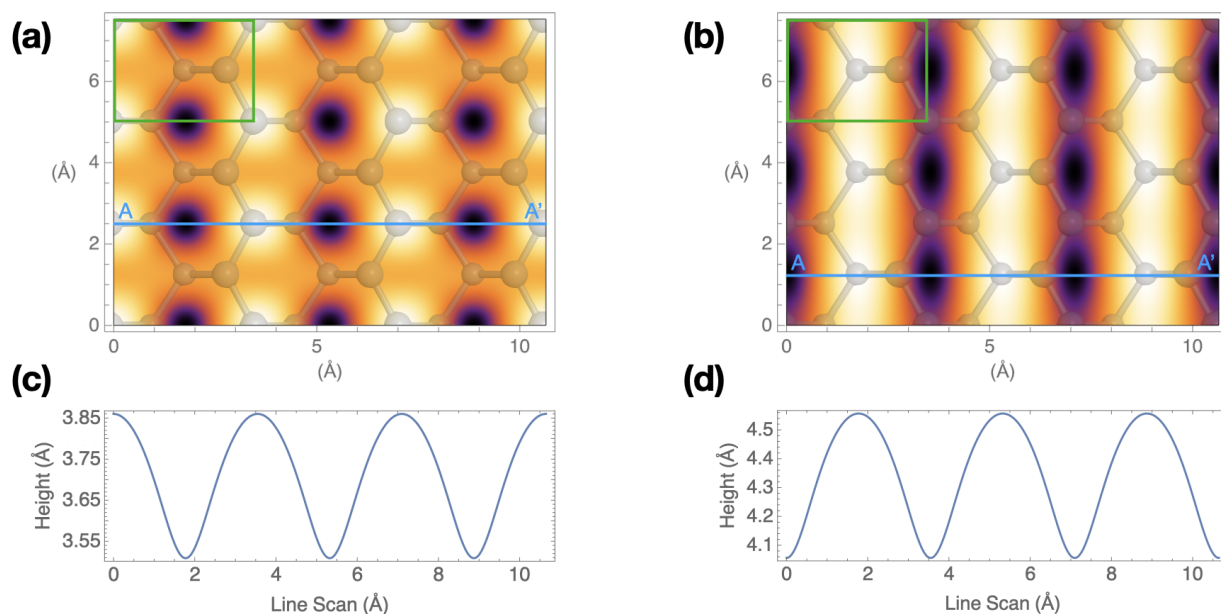


Figure 4.6: Computed constant current mode STM image and linescan along the A-A' profile for the C(110)-(1×1) surface with  $V_{\text{BIAS}}$  of (a, c) -0.6 V, occupied states and (b, d) +1.0 V, unoccupied states. The STM images are colored such that bright (dark) colors of the isocurrent topology represent the protruding (receding) parts of the topology. In both images is superimposed the atomic structure of the topmost layers where the C atoms are represented by grey spheres and the surface C atoms are depicted by bigger spheres; the green box delimits the surface unit cell.

contrasting the metallic state of the pristine C(110)-(1×1). The bulk bandgap for deeper layers is restored to the bulk value (not shown in Fig. 4.7(c)). The electronic structure of L1 around  $E_F$  is mainly composed of C 2p states with minor contributions of C 2s and H 1s states.

### Simulated ultraviolet photoelectron spectroscopy UPS for the C(110)-(1×1)H surface

Figure 4.8 displays the simulated UPS spectrum for C(110)-(1×1)H surface using 40.82 eV photons which correspond to photoelectrons generated within approximately 5.74 Å of the outermost surface layers—i.e., the 4 outermost atomic layers. The spectrum shows main peaks at  $\sim$ -3.7 eV, -5.8 eV and -12 eV. The decomposed simulated UPS spectrum predicts that the dominant contributions are from the C 2p states while C 2s states overcome the C 2p states below -13.3 eV. The H 1s states practically have negligible contribution in all range of energies. The simulated UPS reproduces well the experimental spectrum by

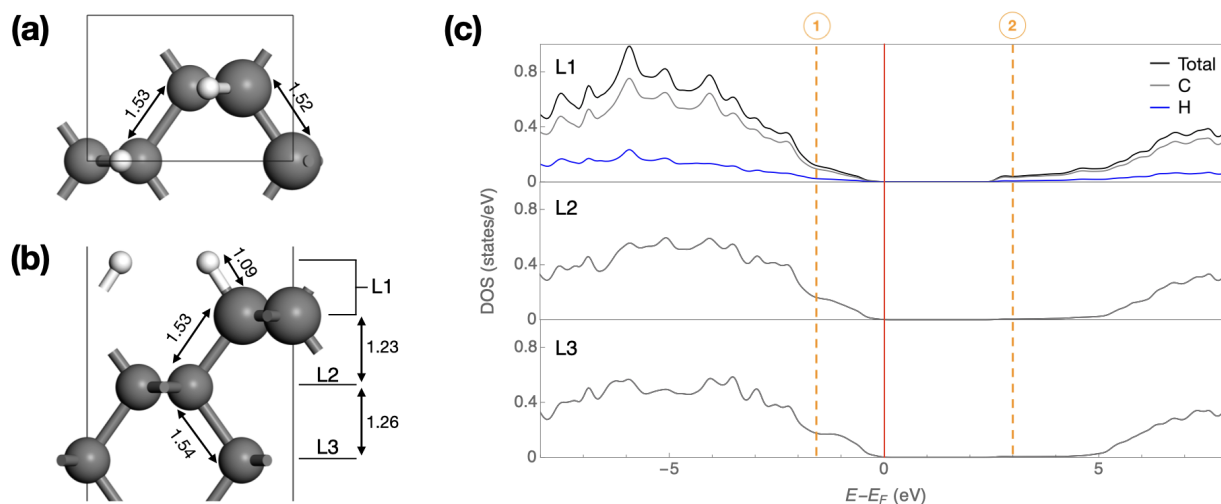


Figure 4.7: SCAN+rVV10 computed atomic and electronic structure of C(110)-(1 $\times$ 1)H. (a) top and (b) side view of the three first topmost layers; the C (H) atoms are represented by grey (white) spheres and the surface C atoms are depicted by larger spheres to contrast with the subsurface C atoms; the black lines delimits the surface unit cell. (c) DOS of the three surface layers, the surface has insulator character. The Fermi level is shifted to 0 eV and is represented by the vertical red line; notice this surface is predicted to have an insulating state. The ranges of integrated energies to obtain the STM images (a and b) are represented from Fermi level to the dashed orange lines (1 and 2).

Francz et al.<sup>54</sup> obtained from a natural diamond (110) with 40.82 eV photons after surface passivisation by atomic deuterium, as depicted in the same Figure 4.8.

### Simulated constant current mode STM images for the C(110)-(1 $\times$ 1)H surface

Figure 4.9 displays the simulated constant current mode STM images and linescans for the C(110)-(1 $\times$ 1)H surface. The STM topography for  $V_{\text{BIAS}} = -1.68$  V (Fig. 4.9(a)) shows bright columns that are assigned to the subsurface C atoms along the  $y$ -direction. The corresponding linescan along the A-A' profile (Fig. 4.9(c)) shows a corrugation of  $\sim 0.01$  Å. The STM topography for  $V_{\text{BIAS}} = +3.0$  V (Fig. 4.9(b)) displays an arrangement of alternating primary and secondary bright spots where no surface C or subsurface C or H atoms are present; the dark spots are assigned to H sites. The corresponding linescan along A-A' profile (Fig. 4.9(d)) reveals a corrugation of 0.015 Å. Comparing the simulated STM topographies for positive and negative bias, we observe a change of contrast, this is similar to the results for pristine C(110)-(1 $\times$ 1)

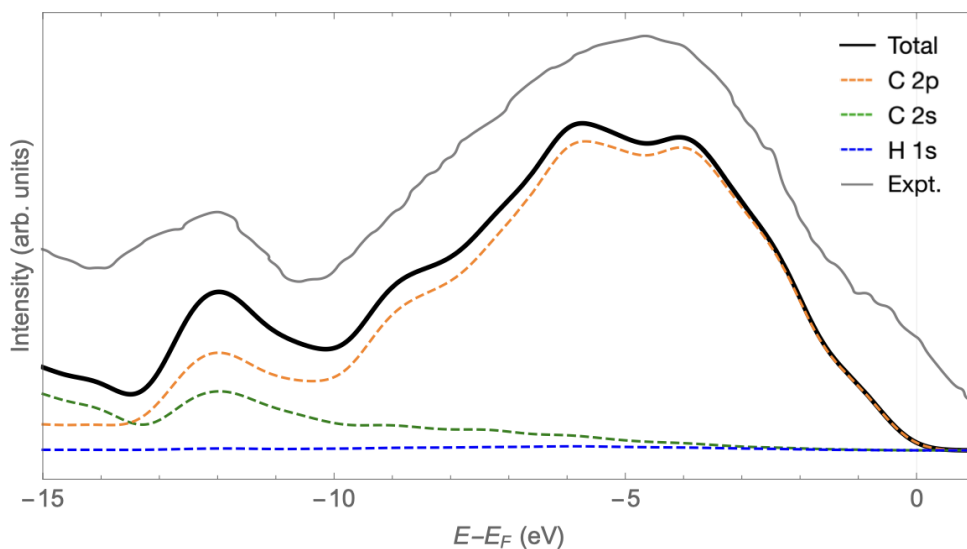


Figure 4.8: Simulated UPS spectrum for the C(110)-(1×1)H surface using 40.82 eV photons. Notice the composition of the spectrum, basically the H 1s states are invisible or has negligible contribution to the spectrum. The experimental spectrum of C(110) D-saturated surface obtained with the same photons energy (gray line) was adapted from Ref. 54 and displayed for direct comparison.

case.

#### 4.2.4 The C(110)-(2×1)H+2H<sub>v</sub> surface

##### Atomic and electronic structure

Figure 4.10 displays the computed results of the atomic and electronic structure of the C(110)-(2×1)H+2H<sub>v</sub> surface. This surface was built from the C(110)-(1×1)H repeated 2 fold along the  $x$ -axis and extracting two H that belong to the same column along the  $y$ -direction. Figure 4.10(a) and (b) show the atomic reconstruction at the surface. After full relaxation, the top layer L1 moves inward, the H-C bond length is 1.10 Å and the H atoms form an angle of 52.3° with respect to the  $x$ -axis. Figure 4.10(c) shows the computed PDOS for layers L1, L2 and L3 corresponding to Figure 4.10(b). These results exhibit a metallic behavior but the bulk bandgap is restored for deeper layers (not shown in Fig. 4.10(c)). The electronic structure of L1 at  $E_F$  is mainly composed of C 2p states.

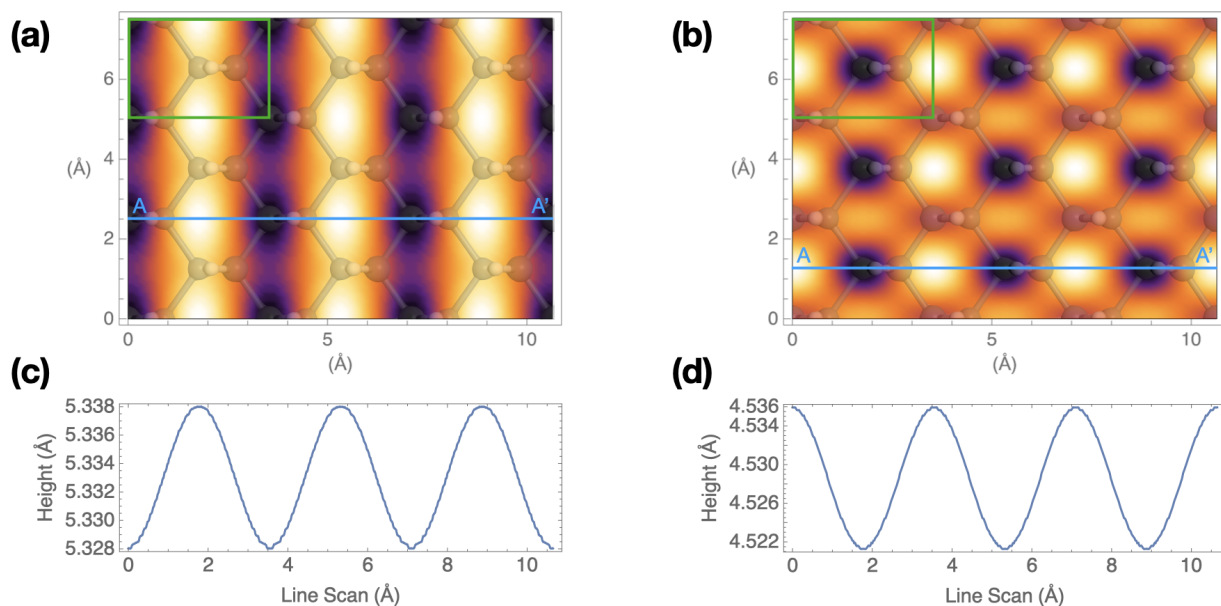


Figure 4.9: Computed constant current mode STM image and linescan along the A-A' profile for the C(110)-(1 $\times$ 1)H surface with  $V_{\text{BIAS}}$  of (a, c) -1.68 V, occupied states and (b, d) +3.0 V, unoccupied states. The STM images are colored such that bright (dark) colors of the isocurrent topology represent the protruding (receding) parts of the topology. In both images is superimposed the atomic structure of the topmost layers where the C (H) atoms are represented by grey (white) spheres; the green box delimits the surface unit cell.

### Simulated ultraviolet photoelectron spectroscopy UPS for the C(110)-(1 $\times$ 1)H+2H<sub>v</sub> surface

Figure 4.11 displays the simulated UPS spectrum for C(110)-(2 $\times$ 1)H+2H<sub>v</sub> surface using 40.82 eV photons. The spectrum shows peaks at -1.1 eV and -12.5 eV, and a broad peak with maximum value at  $\sim$ -5 eV. The decomposed UPS predicts that dominant contribution are from the C 2p states while C 2s states overcome the C 2p state below -14 eV; the H 1s states practically have negligible contribution in all range of energies. The simulated UPS show also some similarity with the experimental UPS spectrum of C(110) passivized with atomic deuterium by Francz *et al.*<sup>54</sup> obtained with 40.82 eV photons, as depicted in the same Figure 4.11; this computed surface is a expected candidate to explain the observed experimental spectrum for H-terminated C(110) surfaces.

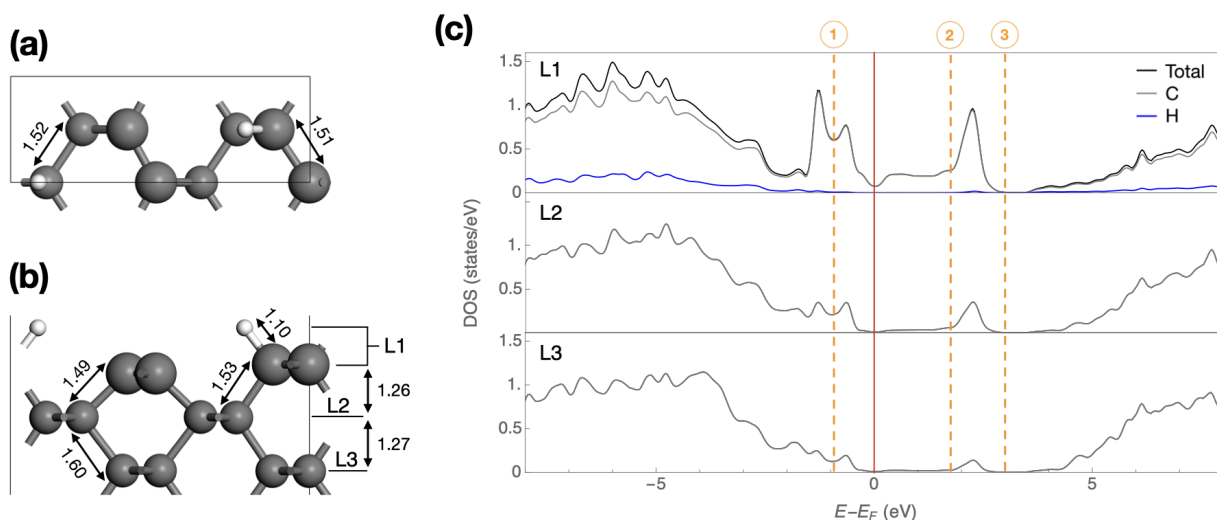


Figure 4.10: SCAN+rVV10 computed atomic and electronic structure of C(110)-(2 $\times$ 1)H+2H<sub>v</sub>. (a) top and (b) side view of the three first topmost layers; the C (H) atoms are represented by grey (white) spheres and the surface C atoms are depicted by bigger spheres to contrast with the subsurface C atoms; the black lines delimits the surface unit cell. (c) DOS of the three surface layers, the surface has metallic character. The Fermi level is shifted to 0 eV and is represented by the vertical red line. The ranges of integrated energies to obtain the STM images (a, b and e) are represented from Fermi level to the dashed orange lines (1, 2 and 3).

### Simulated constant current mode STM images for the C(110)-(1 $\times$ 1)H+2H<sub>v</sub> surface

Figure 4.12 displays the simulated constant current mode STM images and linescans for C(110)-(2 $\times$ 1)H+2H<sub>v</sub> surface. The STM topography for  $V_{\text{BIAS}} = -0.95$  V (Fig. 4.12(a)) shows bright columns along  $y$ -direction which maximum is identified as the three coordinated surface C atoms. The corresponding linescan along A-A' profile (Fig. 4.12(c)) reveals a corrugation of 1.1 Å. The STM topography for  $V_{\text{BIAS}} = +1.76$  V (Fig. 4.12(b)) presents an arrangement of bright and darkest spots along  $y$ -direction that are assigned to the C-H columns; in addition, the other bright spots are assigned to subsurface C columns along the  $y$ -direction. The secondary dark spots are located on the projected hexagons formed by surface and subsurface C sites. The corresponding linescan along the A-A' profile (Fig. 4.12(d)) shows a corrugation of  $\sim 0.42$  Å. Finally, the STM topography for  $V_{\text{BIAS}} = +3.0$  V (Fig. 4.12(e)) exhibits pairs of bright columns along  $y$ -direction identified as subsurface C and C-H sites while the dark columns are assigned to surface C columns. The corresponding linescan along A-A' profile (Fig. 4.12(f)) reveals a corrugation of 0.68 Å.

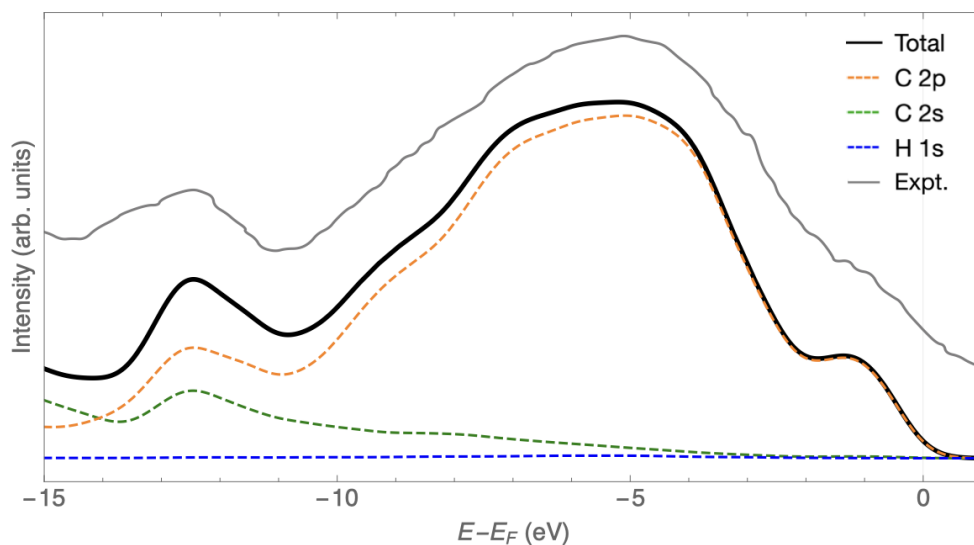


Figure 4.11: Simulated UPS spectrum for the C(110)-(2 $\times$ 1)H+2H<sub>v</sub> surface using 40.82 eV photons. The experimental spectrum of C(110) D-saturated surface obtained with the same photons energy (gray line) was adapted from Ref. 54 and displayed for direct comparison.

#### 4.2.5 The C(110)-(2 $\times$ 1)H+2H<sub>v</sub>-AFM surface

##### Atomic and electronic structure

Our spin polarized calculations yield C(110)-(2 $\times$ 1)H+2H<sub>v</sub> with antiferromagnetic state at the surface that is lower in energy by 8.29 meV/Å<sup>2</sup> with respect to the non magnetic case (cf. Sec. 4.2.4). Figure 4.13 displays the computed results of the atomic and electronic structure of the C(110)-(2 $\times$ 1)H+2H<sub>v</sub>-AFM surface. Figure 4.13(a) and (b) show the atomic reconstruction at the surface; after full relaxation, the atomic configuration shows similar reconstruction as the non magnetic case (cf. Fig. 4.10). In addition, Figure 4.13(a) presents the magnetization of -0.25 and 0.25  $\mu_B$  on the topmost C sites with H vacancies, exhibiting an AFM configuration. Figure 4.13(c) shows the computed spin-polarized (SP) PDOS for layers L1, L2 and L3 corresponding to Figure 4.13(b); the results suggest a stable AFM state with a bandgap opening of 1.36 eV in comparison with the metallic solution of the non magnetic state (cf. Fig. 4.10(c)). The electronic structure of L1 around  $E_F$  is mainly composed of C 2p states with minor contributions of C 2s and H 1s states.

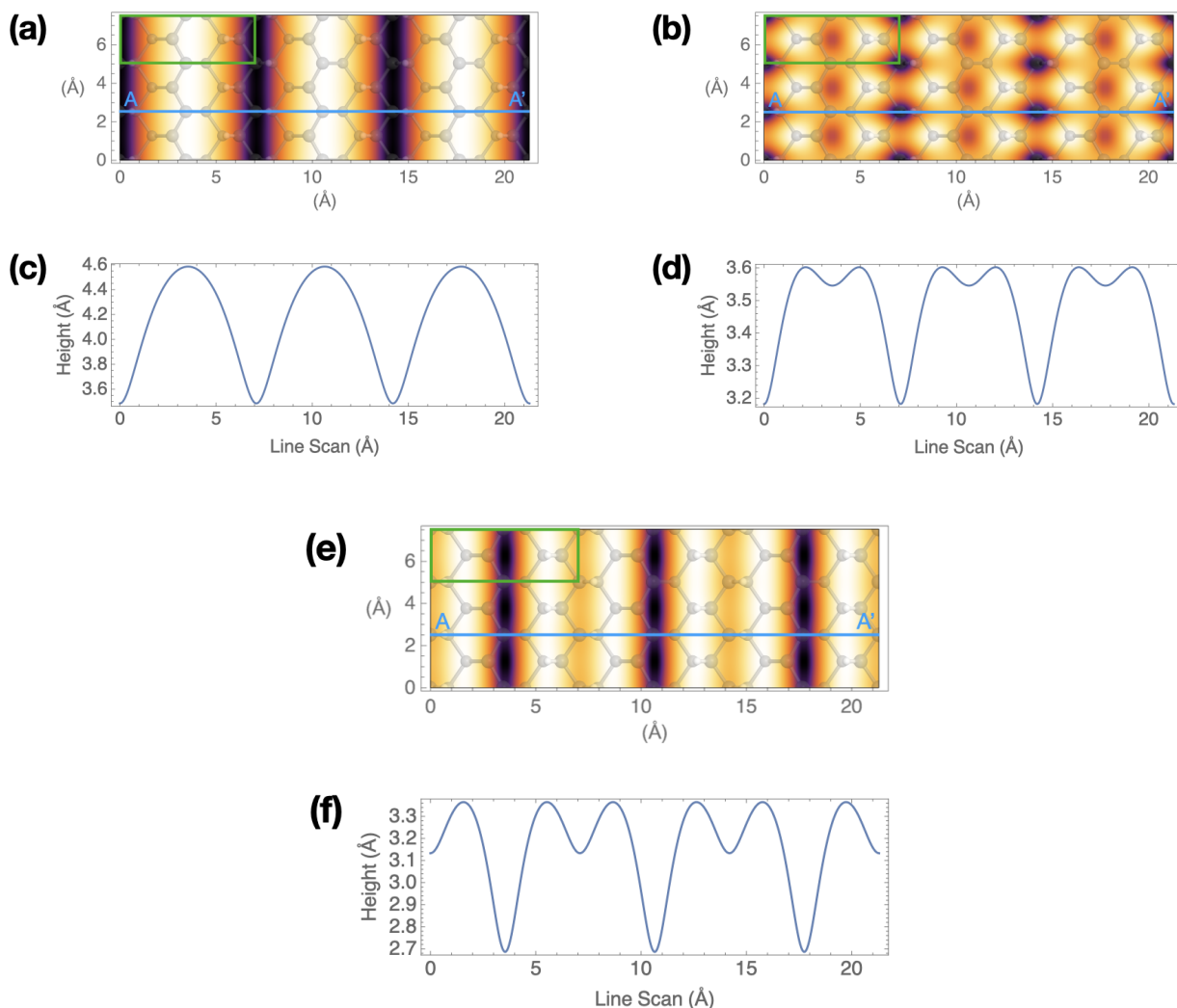


Figure 4.12: Computed constant current mode STM image and linescan along the A-A' profile for the C(110)-(2 $\times$ 1)H+2H<sub>v</sub> surface with  $V_{BIAS}$  of (a, c) -0.95 V, occupied states and (b, d) +1.76 V, (e, f) +3.0 V, unoccupied states. The STM images are colored such that bright (dark) colors of the isocurrent topology represent the protruding (receding) parts of the topology. In the three images is superimposed the atomic structure of the topmost layers where the C (H) atoms are represented by grey (white) spheres and the surface C atoms are depicted by bigger spheres; the green box delimits the surface unit cell.



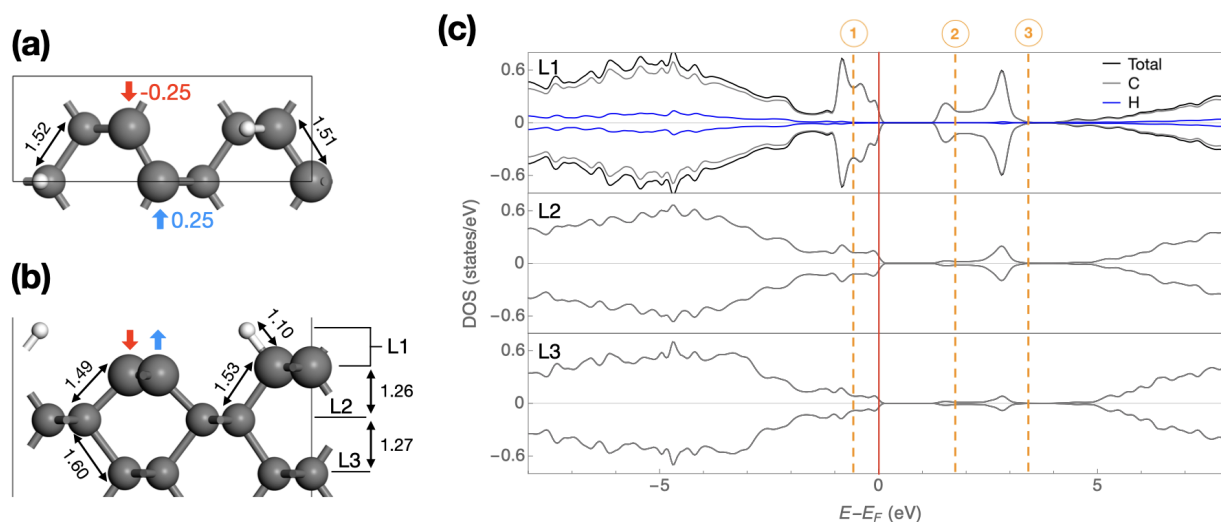


Figure 4.13: SCAN+rVV10 computed atomic and electronic structure of C(110)-(2 $\times$ 1)H+2H<sub>v</sub>-AFM. (a) top and (b) side view of the three first topmost layers; the C (H) atoms are represented by grey (white) spheres and the surface C atoms are depicted by bigger spheres to contrast with the subsurface C atoms; the black lines delimits the surface unit cell; the blue and red arrows shows the magnetization in  $\mu_B$  on the C surface atoms. (c) SP-PDOS of the three surface layers, the surface has insulator character; the spin up (down) are plotted with positive (negative) values on the DOS axis. The Fermi level is shifted to 0 eV and is represented by the vertical red line. The ranges of integrated energies to obtain the STM images (a, b and c) are represented from Fermi level to the dashed orange lines (1, 2 and 3).

### Simulated ultraviolet photoelectron spectroscopy UPS for the C(110)-(2 $\times$ 1)H+2H<sub>v</sub>-AFM surface

Figure 4.14 displays the simulated UPS spectrum for C(110)-(2 $\times$ 1)H+2H<sub>v</sub>-AFM surface using 40.82 eV photons. The spectrum shows main peaks at  $\sim$ -0.8 eV, -4.8 eV and -11.9 eV. The decomposed UPS predicts that above -10.2 eV, the spectrum is composed mainly by C 2p states; while below -10.2 eV, the spectrum is composed of both C 2s and 2p states. The simulated UPS show also some similarities with the experimental UPS spectrum of C(110) passivated with atomic deuterium by Francz *et al.*<sup>54</sup> obtained with 40.82 eV photons as depicted in the same Figure 4.14.

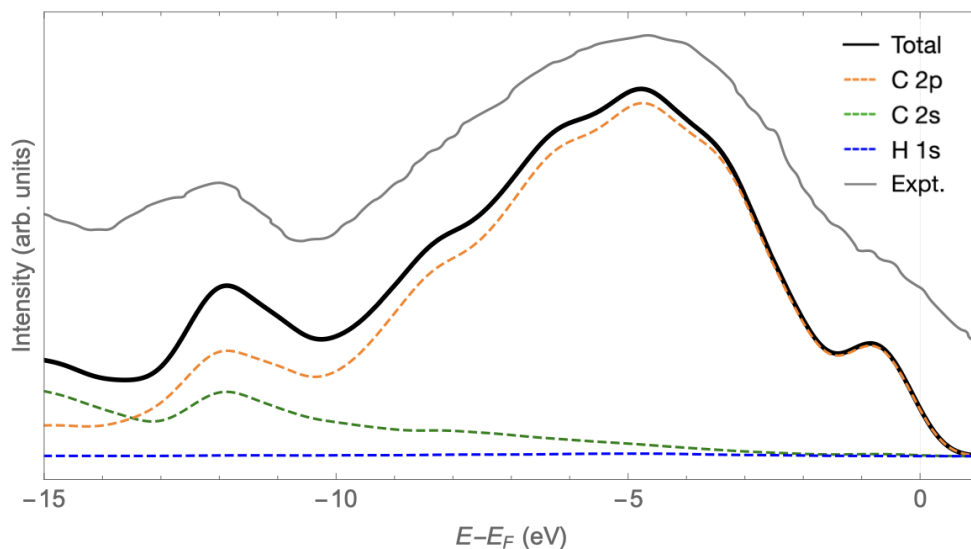


Figure 4.14: Simulated UPS spectrum for the C(110)-(2 $\times$ 1)H+2H<sub>v</sub>-AFM surface using 40.82 eV photons. The experimental spectrum of C(110) D-saturated surface obtained with the same photons energy (gray line) was adapted from Ref. 54 and displayed for direct comparison.

#### Simulated constant current mode STM images for the C(110)-(2 $\times$ 1)H+2H<sub>v</sub>-AFM surface

The STM topography for  $V_{\text{BIAS}} = -0.6$  V (Fig. 4.15(a)) shows bright columns along  $y$ -direction which maximum are centered on the magnetic surface C atoms. The corresponding linescan along A-A' profile (Fig. 4.15(c)) reveals a corrugation of 0.85 Å. The STM topography for  $V_{\text{BIAS}} = +1.8$  V (Fig. 4.15(b)) presents an arrangement of elongated bright spots that are assigned to the magnetic surface C atoms in alternating sites along the  $y$ -direction; the dark spots are assigned to alternating C-H sites. The corresponding linescan along the A-A' profile (Fig. 4.15(d)) shows a corrugation of  $\sim 1.2$  Å. Finally, the STM topography for  $V_{\text{BIAS}} = +3.42$  V (Fig. 4.15(e)) exhibits pairs of bright columns along  $y$ -direction identified as subsurface C and H sites while the dark stripes are assigned to surface C-H columns, the secondary dark columns are assigned to the magnetic surface C atoms along  $y$ -direction. The corresponding linescan along A-A' profile (Fig. 4.15(f)) reveals a corrugation of 0.4 Å.

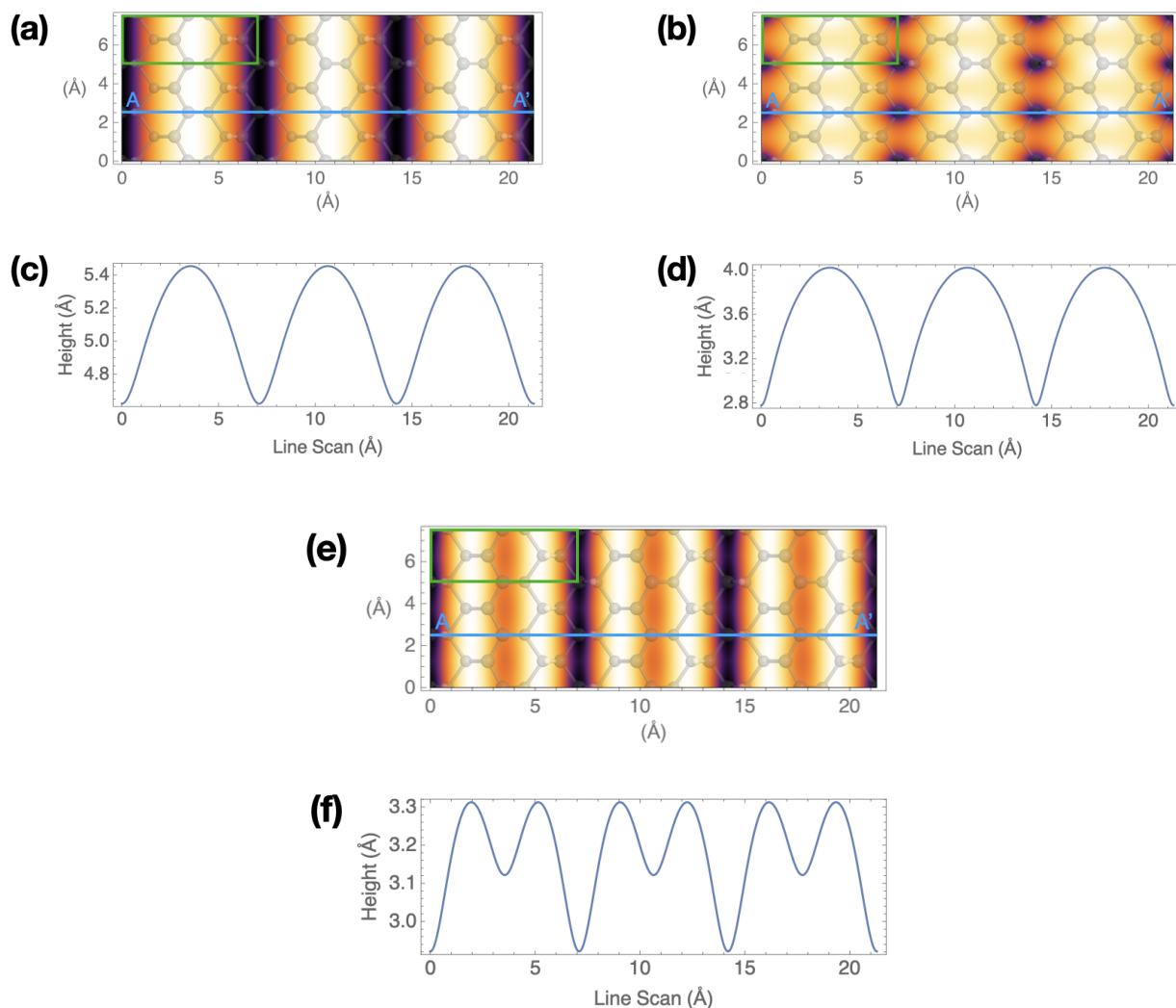


Figure 4.15: Computed constant current mode STM image and linescan along the A-A' profile for the C(110)-(2 $\times$ 1)H+2H<sub>v</sub>-AFM surface with  $V_{\text{BIAS}}$  of (a, c) -0.6 V, occupied states and (b, d) +1.8 V, (e, f) +3.42 V, unoccupied states. The STM images are colored such that bright (dark) colors of the isocurrent topology represent the protruding (receding) parts of the topology. In the three images is superimposed the atomic structure of the topmost layers where the C (H) atoms are represented by grey (white) spheres and the surface C atoms are depicted by bigger spheres; the green box delimits the surface unit cell.

### 4.2.6 The C(110)-(2×1)H+3H<sub>v</sub>-M1 surface

#### Atomic and electronic structure

Starting from C(110)-(2×1)H surface we extracted three H atoms. In order to get the lowest electronic structure configurations, SP calculations were employed. Figure 4.16 displays the computed results of the atomic and electronic structure of the C(110)-(2×1)H+3H<sub>v</sub>-M1 surface where M1 denotes here the magnetic solution 1. Figure 4.16(a) and (b) show the atomic reconstruction at the surface. After full relaxation, the top layer L1 moves inward, the H-C bond length is 1.09 Å and the H is attached to C with a tilted angle of 52.3°. Interestingly the C atom of this site is found 0.21 Å higher with respect to the other surface C atoms. Moreover, these atoms present a magnetization of +0.28, +0.46 and -0.26 μ<sub>B</sub>. Figure 4.16(c) shows the computed SP-PDOS for layers L1, L2 and L3 corresponding to Figure 4.16(b). The results exhibit a magnetic insulator state with a  $E_g = 0.73$  eV. The electronic structure of L1 around  $E_F$  is mainly composed of C 2p states.

#### Simulated ultraviolet photoelectron spectroscopy UPS for the C(110)-(2×1)H+3H<sub>v</sub>-M1 surface

Figure 4.17 displays the simulated UPS spectrum for C(110)-(2×1)H+3H<sub>v</sub>-M1 surface using 40.82 eV photons. The spectrum shows main peaks at ~-1.15 eV and -12.5 eV, and a broad peak with maximum at -5.5 eV. The decomposed UPS shows a main contribution from C 2p states and only below -14 eV the C 2s states are the main contribution; the H 1s contribution is negligible. Comparing this simulated spectrum with the corresponding C(110) passivated by atomic deuterium<sup>54</sup>, our simulated UPS shows a peak at -1.15 eV that is not observed in experiments. This peak comes from the surface atoms that present magnetization of +0.28 and +0.46, both with a contribution of the C 2p<sub>x</sub> and C 2p<sub>z</sub> states.

#### Simulated constant current mode STM images for the C(110)-(2×1)H+3H<sub>v</sub>-M1 surface

Figure 4.18 displays the simulated constant current mode STM images and linescans for C(110)-(2×1)H+3H<sub>v</sub>-M1 surface. The STM topography for  $V_{BIAS} = -0.49$  V (Fig. 4.18(a)) shows bright columns along y-direction centered at the subsurface C atoms located in between the topmost C atoms with H vacancies. The corresponding linescan along A-A' profile (Fig. 4.18(c)) reveals a corrugation of 1.25 Å. The STM topography for  $V_{BIAS} = +1.2$  V (Fig. 4.18(b)) presents an arrangement of x-elongated bright spots that are assigned to the bonding between the topmost C (with H vacancies) and subsurface C atoms along the y-direction; the x-elongated dark spots are assigned to the C-H sites. The corresponding linescan along the A-A' profile (Fig. 4.18(d)) shows a corrugation of ~0.4 Å. Finally, the STM topography for  $V_{BIAS} = +2.04$

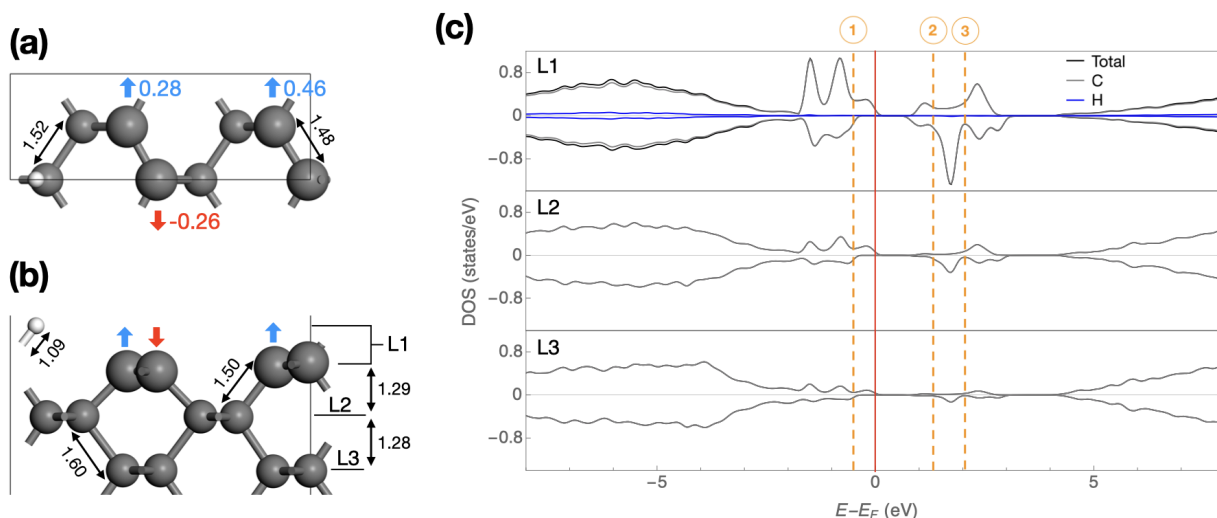


Figure 4.16: SCAN+rVV10 computed atomic and electronic structure of C(110)-(2 $\times$ 1)H+3H<sub>v</sub>-M1. (a) top and (b) side view of the three first topmost layers; the C (H) atoms are represented by grey (white) spheres and the surface C atoms are depicted by bigger spheres to contrast with the subsurface C atoms; the blue and red arrows shows the magnetization in  $\mu_B$  on the surface C atoms. (c) SP-PDOS of the three surface layers, the surface has insulator character; the spin up (down) are plotted with positive (negative) values on the DOS axis. The Fermi level  $E_F$  is shifted to 0 eV and is represented by the vertical red line. The ranges of integrated energies to obtain the STM images (a, b and e) are represented from Fermi level to the dashed orange lines (1, 2 and 3).

V (Fig. 4.18(e)) exhibits bright columns along  $y$ -direction identified as the bonding between the topmost and subsurface C atoms; the secondary bright columns are identified by subsurface C sites next to the C-H sites along the  $x$  direction and the dark columns are located at the surface C atoms lying equidistant between two C-H sites along the  $x$ -direction. The corresponding linescan along A-A' profile (Fig. 4.18(f)) reveals a maximum corrugation of 1.2 Å.

#### 4.2.7 The C(110)-(2 $\times$ 1)H+3H<sub>v</sub>-M2 surface

##### Atomic and electronic structure

We found a second magnetic solution for this surface that is 2.96 meV/Å<sup>2</sup> higher in energy with respect to the M1 solution. Figure 4.19 displays the computed results of the atomic and electronic structure of the

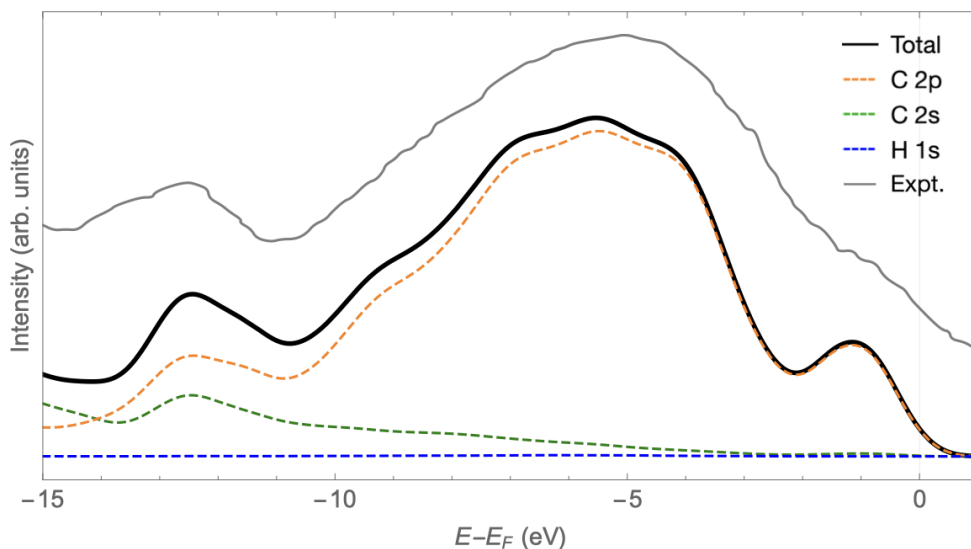


Figure 4.17: Simulated UPS spectrum for the C(110)-(2 $\times$ 1)H+3H<sub>v</sub>-M1 surface using 40.82 eV photons. The experimental spectrum for C(110) passivated by atomic deuterium obtained with the same photons energy (gray line) was adapted from Ref. 54 and displayed for direct comparison.

C(110)-(2 $\times$ 1)H+3H<sub>v</sub>-M2 surface. Figure 4.19(a) and (b) show the atomic reconstruction at the surface; after full relaxation, the atomic configuration is practically the same as the M1 case (cf. Figs. 4.16 and 4.19). In this magnetic solution the surface C atoms present a magnetization of  $-0.23$ ,  $+0.25$  and  $+0.47 \mu_B$ ; in comparison with the C(110)-(2 $\times$ 1)H+3H<sub>v</sub>-M1 surface, two C atoms changed its magnetic orientation. Figure 4.19(c) shows the computed SP-PDOS for layers L1, L2 and L3 corresponding to Figure 4.19(b); the results shows a bandgap opening of 0.86 eV. Similar to the M1 case, the electronic structure of L1 around  $E_F$  is mainly composed of C 2p states.

#### Simulated ultraviolet photoelectron spectroscopy UPS of the C(110)-(2 $\times$ 1)H+3H<sub>v</sub>-M2 surface

Figure 4.20 displays the simulated UPS spectrum for C(110)-(2 $\times$ 1)H+3H<sub>v</sub>-M2 surface using 40.82 eV photons. The spectrum shows main peaks at  $\sim -1.13$  eV and  $-12.5$  eV, and a broad peak with maximum at  $-5.5$  eV. The decomposed UPS shows a main contribution from C 2p states and only below  $-14$  eV the C 2s states are the main contribution; the H 1s contribution is negligible. Comparing the simulated UPS of C(110)-(2 $\times$ 1)H+3H<sub>v</sub>-M1 and this -M2, both spectra show almost no differences and both shows peaks close to  $-1$  eV that are not observed in the corresponding experimental UPS of C(110) passivated by

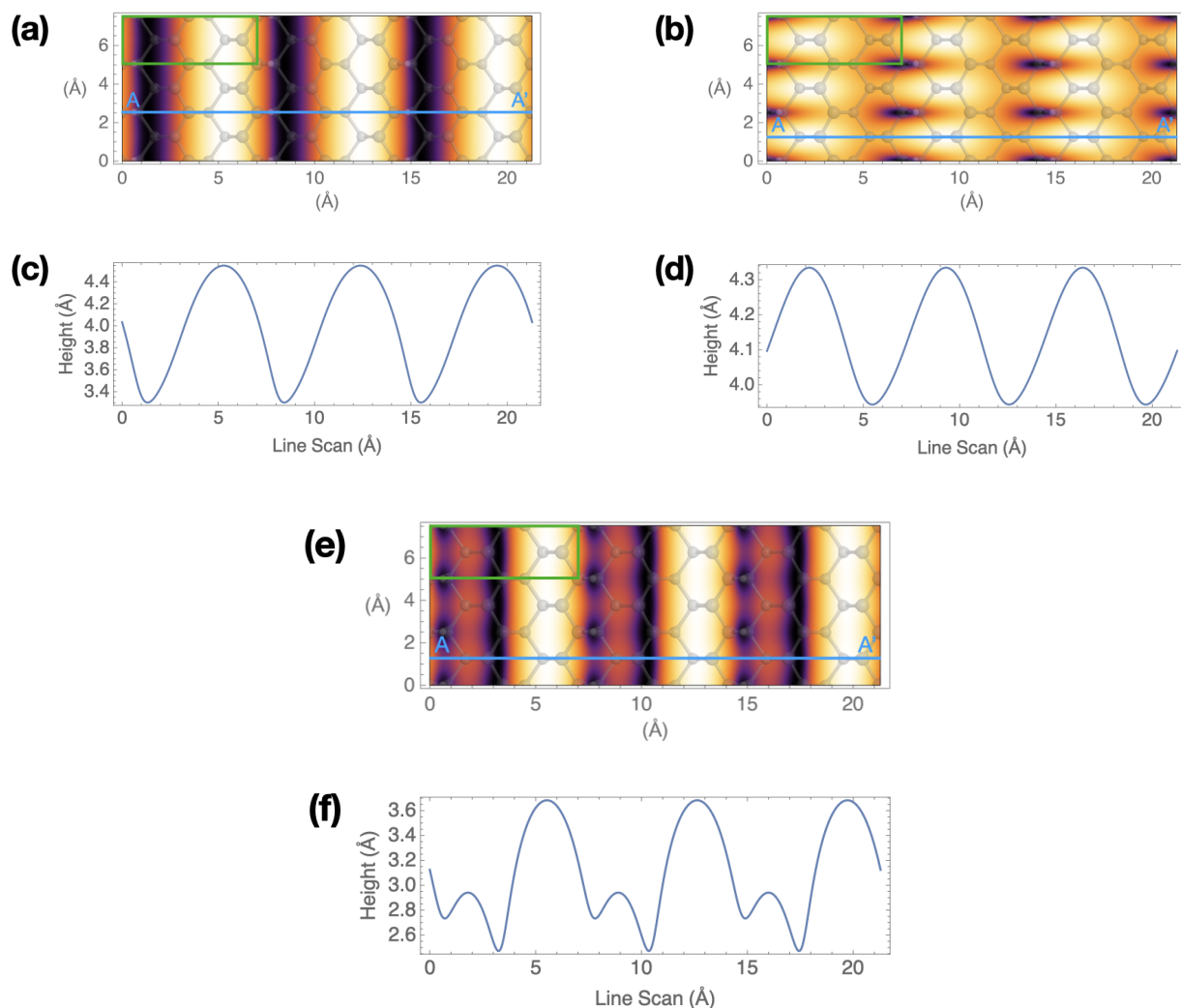


Figure 4.18: Computed constant current mode STM image and linescan along the A-A' profile for the C(110)-(2 $\times$ 1)H+3H<sub>v</sub>-M1 surface with  $V_{\text{BIAS}}$  of (a, c) -0.49 V, occupied states and (b, d) +1.2 V, (e, f) +2.04 V, unoccupied states. The STM images are colored such that bright (dark) colors of the isocurrent topology represent the protruding (receding) parts of the topology. In the three images is superimposed the atomic structure of the topmost layers where the C (H) atoms are represented by grey (white) spheres and the surface C atoms are depicted by bigger spheres; the green box delimits the surface unit cell.

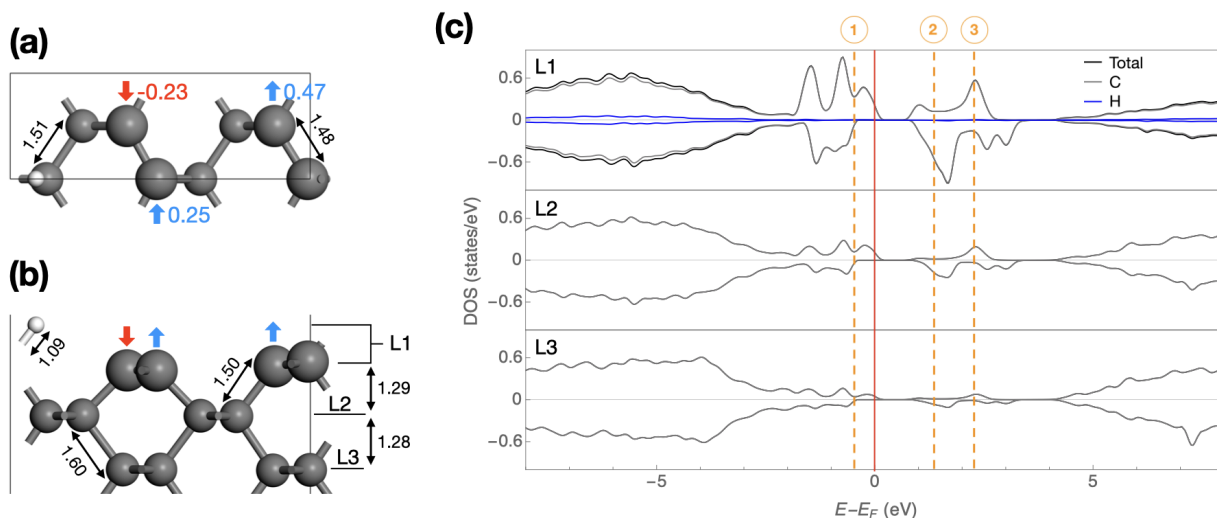


Figure 4.19: SCAN+rVV10 computed atomic and electronic structure of C(110)-(2 $\times$ 1)H+3H<sub>v</sub>-M2. (a) top and (b) side view of the three first topmost layers; the C (H) atoms are represented by grey (white) spheres and the surface C atoms are depicted by bigger spheres to contrast with the subsurface C atoms; the blue and red arrows shows the magnetization in  $\mu_B$  on the surface C atoms. (c) SP-PDOS of the three surface layers, the surface has insulator character; the spin up (down) are plotted with positive (negative) values on the DOS axis. The Fermi level  $E_F$  is shifted to 0 eV and is represented by the vertical red line. The ranges of integrated energies to obtain the STM images (a, b and e) are represented from Fermi level to the dashed orange lines (1, 2 and 3).

atomic deuterium<sup>54</sup>. The peak observed at -1 eV, in this case, comes from the surface atoms that present magnetization of -0.23 and +0.47, both with a contribution of the C 2p<sub>x</sub> and C 2p<sub>z</sub> states.

### Simulated constant current mode STM images of the C(110)-(2 $\times$ 1)H+3H<sub>v</sub>-M2 surface

Figure 4.21 displays the simulated constant current mode STM images and linescans for C(110)-(2 $\times$ 1)H+3H<sub>v</sub>-M2 surface. The STM topography for  $V_{BIAS} = -0.48$  V (Fig. 4.21(a)) shows bright columns along y-direction identified as the bonding between the topmost and subsurface C atoms. the darkest column is assigned to the surface magnetic C atoms located in between two C-H sites along the x-direction. The corresponding linescan along A-A' profile (Fig. 4.21(c)) reveals a maximum corrugation of 1.4 Å. The STM topography for  $V_{BIAS} = +1.31$  V (Fig. 4.21(b)) presents bright columns along y-direction identified as the subsurface C atoms located in between the magnetic surface C atoms in the x-direction; the darker



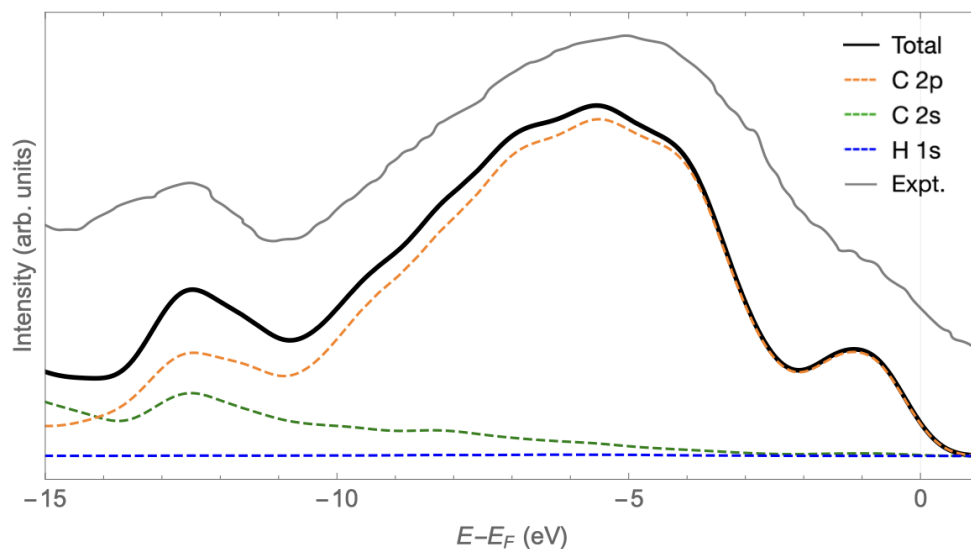


Figure 4.20: Simulated UPS spectrum for the C(110)-(2 $\times$ 1)H+3H<sub>v</sub>-M2 surface using 40.82 eV photons. The experimental spectrum obtained with the same photons energy (gray line) was adapted from Ref. 54 and displayed for direct comparison.

columns are assigned to the C-H sites along the  $y$ -direction. The corresponding linescan along A-A' profile (Fig. 4.21(d)) shows a corrugation of 1.6 Å. Finally, the STM topography for  $V_{\text{BIAS}} = +2.25$  V (Fig. 4.21(e)) exhibits bright columns that are assigned to the subsurface C atoms in alternating sites along the  $y$ -direction; the darkest columns are assigned to the magnetic surface C atoms with alternating magnetization along the  $y$ -direction. The corresponding linescan along A-A' profile (Fig. 4.21(f)) reveals a maximum corrugation of 2.5 Å.

### 4.3 The C(111) diamond surfaces

#### 4.3.1 The C(111) surface energies and electronic properties

In the C(111) surface calculations, we explored different surface structure reconstructions. In general, the surfaces explored were the pristine and hydrogenated surfaces for different cell sizes. The pristine surface structure C(111)-(1 $\times$ 1) presents a variation in its structure with respect to the reconstruction C(111)-(2 $\times$ 1), then we use both pristine structures as reference to explore the hydrogenated surface structures and reconstructions.

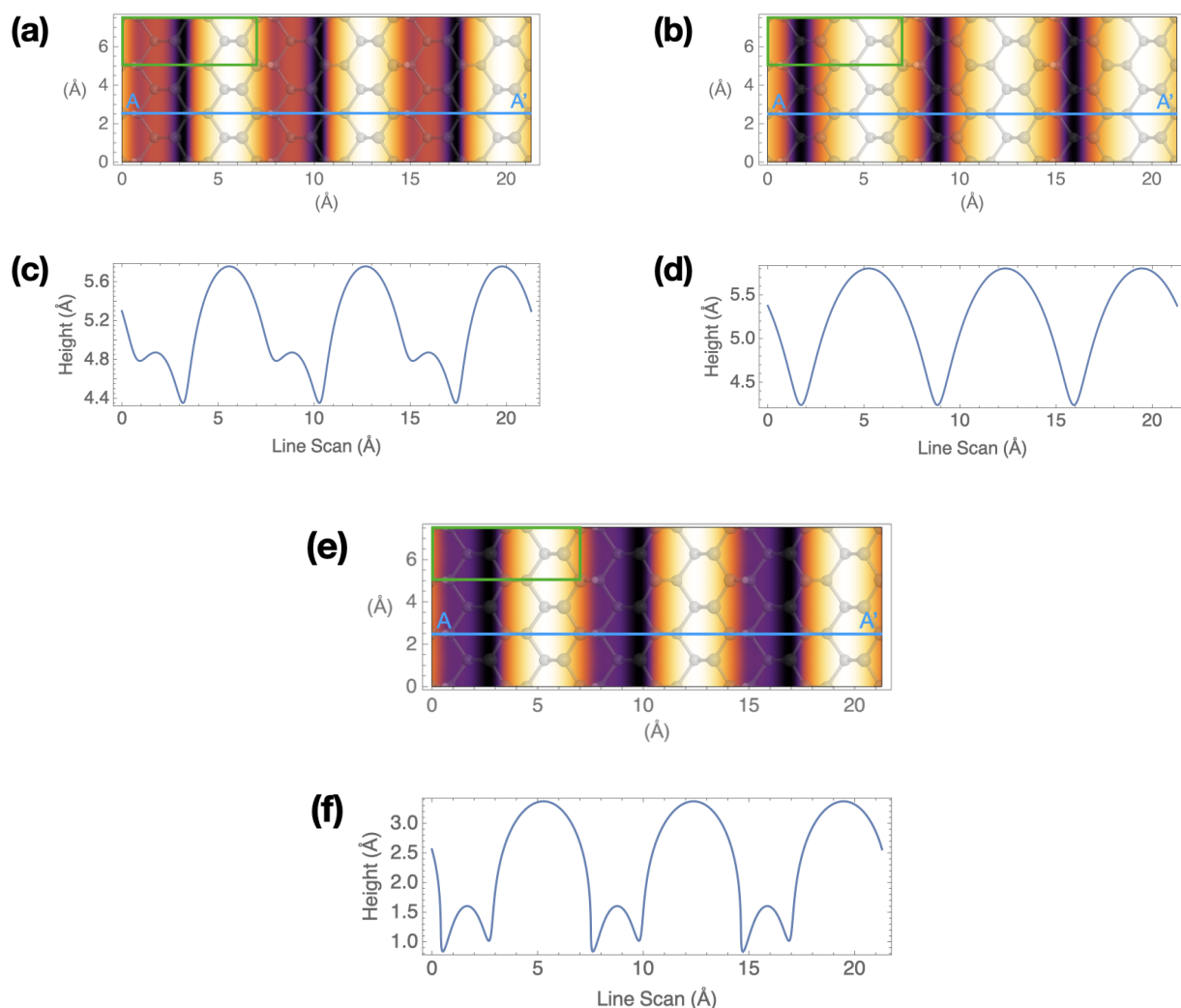


Figure 4.21: Computed constant current mode STM image and linescan along the A-A' profile for the C(110)-(2 $\times$ 1)H+3H<sub>v</sub>-M2 surface with  $V_{\text{BIAS}}$  of (a, c) -0.48 V, occupied states and (b, d) +1.31 V, (e, f) +2.25 V, unoccupied states. The STM images are colored such that bright (dark) colors of the isocurrent topology represent the protruding (receding) parts of the topology. In the three images is superimposed the atomic structure of the topmost layers where the C (H) atoms are represented by grey (white) spheres and the surface C atoms are depicted by bigger spheres; the green box delimits the surface unit cell.

Figure 4.22 displays the SCAN+rVV10 computed surface energies  $\gamma$  (cf. Eqs. 3.4 and 3.8) for all the reconstructions and hydrogenated surfaces considered in this study.

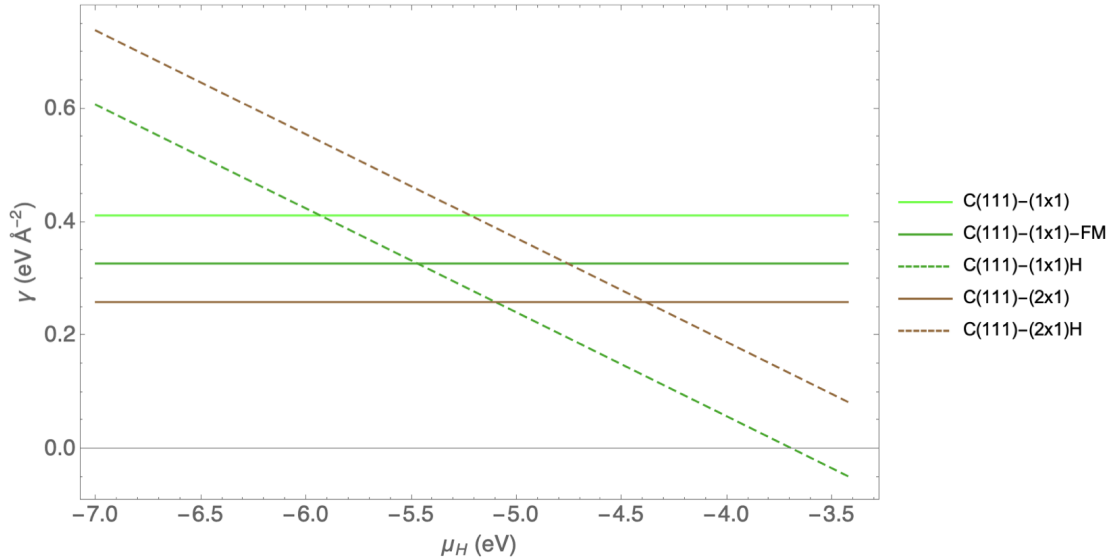


Figure 4.22: SCAN+rVV10 computed surface energy of the C(111) surfaces considered in this study. The different colors (green and brown) denote the number of cell repetitions ( $1\times 1$  and  $2\times 1$ ) in the  $x$ - and  $y$ -direction. The structures that only have carbon atoms on the surface are represented by solid energy lines; while the dashed lines represent the surfaces with carbon and hydrogen atoms. In the inset, FM stands for ferromagnetic solution.

The most expected surface for  $\mu_H < -5.1$  eV is the pristine C(111)-( $2\times 1$ ) while for  $\mu_H > -5.1$  eV is the fully hydrogenated surface C(111)-( $1\times 1$ )H, both without magnetization; however, we observed the most stable pristine surface for C(111)-( $1\times 1$ ) reconstructions is ferromagnetic. Based in these results, the following sections will analyse in detail the electronic structure of C(111)-( $2\times 1$ ) and C(111)-( $1\times 1$ )H surfaces. Table 4.3 shows a summary of the work functions and energy bandgaps calculated in this study for the (111) family of surfaces; notice the increased gap and decreased work function for the hydrogenated surface.

Table 4.3: SCAN+rVV10 computed work functions ( $\Phi$ ) and energy bandgaps ( $E_g$ ) for the C(111) surfaces considered in this study. Additionally keep in mind that computed here (experimental)  $E_g$  for bulk diamond is 4.5 (5.4) eV.

Surface	$\Phi$ (eV)	$E_g$ (eV)
C(111)-(2 $\times$ 1)	5.58	1.61
C(111)-(1 $\times$ 1)H	3.67	3.14

### 4.3.2 The C(111)-(2 $\times$ 1) surface

#### Atomic and electronic structure

Figure 4.23 displays the computed results of the atomic and electronic structure of the C(111)-(2 $\times$ 1) surface. Figure 4.23(a) and (b) show a reconstruction similar to the chain-like atomic reconstruction proposed by Pandey<sup>55</sup> and ordered by bilayers at different heights. After relaxation, the structure presents tilted chains with intrachain buckling from second to bulk bilayers. There is a dimerization at the bilayer L1 forming ‘zig-zag’ chains of C atoms with a C-C distance of 1.43 Å and a bond angle of 122.4°. The surface geometry is very close to that of graphite, allowing the formation of a delocalised  $\pi$  bond, which stabilises the surface. Notice the alternation of five-atom and seven-atom rings at the first bilayers, contrary to the diamond bulk structure and the (110) surface reconstructions (Sec. 4.3). Figure 4.23(c) shows the computed PDOS for bilayers L1, L2 and L3 corresponding to Figure 4.23(b); the results exhibit an insulator state with  $E_g = 1.61$  eV. The electronic structure of L1 around  $E_F$  is mainly composed of C 2p states with minor contributions of C 2s.

#### Simulated ultraviolet photoelectron spectroscopy UPS for the C(111)-(2 $\times$ 1) surface

Figure 4.24 displays the simulated UPS spectrum for C(111)-(2 $\times$ 1) surface using 40.82 eV photons which correspond to photoelectrons generated within approximately 5.74 Å of the outermost surface layers—i.e., the 3 outermost atomic bilayers. The spectrum shows a broad peak centered around  $\sim$ -5 eV, a shoulder at -1.5 eV and other peak at -12 eV. The decomposed UPS suggest it has mainly a C 2p character and below -13.5 eV C 2s states start to be the main contribution. The simulated UPS nicely reproduces the main features of the corresponding experimental UPS spectrum by Francz *et al.*<sup>54</sup> obtained from a natural diamond (111) with 40.82 eV photons after annealing at 1050 °C, as depicted in the same Figure 4.24.

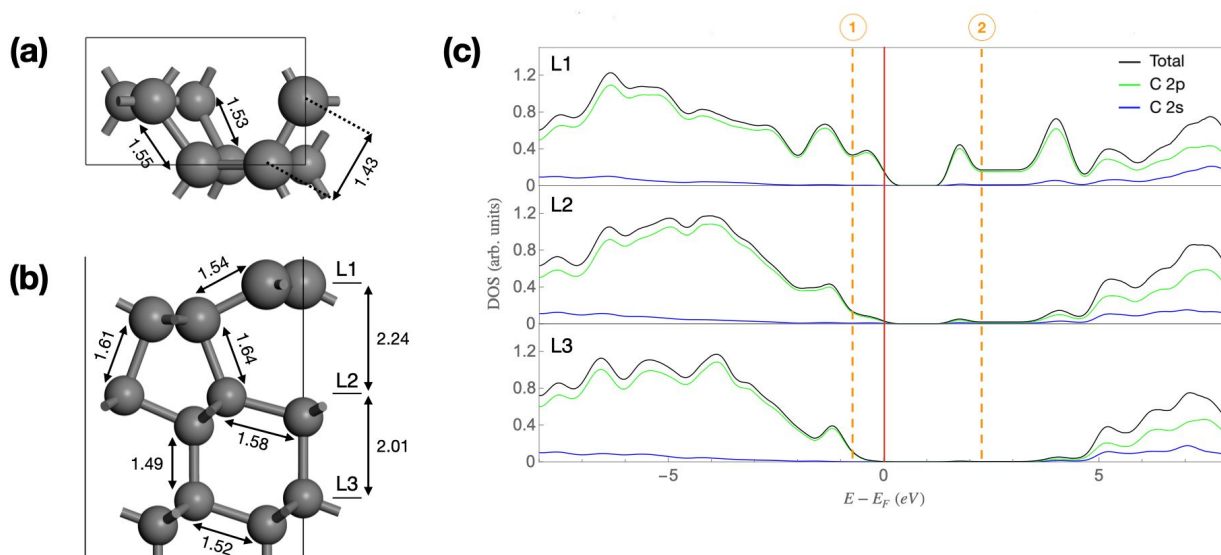


Figure 4.23: SCAN+rVV10 computed atomic and electronic structure of C(111)-(2 $\times$ 1). (a) top and (b) side view of the three first topmost bilayers; the C atoms are represented by grey spheres and the surface C atoms are depicted by bigger spheres to contrast with the subsurface C atoms; the black lines delimits the surface unit cell. (c) PDOS of the three surface layers, the surface has insulator character. The Fermi level is shifted to 0 eV and is represented by the vertical red line. The ranges of integrated energies to obtain the STM images (a and b) are represented from Fermi level to the dashed orange lines (1 and 2).

### Simulated constant current mode STM images for the C(111)-(2 $\times$ 1) surface

Figure 4.25 displays the simulated constant current mode STM images and linescans for C(111)-(2 $\times$ 1) surface. The STM topography for  $V_{\text{BIAS}} = -0.76$  V (Fig. 4.25(a)) shows bright (dark) columns that are assigned to the topmost (subsurface) C atoms of same surface bilayer L1 along the  $y$ -direction. The corresponding linescan along the A-A' profile (Fig. 4.25(c)) shows a corrugation of  $\sim 0.24$  Å. The STM topography for  $V_{\text{BIAS}} = +2.3$  V (Fig. 4.25(b)), the zig-zag bright columns along  $y$ -direction are identified as surface and subsurface C sites; the dark spots are located where either no surface nor subsurface C atoms are present. The corresponding linescan along A-A' profile (Fig. 4.25(d)) reveals a corrugation of 0.56 Å.

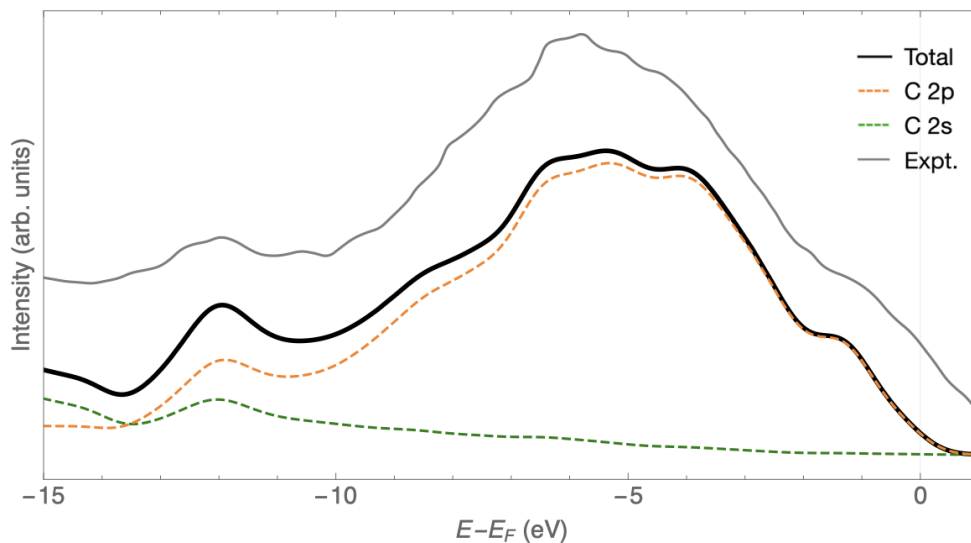


Figure 4.24: Simulated UPS spectrum for the C(111)-(2 $\times$ 1) surface using 40.82 eV photons. The experimental spectrum obtained with the same photons energy (gray line) was adapted from Ref. 54 and displayed for direct comparison.

### 4.3.3 The C(111)-(1 $\times$ 1)H surface

#### Atomic and electronic structure

Figure 4.26 displays the computed results of the atomic and electronic structure of the fully H covered C(111)-(1 $\times$ 1)H surface. Figure 4.26(a) and (b) show the atomic reconstruction at the surface; after full relaxation we notice the inward relaxation of the topmost L1 layer and the H atoms are vertically adsorbed on the surface C atoms with a bond length of 1.10 Å. Figure 4.26(c) shows the computed DOS for layers L1, L2 and L3 corresponding to Figure 4.26(b); the system shows an insulating state with  $E_g = 3.14$  eV. The electronic structure at  $E_F$  is mainly composed of C 2p states with minor contributions of C 2s and H 1s states.

#### Simulated ultraviolet photoelectron spectroscopy UPS of the C(111)-(1 $\times$ 1)H surface

Figure 4.27 displays the simulated UPS spectrum for C(111)-(1 $\times$ 1)H surface using 40.82 eV photons. The spectrum shows a broad peak centered at  $\sim -4.4$  eV and other peak at -11.8 eV. The decomposed UPS shows a C 2p main contribution and below -13.5 eV the C 2s states start to be the main character; the H

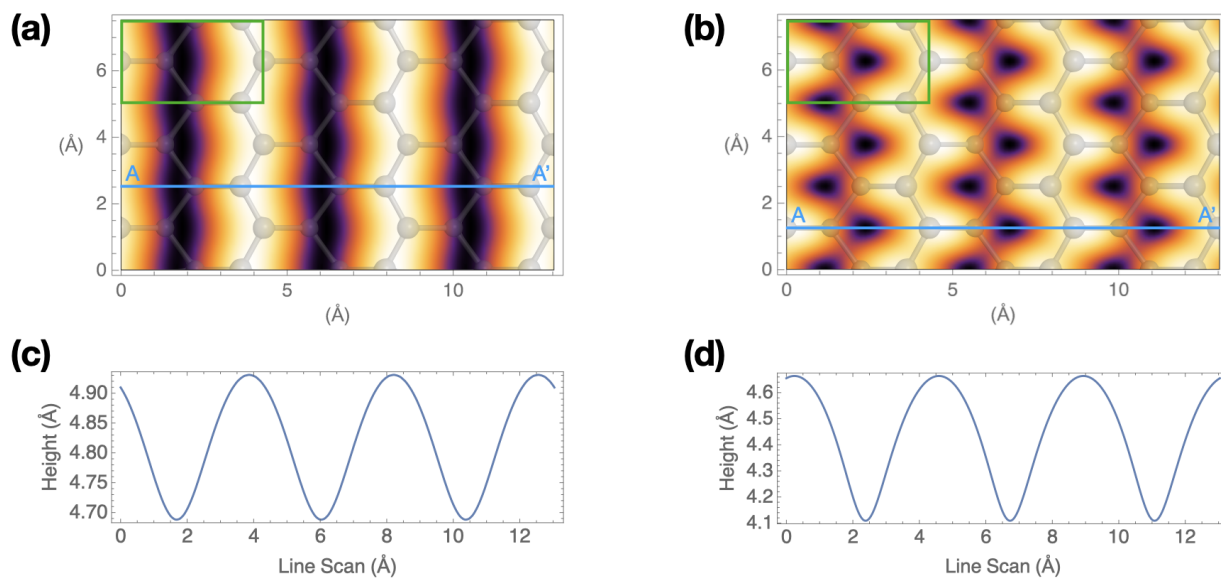


Figure 4.25: Computed constant current mode STM image and linescan along the A-A' profile for the C(111)-(2 $\times$ 1) surface with  $V_{\text{BIAS}}$  of (a, c) -0.76 V, occupied states and (b, d) +2.3 V, unoccupied states. The STM images are colored such that bright (dark) colors of the isocurrent topology represent the protruding (receding) parts of the topology. In both images is superimposed the atomic structure of the topmost bilayer where the C atoms are represented by grey spheres and the surface C atoms are depicted by bigger spheres; the green box delimits the surface unit cell.

1s states contribution is practically negligible. A direct comparison with the corresponding experimental UPS obtained from a natural diamond (111) with 40.82 eV photons after atomic deuterium exposure<sup>54</sup> shows close similarities.

### Simulated constant current mode STM images of the C(111)-(1 $\times$ 1)H surface

Figure 4.28 displays the simulated constant current mode STM image and linescan for C(111)-(1 $\times$ 1)H surface. The STM topography for  $V_{\text{BIAS}} = -1.26$  V and  $V_{\text{BIAS}} = +3.6$  V (Fig. 4.28(a, b)) shows a hexagonal arrangement of bright spots that are assigned to the topmost C-H sites; the dark spots are assigned to subsurface C sites. The corresponding linescans along the A-A' profile (Fig. 4.28(c, d)) shows maximum corrugations of  $\sim 0.006$  Å and  $\sim 0.011$  Å, respectively.

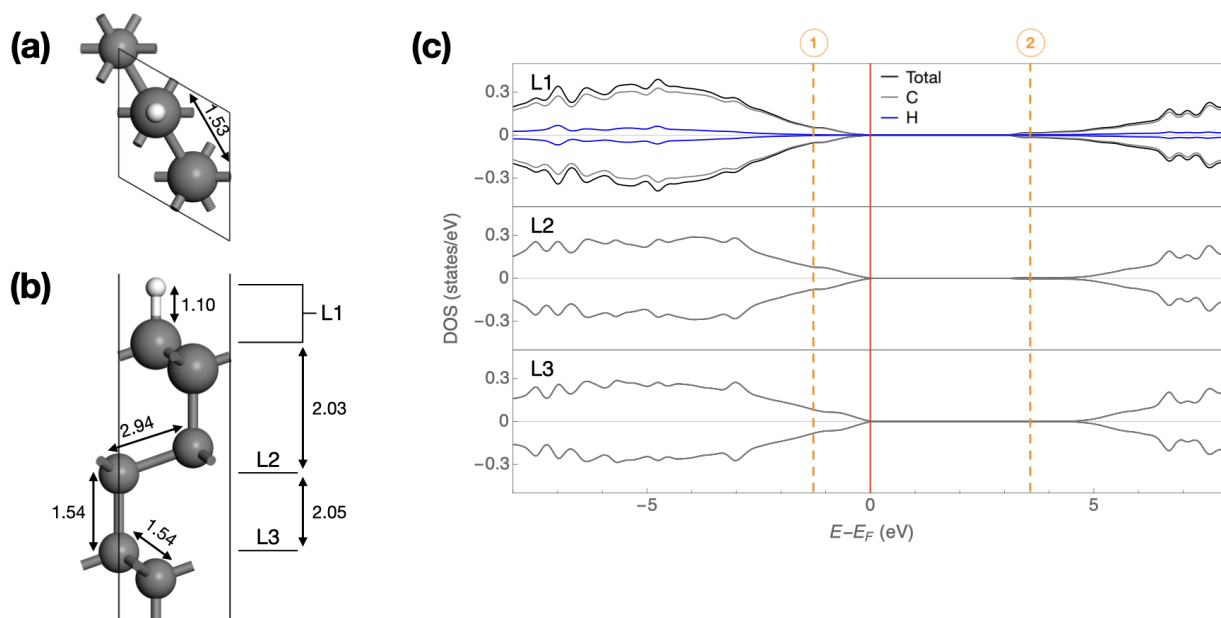


Figure 4.26: SCAN+rVV10 computed atomic and electronic structure of C(111)-(1 $\times$ 1)H. (a) top and (b) side view of the three first topmost layers; the C (H) atoms are represented by grey (white) spheres and the surface C atoms are depicted by bigger spheres to contrast with the subsurface C atoms; the black lines delimits the surface unit cell. (c) DOS of the three surface layers, the surface has insulator character. The Fermi level is shifted to 0 eV and is represented by the vertical red line. The ranges of integrated energies to obtain the STM images (a and b) are represented from Fermi level to the dashed orange lines (1 and 2).



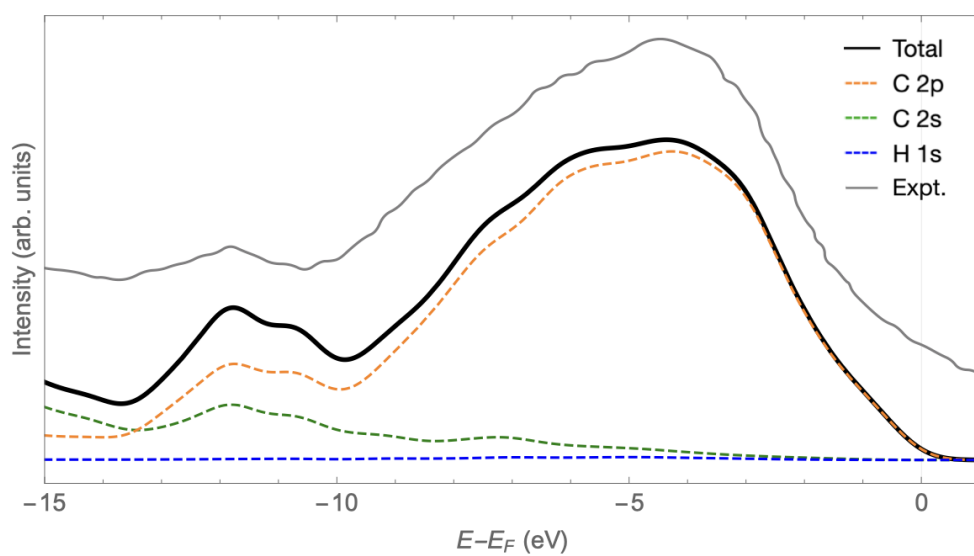


Figure 4.27: Simulated UPS spectrum for the C(111)-(1 $\times$ 1)H surface using 40.82 eV photons. The experimental spectrum obtained with the same photons energy (gray line) was adapted from Ref. 54 and displayed for direct comparison.

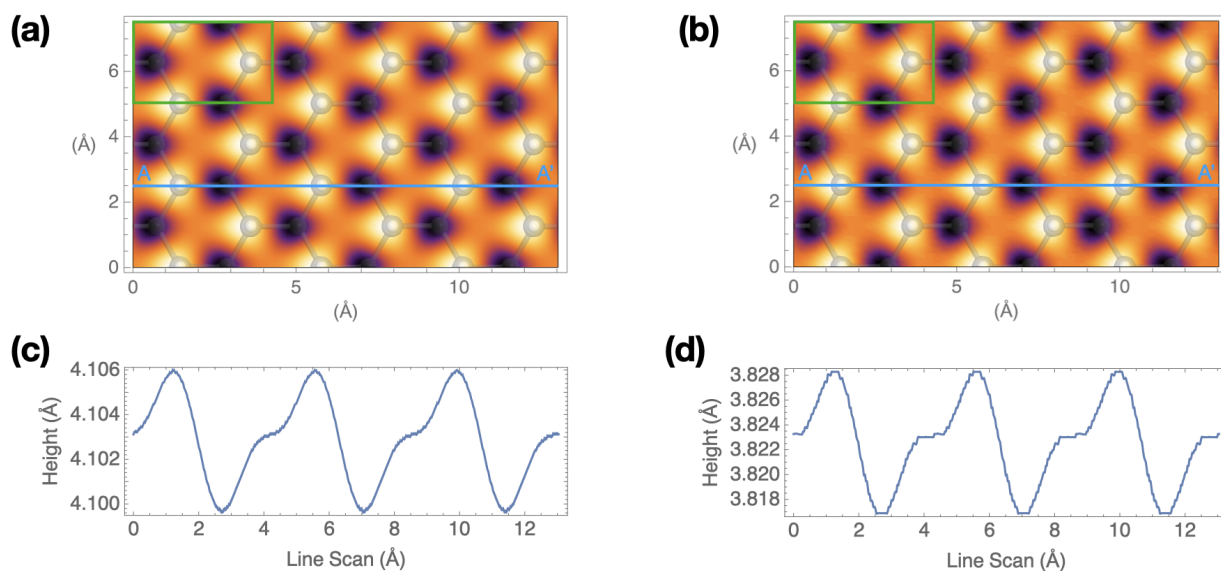


Figure 4.28: Computed constant current mode STM image and linescan along the A-A' profile for the C(111)-(1×1)H surface with  $V_{\text{BIAS}}$  of (a, c) -1.26 V, occupied states and (b, d) +3.6 V, unoccupied states. The STM image is colored such that bright (dark) colors of the isocurrent topology represent the protruding (receding) parts of the topology. In the image is superimposed the atomic structure of the topmost layers where the C atoms are represented by grey spheres and the surface C atoms are depicted by bigger spheres; the green box delimits the surface unit cell.

## Chapter 5

# Conclusions & Outlook

In this thesis, we have performed a detailed DFT study of the atomic and electronic structure of diamond surface reconstructions with hydrogenation and carbon vacancies defects using a state-of-the-art functional SCAN+rVV10.

In the first stage, we studied the electronic and mechanical properties of pristine bulk fcc diamond crystal, finding semi-quantitative and qualitative agreement for the experimental data. The simulated bulk structure was the starting point for designing an appropriate methodology for the study of pristine, hydrogenated, and carbon vacancy diamond surfaces. Here, we were able to define the optimal vacuum space in a diamond slab cell, the slab thickness needed to reproduce a surface, the energies of a passivated surface, and the different modifications for the diamond surface structures.

We proposed and simulated in total fourteen different C(110) surface models. Based on the computed surface energy, we were able to identify the most energetically favorable surface reconstructions; finding a particular region of H chemical potentials ( $-5.8 < \mu_H < -5.0$  eV) where we find a variety of possible hydrogenated reconstructions from which some of them show magnetic properties. We performed UPS simulations for the most stable surface structures, the computed spectra show that the C(110)-(1×1) surface reproduces qualitatively and semi-quantitatively the experimental UPS reported for the pristine surface. Whereas the surface that best reproduces the experimental UPS reported for a hydrogenated diamond surface is the metallic C(110)-(2×1)H+2H<sub>v</sub> surface, even though the insulator C(110)-(2×1)H+2H<sub>v</sub>-AFM surface is energetically most stable and presents practically the same atomic geometry. We presume that temperature effects might lead to a transition from the predicted AFM (insulator) to the non-magnetic

(metallic) state—bear in mind that all our simulations are at zero Kelvin—therefore, due to temperature effects, the experiments are reporting only the non-magnetic phase. Computing the constant current mode STM images for the most stable surface structures, we found different STM images between the C(110)-(2×1)H+2H<sub>v</sub> and C(110)-(2×1)H+2H<sub>v</sub>-AFM surfaces; suggesting that the STM images clearly can resolve the state of the surfaces, AFM or non-magnetic in this case. Based on the previous results, we suggest that with experimental STM images for unoccupied states taken at low temperatures, i.e., liquid helium temperatures, one could determine which surfaces are being seen in the experiment. Furthermore, using scanning tunneling spectroscopy (STS), we can directly measure the existence of a bandgap and determine which surface is present in the experiment.

Additionally, considering both C(110)-(2×1)H+3H<sub>v</sub>-M1 and C(110)-(2×1)H+3H<sub>v</sub>-M2 surfaces, they present practically similar energies and simulated UPS spectra; these results that do not make possible the differentiation between both surfaces. However, the STM images present clear differences between the M1 and M2 states, making the atomic structure resolution possible for this kind of surfaces.

Concerning the C(111) surface structures, we considered five surface models. The outcome of the computed surface energies allow us to identify the most favorable surface reconstructions. We found that the most stable surfaces are the C(111)-(2×1) and C(111)-(1×1)H surfaces. The UPS spectra for both surfaces are reproduced in excellent agreement with respect to the experimental spectra. The STM images for both surface structures are completely different between them. In the case of the STM images for the occupied and unoccupied states for the C(111)-(2×1) surface, presents different STM images; while, for the C(111)-(1×1)H surface, the STM images are basically similar.

Furthermore, it is essential to note that all the simulated STM images, except for surfaces C(110)-(1×1)H and C(111)-(1×1)H, present images with a corrugation above 0.1 Å (See Fig. 4.9, 4.28). Which means that all the surfaces, except the above mentioned, we predict that an appropriate STM experiment might be able to revolve the atomic structure, this conclusion is supported considering that the best experimental STM can obtain images with a maximum resolution along *z*-direction of 0.1 Å<sup>56</sup>.

Finally, we are aware that other reconstructions might be possible and escape our models but we are confident that given the level of sophistication of the method used here, the results presented in this thesis could encourage further experiments, specially considering the prediction of magnetic phases in the case of C(110) surfaces.

# Appendix A

## VASP working principle

In order to understand how VASP performs the DFT calculations for a given system, we need to understand the different input and output files involved in the procedure. So, the following sub-sections detail the files and their content.

### A.0.1 VASP inputs

The input files give a complete description of all the parameters and what calculation procedures the software should perform. In general, the minimum amount of input files are four: INCAR, POTCAR, POSCAR, and KPOINTS.

1. **INCAR:** This is the most critical file because it determines which calculations do and how to perform them. Usually, this is the primary source of errors that can produce false results, so we need to pay close attention to this particular file. This file has a large set of parameters that can be set through tags (always in capital letter) in each file line. Most tags have default values if they are not specified<sup>57</sup>. See Figure C.1 for an example, and for more information about the possible tags, please visit the VASP documentation on the following website: <https://www.vasp.at/wiki/index.php/Category:INCAR>.
2. **POTCAR:** The POTCAR file contains the pseudopotentials and specific information (such as core radius, number of valence electrons, atomic mass, and atomic configuration) about each atomic species we are working to perform the calculations. If there are more than one atomic species in the calculation, we should create just one POTCAR file with all the concatenated POTCAR files in the same atomic order as in the POSCAR and INCAR files are specified. It is also essential to mention

that with the POTCAR file present in the input files, it is not necessary to specify the valence and mass in the INCAR file<sup>58</sup>.

3. **POSCAR:** This file contains the atomic structure of the system. The lattice constant, lattice vectors, and ionic positions are the mainly used parameters to describe the structure<sup>59</sup>. See Figure C.2 for an example.
4. **KPOINTS:** This file specifies the Bloch vectors ( $k$ -points) used to sample the Brillouin zone in the calculation. The most convenient way to specify the  $k$ -points sampling is that VASP automatically generates a regular mesh of points. The  $k$ -points generation mode that we use is the Monkhorst-Pack, which is the flavor most commonly used to grid generation. This mode allows the user to supply the subdivisions  $N_1$ ,  $N_2$ , and  $N_3$  manually<sup>60</sup>. See Figure C.3 for an example.

## A.0.2 VASP outputs

After performing the calculations with VASP, it will generate some output files with the results and input parameters summaries. The number of output files depends on the achieved procedures according to the input files. The most relevant files that commonly generate in most calculations are: CONTCAR, CHGCAR, CHG, DOSCAR, OUTCAR, OSZICAR, and WAVECAR.

1. **CONTCAR:** This file contains the new atomic structure of the system after VASP calculations (such as relaxations). The CONTCAR file is written in the same format as POSCAR, with the difference that it is modified after each ionic step. If VASP stops or kills the calculations for some reason, it should be possible to retake them from the CONTCAR file<sup>61</sup>.
2. **CHGCAR and CHG:** These files contain the lattice vectors, atomic coordinates, total charge density multiplied by the volume, and a data array with the electron number density in all the cell. They can be used to restart VASP from an existing charge density<sup>62,63</sup>.
3. **DOSCAR:** This file contains information about the total density of state (DOS), integrated DOS, the partial density of state (PDOS), and Fermi energy level<sup>64</sup>. See Figure C.4 for an example.
4. **OUTCAR:** This file contains information about stress tensors, forces on the atoms, local charges, magnetic moments, dielectric properties, information about the electronic steps, and a summary of the used input parameters<sup>65</sup>.

5. **OSZICAR:** This file gives information about convergence speed and the current step. Most specifically, it gives information such as the number of electronic steps, current free energy values, total energy after obtaining convergence, change in the free band structure, and energy values. All of these in real-time while the calculations are performing<sup>66</sup>.
6. **WAVECAR:** This is a binary file that contains data about the number of bands, cut-off energy, basis vectors defining the supercell, eigenvalues, Fermi-weights, and wavefunctions. This file provides starting wavefunctions for a continuation job<sup>67</sup>.





## Appendix B

# bSKAN working principle

In order to understand how bSKAN simulates the STM images for a given system, we need to understand the different inputs and outputs files involved in the procedure. So, the following sub-sections detail the files and the kind of content of each one of them. It is necessary to mention that, in the same way as VASP, all input and output files are written in capital letters, where the first two or three letters specify the information that it contains. Some examples are: all files related to the Kohn-Sham states begin with WAV-, files describing the geometry with A-, input parameters are contained in files named IN-, the output in files OUT-. Current maps are stored in CUR- files, while plots generally are called PLOT or PLT<sup>46</sup>.

### B.0.1 bSKAN inputs

The bSKAN input files give a complete description of all the parameters and the program's calculation procedures to realize. In this way, we use four essential input files always present in any calculation. They are INCAR, INSCAN, WAVSAMPLE, and ASAMPLE. Considering that bSKAN can cooperate with VASP, we can use VASP to calculate the Kohn-Sham states and use them to perform the bSKAN calculation, as we will see in the following descriptions<sup>46</sup>.

1. **INCAR:** This file has the same form and purposes as in VASP calculations, just with the difference of an additional line that describes some STM information needed. Information such as the range of energy values of interest according to the DOS, range of atomic positions in the z-direction, and the Fermi energy level.
2. **INSCAN:** This file contains all the input parameters needed for the simulation. It has similar form and purposes as the INCAR file. See Figure C.5 for an example and visit the following reference<sup>46</sup>

for tags documentation.

3. **WAVSAMPLE:** This file contains the Kohn-Sham states of the surface and can be created using the OUTCAR file resulting from VASP calculations.
4. **ASAMPLE:** This file contains the atomic position of surface atoms and can be created using the CONTCAR file resulting from VASP calculations. Also, the file has the same structural form as CONTCAR file.

### **B.0.2 bSKAN outputs**

Output files are either for information on the run. It contains the simulation data or an extracted sample of the simulation data for visualizing. Commonly, there are four output file essentials in any calculation: OUTSCAN, CURMAT, and CURSAVE<sup>46</sup>. However, in our case, we also obtained an additional file called CURRENT.

1. **OUTSCAN:** This file contains all the output information of the STM simulations. It is similar to the OUTCAR file on VASP.
2. **CURMAT:** This is a binary file that contains the current matrix of a topographic simulation.
3. **CURSAVE:** This file contains the current spectrum or matrix in ASCII format.
4. **CURRENT:** This file contains a current array in OpenDX format. This file is used to build the STM image with its corrugated structure. This image is constructed with the help of Wolfram Mathematica software.

## Appendix C

# Input and output files examples

Examples of input and output files used in this work.

```
1 SYSTEM = Diamond
2 ##### ELECTRONIC #####
3 ISMEAR = -5
4 LREAL = auto
5 PREC = Accurate
6 ENCUT = 1000
7 ALGO = N
8 LORBIT = 11
9 AMIN = 0.01
10 ##### FUNCTIONAL #####
11 METAGGA = SCAN
12 LUSE_VDW = .TRUE.
13 BPARAM = 15.7
14 LMIXTAU = T
15 LASPH = .TRUE.
16 ##### DIPOLE CORRECTIONS #####
17 IDIPOL=3
18 LDIPOL=.TRUE.
```

Figure C.1: Example of a typical INCAR file. This text shows various tags used to describe the electronic relaxations, functional, and dipole corrections used to perform a VASP calculation. Also, it is necessary to mention that the symbols # or ! are used to set comments.

```

1 Hydrogenated Diamond Surface
2 1.0000000000000000
3 2.5095000000000001 0.0000000000000000 0.0000000000000000
4 -1.2547499999999994 2.1732907507970491 0.0000000000000000
5 0.0000000000000000 0.0000000000000000 28.336999999999997
6 C H
7 12 2
8 Selective dynamics
9 Direct
10 0.3333160593095900 0.6666839406904019 0.0572710929269463 T T T
11 0.9999876837654681 0.0000123162345344 0.1289305222226718 T T T
12 0.6666611535852203 0.3333388464147730 0.2012149232025754 T T T
13 0.3333372232367867 0.6666627767632129 0.2733859867420120 T T T
14 0.0000097478890398 0.9999902521109592 0.3456246052817470 T T T
15 0.6666805808529412 0.3333194191470510 0.4180480105683786 T T T
16 0.9999802752710698 0.0000197247289254 0.0744242348201843 T T T
17 0.6666552809525793 0.3333447190474138 0.1470025819060418 T T T
18 0.3333328575784064 0.6666671424215780 0.2192374109983557 T T T
19 0.0000070811729534 0.9999929188270432 0.2914575282609311 T T T
20 0.6666797288563177 0.3333202711436756 0.3636187770101301 T T T
21 0.3333460448829265 0.6666539551170733 0.4351640584656698 T T T
22 0.3333540273908592 0.6666459726091394 0.4741044039903367 T T T
23 0.3333132496650258 0.6666867503349664 0.0183425281914370 T T T

```

Figure C.2: Example for the POSCAR file. This text shows the lattice information of the C(111)-(1×1)H surface structure with 6 layers and 15 Å vacuum. The first line is treated as a comment, so here we can write the name of the system we are studying. The second is the scaling constant constant, which is used to scale the lattice vectors and all the atomic coordinates; If this value is negative, it becomes the volume of the cell. The third to the fifth lines specify the lattice vectors in Å. The sixth line defines the system elements; it should have the same species organization as the POTCAR file. The seventh line gives the number of atoms per atomic species (one number for each species). The eighth allows restriction on the movement of atoms (cf. the T at the end of lines 10 and below). The ninth line indicates if the atomic coordinates will be in direct (fractional) or cartesian coordinates. Finally, from the tenth to the last line, the atomic positions are provided according to the lattice geometry defined on ninth line<sup>59</sup>.

```

1 Diamond sf110-1x1 Dk=0.042 Ang^-1
2 Gamma
3 7 9 1
4 0 0 0

```

Figure C.3: Example for the KPOINTS file. This text shows the KPOINTS file used for the C(110)-(1×1) surface structure. The first line is treated as a comment, so we can label the system we are studying in this line. The second specifies the number of  $k$ -points, if 0 then the mesh will be generated automatically. The third line specifies a Monkhorst-Pack gamma-centered grid generation. The fourth line defines the  $N_1$ ,  $N_2$ , and  $N_3$  subdivisions along the reciprocal lattice vectors. Finally, the last line specifies the optional shift of the mesh<sup>60</sup>.

```

1 38 38 1 0
2 0.8856036E+01 0.3549000E-09 0.2509500E-09 0.3778590E-08 0.5000000E-15
3 1.0000000000000000E-004
4 CAR
5 Diamond
6 15.00000000 -5.00000000 4001 6.09157233 1.00000000
7 -5.000 0.5869E+01 0.5868E+02
8 -4.995 0.5818E+01 0.5871E+02
9 -4.990 0.5801E+01 0.5873E+02
10 -4.985 0.5784E+01 0.5876E+02
11 -4.980 0.5766E+01 0.5879E+02

```

Figure C.4: Example of a DOSCAR output file. From the first line hows four numbers corresponding to the number of ions (including empty spheres), number of ions, 0 (no PDOS) or 1 (for PDOS). The second line contains five numbers corresponding to the unit cell volume in  $\text{\AA}^3$ , length of the basis vectors (a,b,c), and the POTIM tag. The third line specifies the temperature value. The fourth line gives the name of the system as given by SYSTEM in the INCAR file. The sixth line gives five values corresponding to the energy range in which the DOS is given, the number of grid points on which the DOS is evaluated, Fermi energy level, and the value of 1. Finally, from the seventh to the last line is given a list of values that correspond to energy, DOS, and integrated DOS<sup>64</sup>.

```
1 #STM simulation for 111 diamond 2x1
2 TERSOFF
3 # NUMERICAL
4 LIMITS = -0.01 0.01
5 GRIDPOINTS = 150
6 BIAS VOLTAGE = 4.5
7 NKELDYSH = 1
8 PIVOT = 0.0000 0.0000
9 TOP = 0.0000 0.0000
10 ZVACUUM = 25.9575
11 CURRENT = 0.0
```

Figure C.5: Example for the INSCAN file. This text shows a typical INSCAN file used to simulate the STM images for the C(111)-(2×1) surface structure.

## Appendix D

# Computed work functions for all the selected surfaces

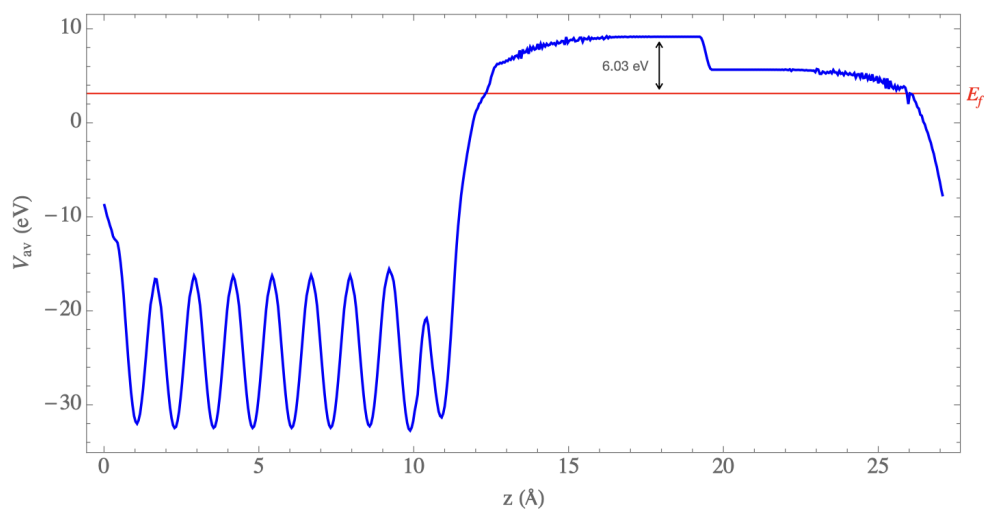


Figure D.1: SCAN+rVV10 computed work function for the C(110)-(1×1) surface. The average potential in  $z$ -direction is represented by the blue line; while the Fermi level  $E_F$  is represented by the horizontal red line.

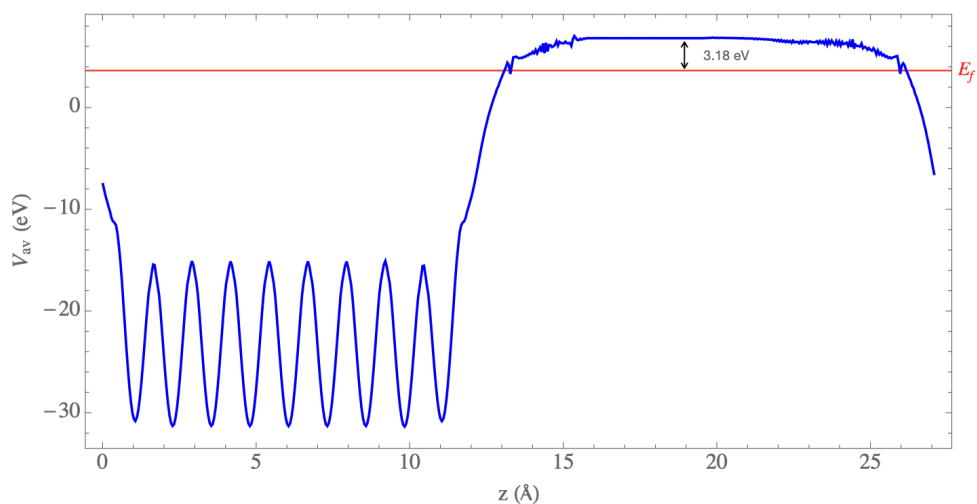


Figure D.2: SCAN+rVV10 computed work function for the C(110)-(1×1)H surface. The average potential in  $z$ -direction is represented by the blue line; while the Fermi level  $E_F$  is represented by the horizontal red line.

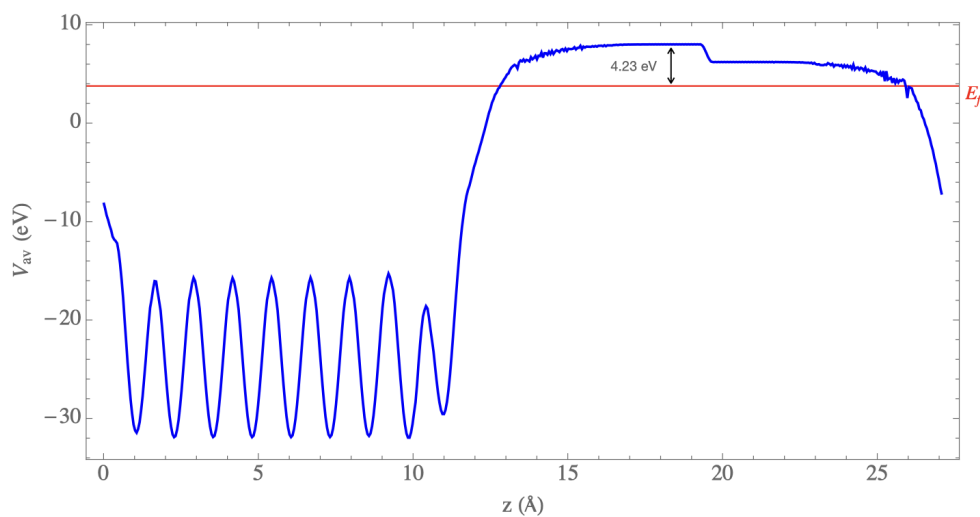


Figure D.3: SCAN+rVV10 computed work function for the C(110)-(1×1)H+2H<sub>v</sub> surface. The average potential in  $z$ -direction is represented by the blue line; while the Fermi level  $E_F$  is represented by the horizontal red line.



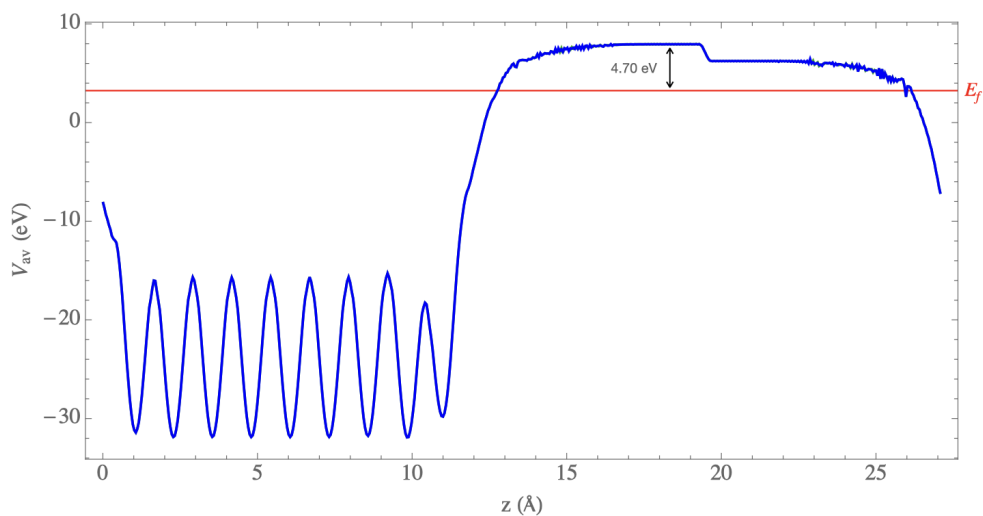


Figure D.4: SCAN+rVV10 computed work function for the C(110)-(1 $\times$ 1)H+2H<sub>v</sub>-AFM surface. The average potential in  $z$ -direction is represented by the blue line; while the Fermi level  $E_F$  is represented by the horizontal red line.

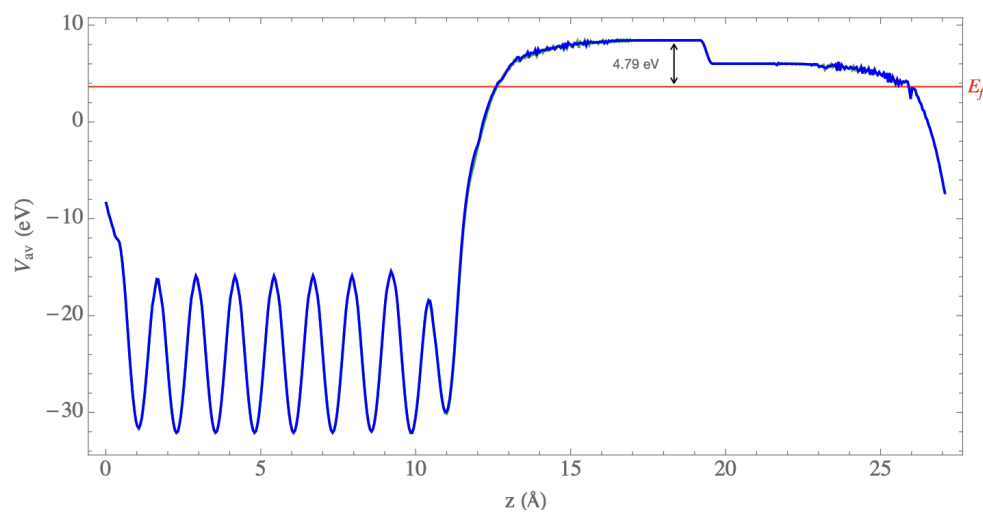


Figure D.5: SCAN+rVV10 computed work function for the C(110)-(1 $\times$ 1)H+3H<sub>v</sub>-M1 surface. The average potential in  $z$ -direction is represented by the blue line; while the Fermi level  $E_F$  is represented by the horizontal red line.

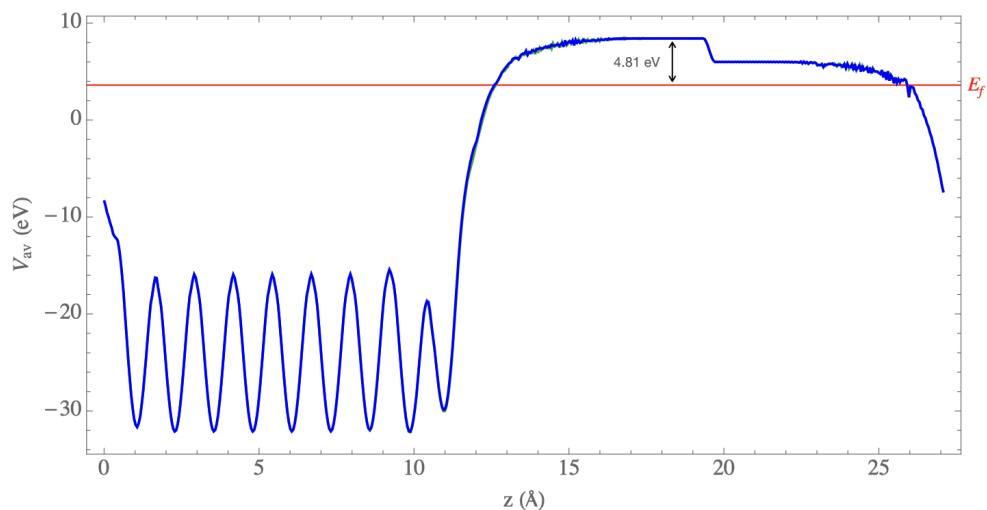


Figure D.6: SCAN+rVV10 computed work function for the C(110)-(1×1)H+3H<sub>v</sub>-M2 surface. The average potential in  $z$ -direction is represented by the blue line; while the Fermi level  $E_F$  is represented by the horizontal red line.

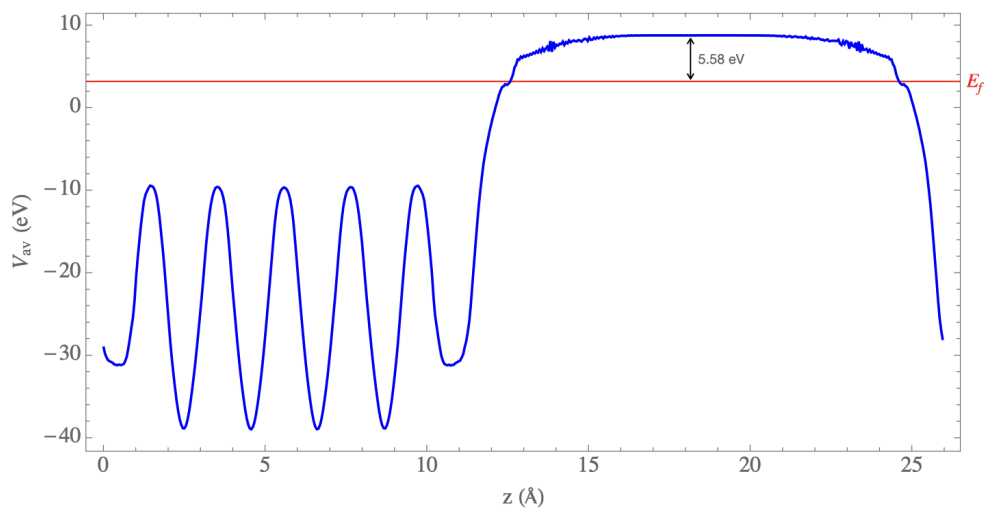


Figure D.7: SCAN+rVV10 computed work function for the C(111)-(2×1) surface. The average potential in  $z$ -direction is represented by the blue line; while the Fermi level  $E_F$  is represented by the horizontal red line.

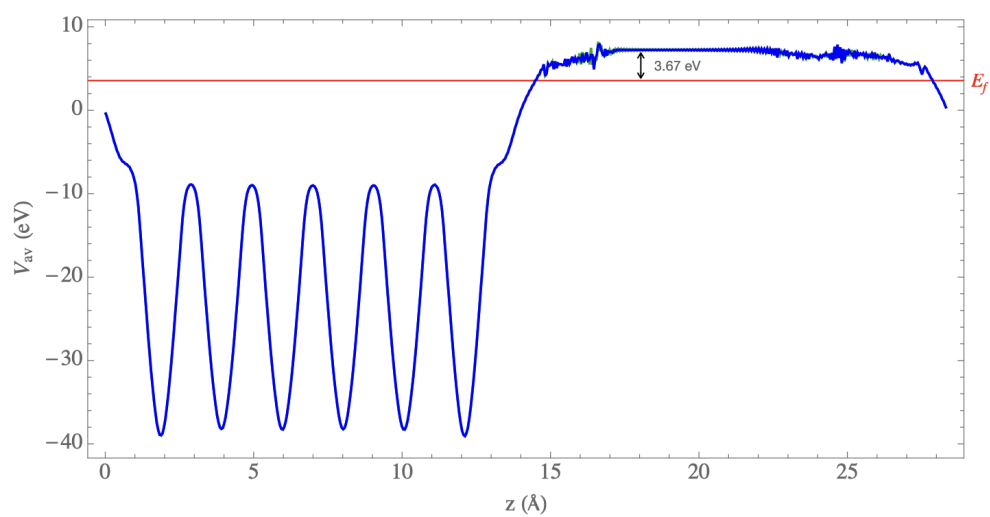


Figure D.8: SCAN+rVV10 computed work function for the C(111)-(1 $\times$ 1)H surface. The average potential in  $z$ -direction is represented by the blue line; while the Fermi level  $E_F$  is represented by the horizontal red line.



## Appendix E

# Computed PDOS for all the selected surfaces

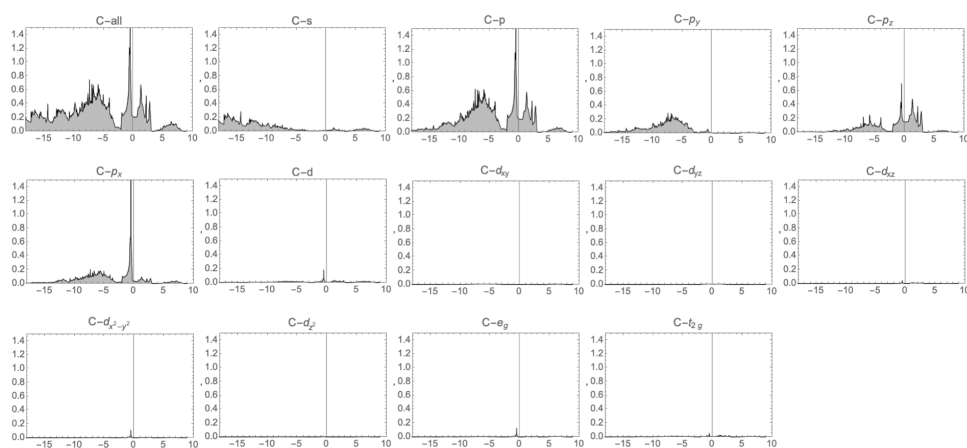


Figure E.1: Detailed PDOS for the C(110)-(1 $\times$ 1) surface computed with SCAN+rVV10. The horizontal axis is the  $E - E_F$  (eV), and the vertical axis are the states/eV.

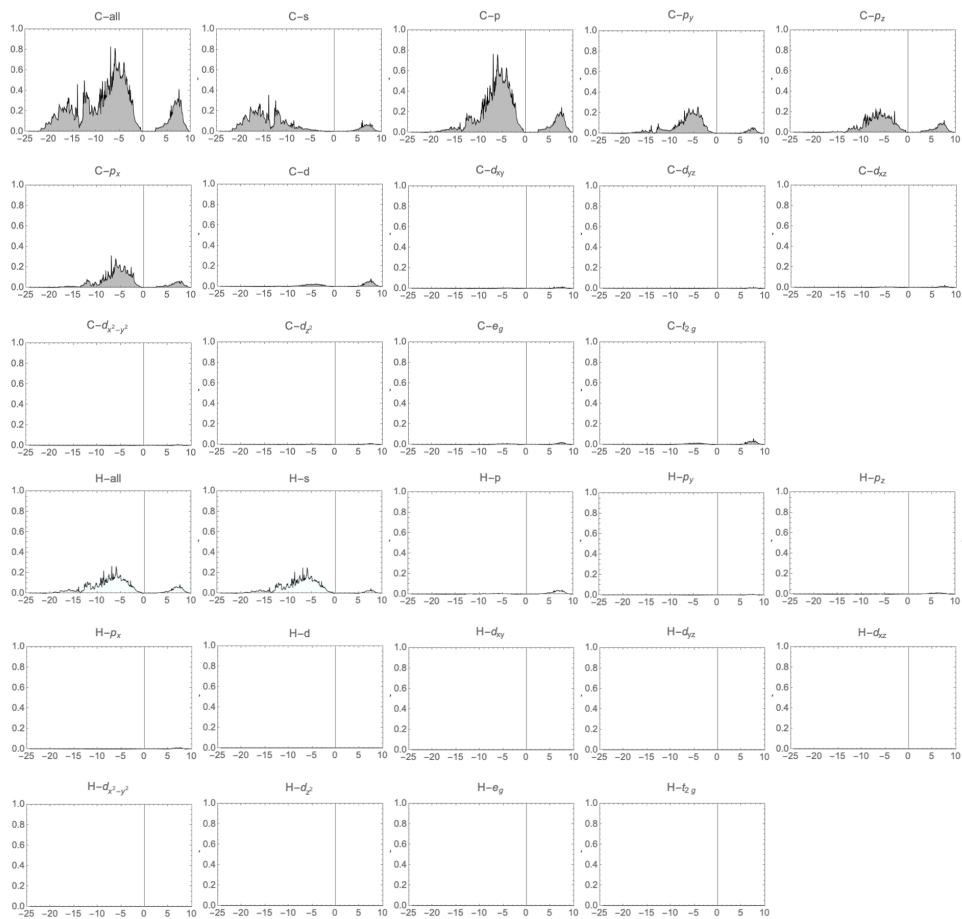


Figure E.2: Detailed PDOS for the C(110)-(1 $\times$ 1)H surface computed with SCAN+rVV10. The horizontal axis is the  $E - E_F$  (eV), and the vertical axis are the states/eV.

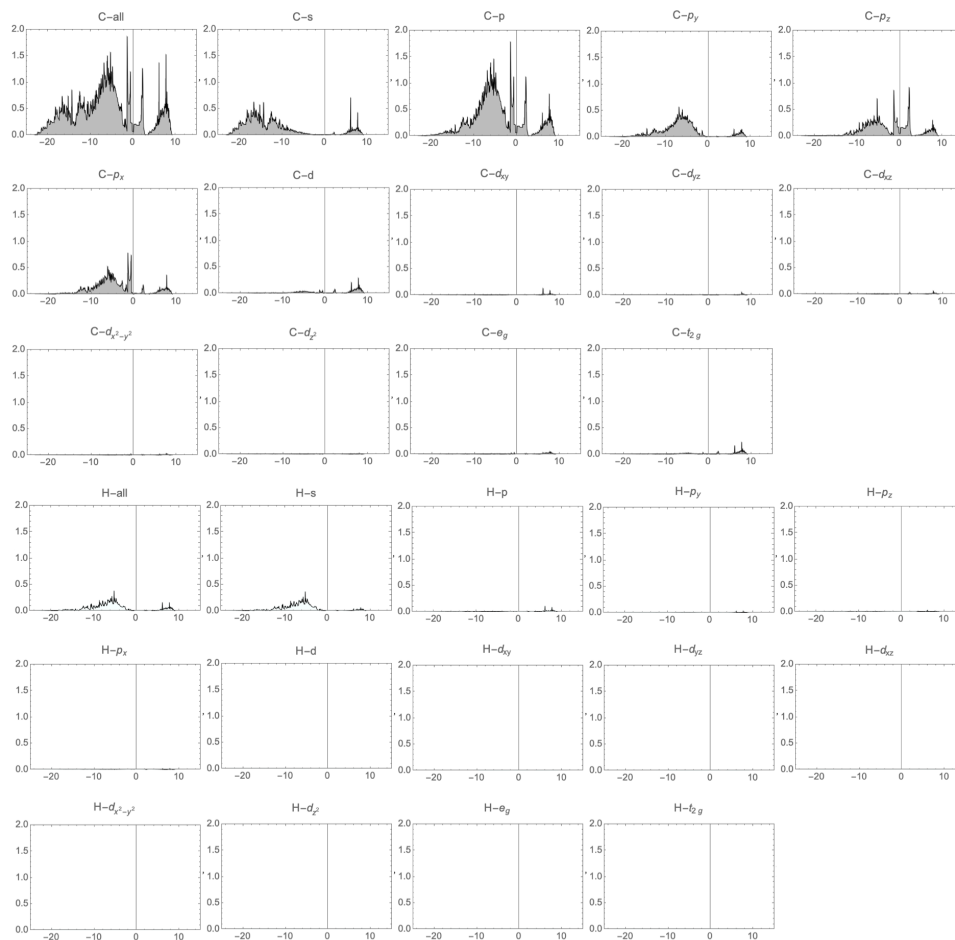


Figure E.3: Detailed PDOS for the C(110)-(1×1)H+2H<sub>v</sub> surface computed with SCAN+rVV10. The horizontal axis is the  $E - E_F$  (eV), and the vertical axis are the states/eV.

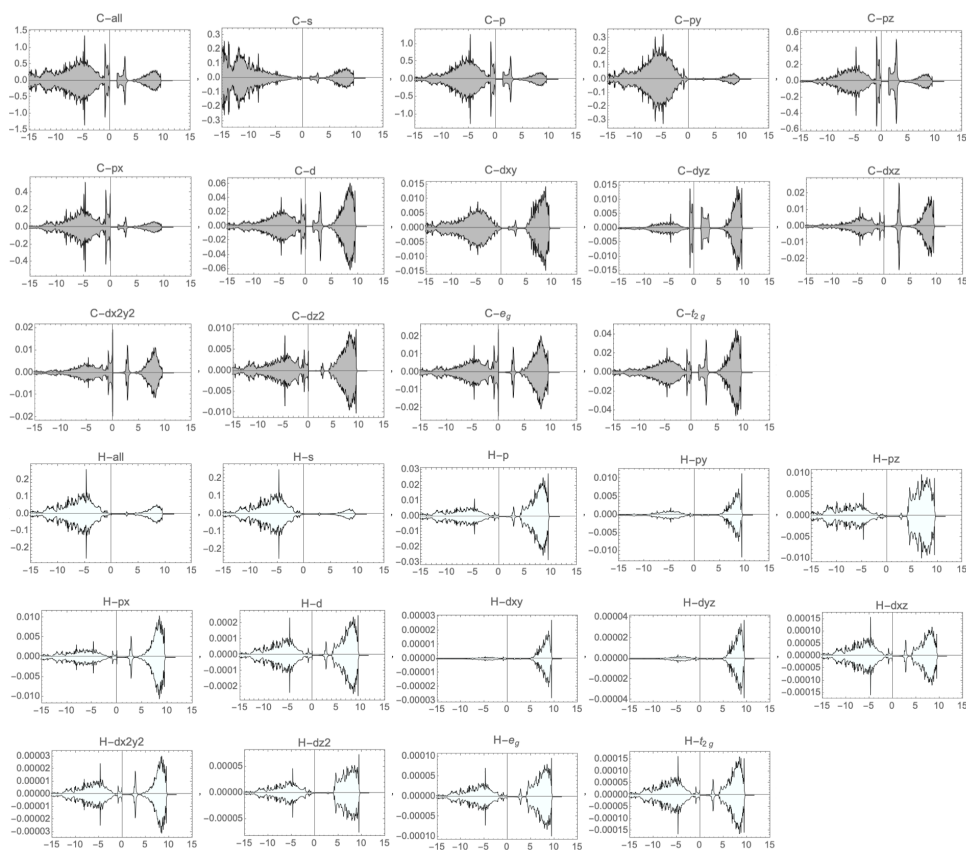


Figure E.4: Detailed PDOS for the C(110)-(1 $\times$ 1)H+2H<sub>v</sub>-AFM surface computed with SCAN+rVV10. The horizontal axis is the  $E - E_F$  (eV), and the vertical axis are the states/eV.



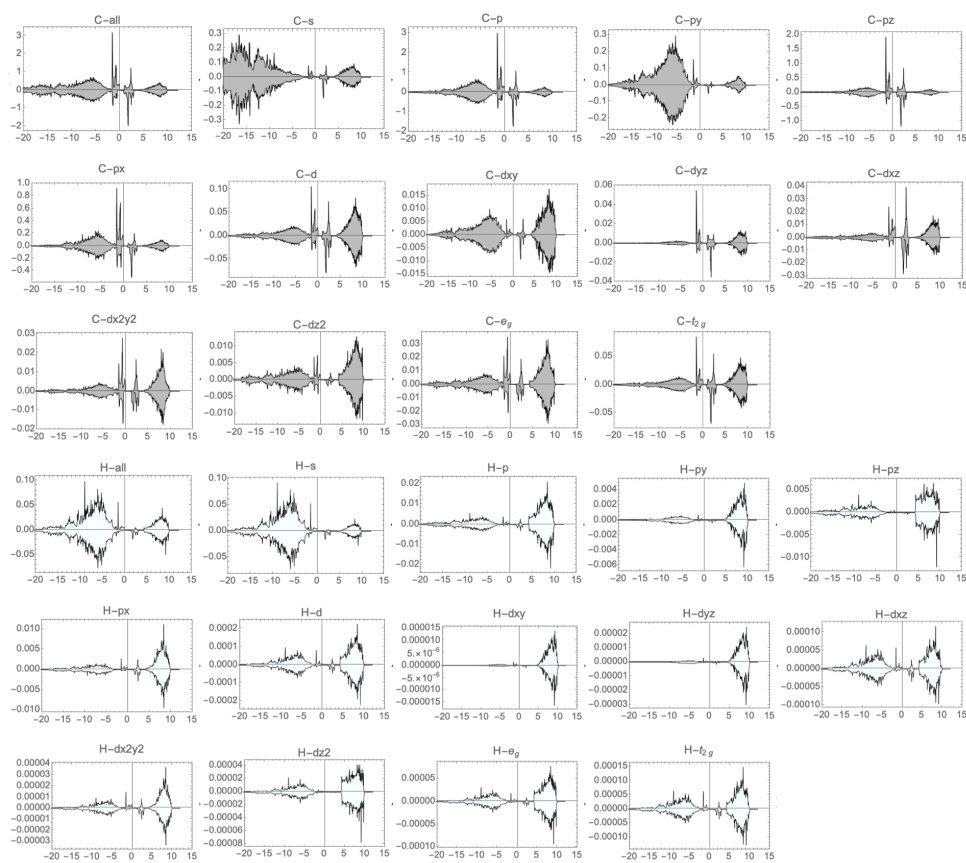


Figure E.5: Detailed PDOS for the C(110)-(1 $\times$ 1)H+3H<sub>v</sub>-M1 surface computed with SCAN+rVV10. The horizontal axis is the  $E - E_F$  (eV), and the vertical axis are the states/eV.

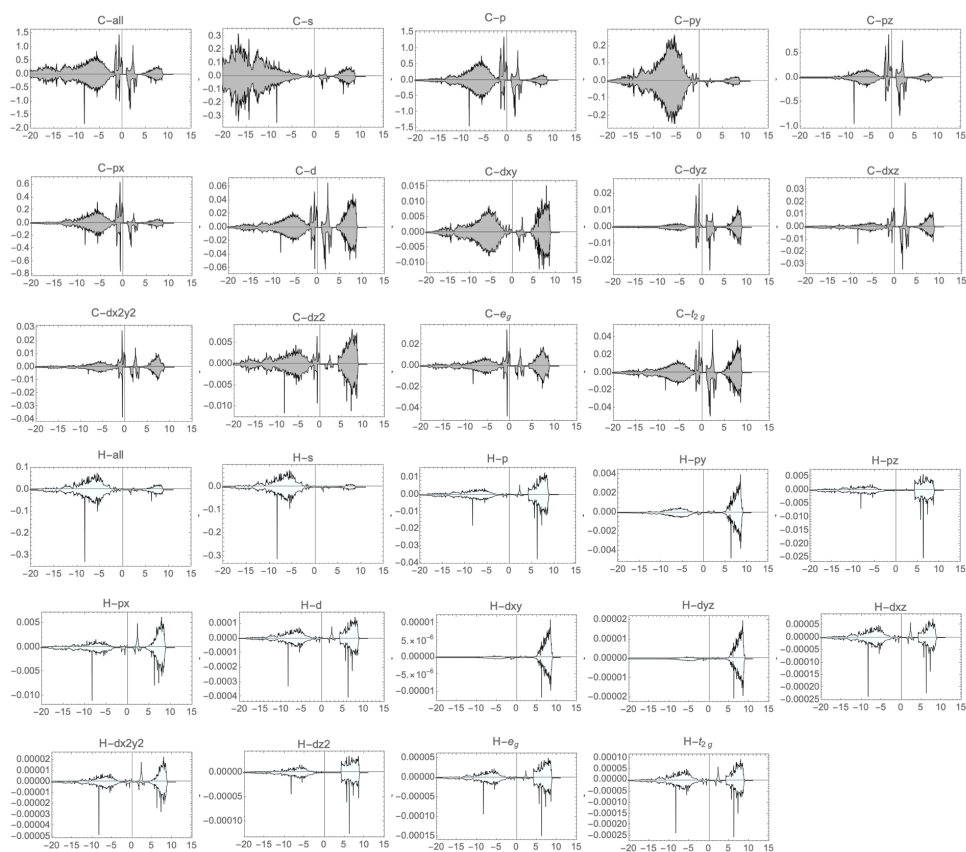


Figure E.6: Detailed PDOS for the C(110)-(1 $\times$ 1)H+3H<sub>v</sub>-M2 surface computed with SCAN+rVV10. The horizontal axis is the  $E - E_F$  (eV), and the vertical axis are the states/eV.

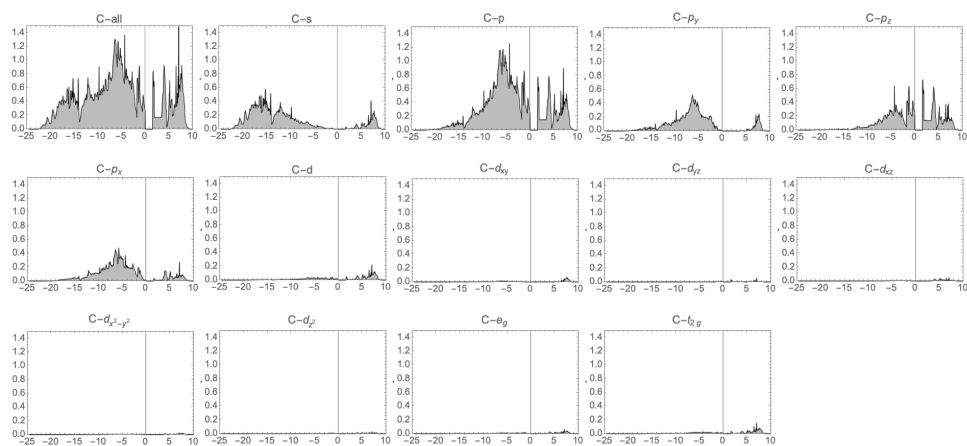


Figure E.7: Detailed PDOS for the C(111)-(2x1) surface computed with SCAN+rVV10. The horizontal axis is the  $E - E_F$  (eV), and the vertical axis are the states/eV.

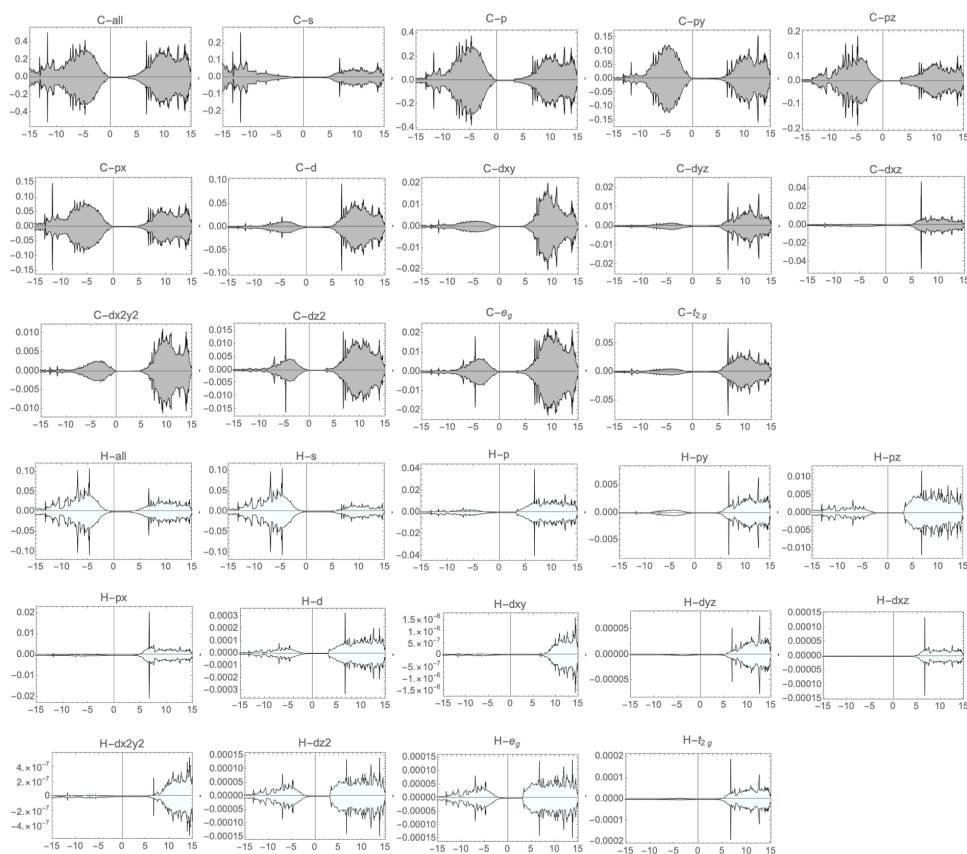


Figure E.8: Detailed PDOS for the C(111)-(1 $\times$ 1)H surface computed with SCAN+rVV10. The horizontal axis is the  $E - E_F$  (eV), and the vertical axis are the states/eV.

## Appendix F

# IMFP and Cross-section used for UPS spectra simulations

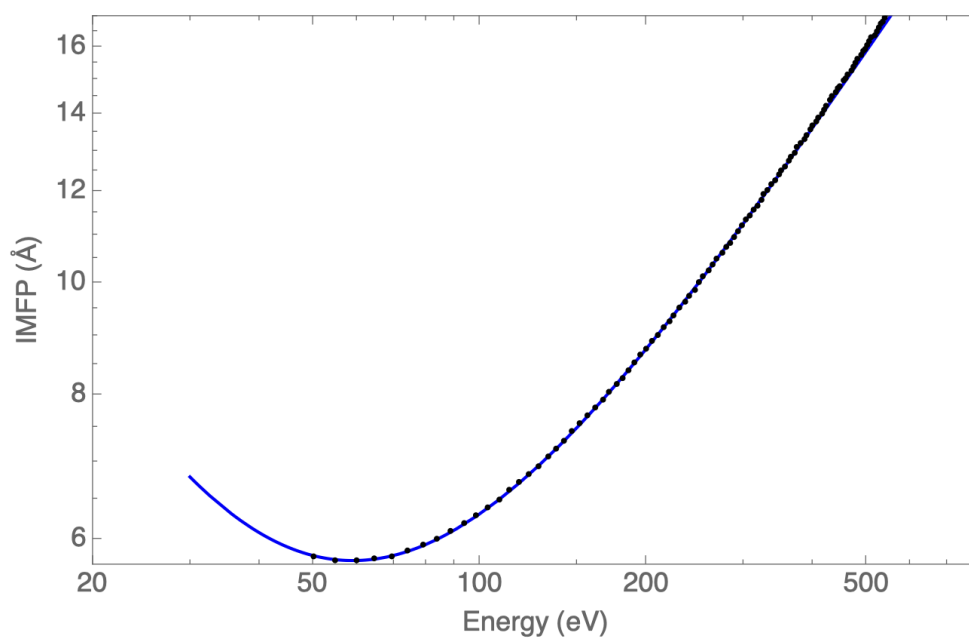


Figure F.1: Inelastic mean free path (IMFP) fitting for the data obtained from NIST software<sup>51</sup>.

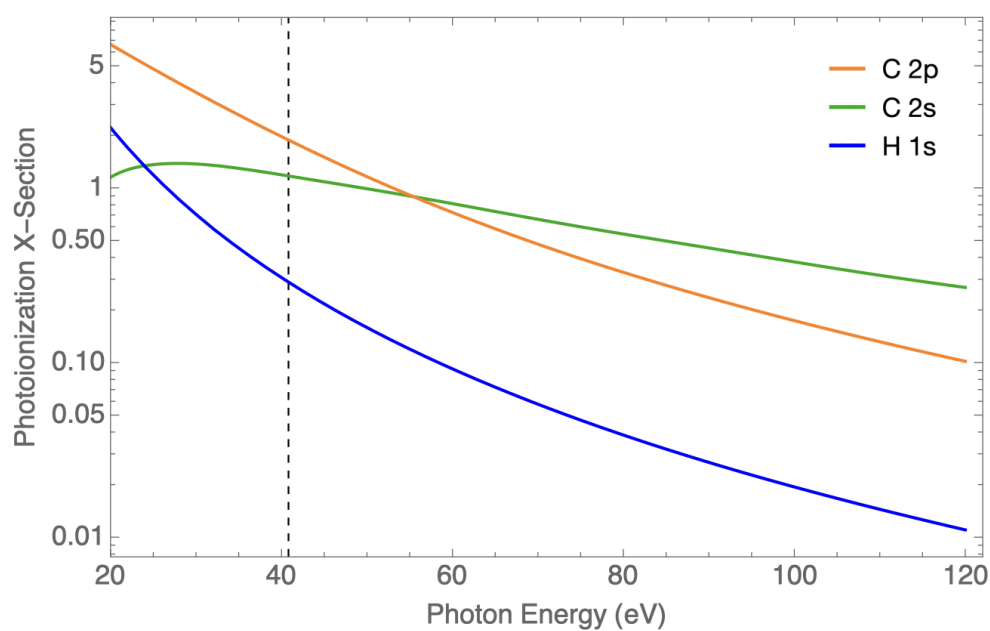


Figure F.2: Photoionization cross-section interpolations for the C and H atoms. The vertical dashed line is located at 40.82 eV, which is the energy used to simulate the UPS spectra. The data used in this interpolation was taken from Yeh and Lindau<sup>43</sup>.

# Bibliography

- [1] Gogotsi, Y. *Nanomaterials handbook*; CRC press, 2017.
- [2] Arnault, J.-C. *Nanodiamonds: advanced material analysis, properties and applications*; William Andrew, 2017.
- [3] Williams, O. A.; Hees, J.; Dieker, C.; Jäger, W.; Kirste, L.; Nebel, C. E. Size-dependent reactivity of diamond nanoparticles. *ACS nano* **2010**, *4*, 4824–4830.
- [4] Lin, B.-R.; Kunuku, S.; Chen, C.-H.; Chen, T.-Y.; Hsiao, T.-Y.; Yu, H.-K.; Chang, Y.-J.; Liao, L.-C.; Niu, H.; Lee, C.-P. Fluorescent Fe embedded magnetic nanodiamonds made by ion implantation. *Scientific reports* **2019**, *9*, 1–6.
- [5] Krueger, A.; Stegk, J.; Liang, Y.; Lu, L.; Jarre, G. Biotinylated nanodiamond: simple and efficient functionalization of detonation diamond. *Langmuir* **2008**, *24*, 4200–4204.
- [6] Liang, Y.; Ozawa, M.; Krueger, A. A general procedure to functionalize agglomerating nanoparticles demonstrated on nanodiamond. *ACS nano* **2009**, *3*, 2288–2296.
- [7] Mardirossian, N.; Head-Gordon, M. Thirty years of density functional theory in computational chemistry: an overview and extensive assessment of 200 density functionals. *Molecular Physics* **2017**, *115*, 2315–2372.
- [8] Giustino, F. *Materials Modelling using Density Functional Theory: Properties and Predictions*; Oxford University Press, 2014.
- [9] Groß, A. *Theoretical Surface Science: A Microscopic Perspective*, 2nd ed.; Springer-Verlag Berlin Heidelberg, 2009.

- [10] Martin, R. M. *Electronic Structure: Basic Theory and Practical Methods, 2nd Edition*, 2nd ed.; Cambridge University Press, 2020.
- [11] Born, M.; Oppenheimer, R. Zur quantentheorie der molekeln. *Annalen der physik* **1927**, *389*, 457–484.
- [12] Hohenberg, P.; Kohn, W. Inhomogeneous electron gas. *Physical review* **1964**, *136*, B864.
- [13] Kohn, W.; Vashishta, P. General density functional theory. *Theory of the Inhomogeneous Electron gas* **1983**, 79–147.
- [14] von Barth, U.; Hedin, L. A local exchange-correlation potential for the spin polarized case. i. *Journal of Physics C: Solid State Physics* **1972**, *5*, 1629.
- [15] Kubler, J.; Hock, K.-H.; Sticht, J.; Williams, A. Density functional theory of non-collinear magnetism. *Journal of Physics F: Metal Physics* **1988**, *18*, 469.
- [16] Perdew, J. P.; Ruzsinszky, A.; Tao, J.; Staroverov, V. N.; Scuseria, G. E.; Csonka, G. I. Prescription for the design and selection of density functional approximations: More constraint satisfaction with fewer fits. *The Journal of chemical physics* **2005**, *123*, 062201.
- [17] Sun, J.; Furness, J. W.; Zhang, Y. *Mathematical Physics in Theoretical Chemistry*; Elsevier, 2019; pp 119–159.
- [18] Perdew, J. P.; Kurth, S. *A primer in density functional theory*; Springer, 2003; pp 1–55.
- [19] Perdew, J. P.; Yue, W. Accurate and simple density functional for the electronic exchange energy: Generalized gradient approximation. *Physical review B* **1986**, *33*, 8800.
- [20] Perdew, J. P.; Kurth, S.; Zupan, A.; Blaha, P. Accurate density functional with correct formal properties: A step beyond the generalized gradient approximation. *Physical review letters* **1999**, *82*, 2544.
- [21] Becke, A. D. A new inhomogeneity parameter in density-functional theory. *The Journal of chemical physics* **1998**, *109*, 2092–2098.
- [22] Becke, A. Hartree–Fock exchange energy of an inhomogeneous electron gas. *International journal of quantum chemistry* **1983**, *23*, 1915–1922.



- [23] Sun, J.; Ruzsinszky, A.; Perdew, J. P. Strongly constrained and appropriately normed semilocal density functional. *Physical review letters* **2015**, *115*, 036402.
- [24] others., *et al.* Accurate first-principles structures and energies of diversely bonded systems from an efficient density functional. *Nature chemistry* **2016**, *8*, 831.
- [25] Neil W.(Neil W. Ashcroft) Ashcroft, N. D. M. *Solid state physics*, 1st ed.; Solid State Physics; Holt, Rinehart and Winston, 1976.
- [26] Kittel, C. *Introduction to Solid State Physics*, 8th ed.; Wiley, 2005.
- [27] Simon, S. H. *The Oxford Solid State Basics*; Oxford University Press, 2013.
- [28] Sholl, D.; Steckel, J. A. *Density functional theory: a practical introduction*; John Wiley & Sons, 2011.
- [29] Brázdová, V.; Bowler, D. R. *Atomistic computer simulations: a practical guide*; John Wiley & Sons, 2013.
- [30] Monkhorst, H. J.; Pack, J. D. Special points for Brillouin-zone integrations. *Physical review B* **1976**, *13*, 5188.
- [31] Blöchl, P. E. Projector augmented-wave method. *Physical review B* **1994**, *50*, 17953.
- [32] Kantorovich, L. *Quantum theory of the solid state: an introduction*; Springer Science & Business Media, 2004; Vol. 136.
- [33] Hafner, J. Ab-initio simulations of materials using VASP: Density-functional theory and beyond. *Journal of computational chemistry* **2008**, *29*, 2044–2078.
- [34] Kresse, G.; Joubert, D. From ultrasoft pseudopotentials to the projector augmented-wave method. *Physical review b* **1999**, *59*, 1758.
- [35] Binnig, G.; Rohrer, H.; Gerber, C.; Weibel, E. Surface studies by scanning tunneling microscopy. *Physical review letters* **1982**, *49*, 57.
- [36] Voigtländer, B. *Scanning probe microscopy: Atomic force microscopy and scanning tunneling microscopy*; Springer, 2015.

- [37] Liu, M. *Controlled Synthesis and Scanning Tunneling Microscopy Study of Graphene and Graphene-Based Heterostructures*; Springer, 2017.
- [38] Lab, H. STM: more technical details. 2010; <http://hoffman.physics.harvard.edu/research/STMtechnical.php>.
- [39] Griffiths, D. J. *Introduction to Quantum Mechanics*, 2nd ed.; Pearson Prentice Hall, 2004.
- [40] Andrew M. Ellis, T. G. W., Miklos Feher *Electronic and photoelectron spectroscopy: fundamentals and case studies*; Cambridge University Press, 2005.
- [41] Atkins, P. *Atkins' Physical Chemistry*, 8th ed.; Oxford University Press, 2006.
- [42] Schaible, M. J.; Pinto, H. P.; McKee, A. D.; Leszczynski, J.; Orlando, T. M. Characterization and Simulation of Natural Pyrite Surfaces: A Combined Experimental and Theoretical Study. *The Journal of Physical Chemistry C* **2019**, *123*, 26397–26405.
- [43] Yeh, J.; Lindau, I. Atomic subshell photoionization cross sections and asymmetry parameters: 1 Z 103. *Atomic data and nuclear data tables* **1985**, *32*, 1–155.
- [44] Yeh, J. Atomic Calculation of Photoionization Cross-Section and Asymmetry Parameters Gordon and Breach Science Publishers. *Langhorne, PE (USA)* **1993**,
- [45] VASP, Vienna Ab initio Simulation Package. <https://www.vasp.at/>.
- [46] Hofer, W. A Guide to simulation of STM images and spectra from first principles: bSKAN 3.6. *Surface Science Research Centre, The University of Liverpool, Liverpool, UK* **2005**, 60.
- [47] Tyuterev, V.; Vast, N. Murnaghan's equation of state for the electronic ground state energy. *Computational materials science* **2006**, *38*, 350–353.
- [48] Łodziana, Z.; Topsøe, N.-Y.; Nørskov, J. K. A negative surface energy for alumina. *Nature materials* **2004**, *3*, 289–293.
- [49] Sen, F. G.; Qi, Y.; Alpas, A. T. Surface stability and electronic structure of hydrogen-and fluorine-terminated diamond surfaces: A first principles investigation. *Journal of Materials Research* **2009**, *24*, 2461–2470.
- [50] Reuter, K.; Scheffler, M. Composition, structure, and stability of RuO<sub>2</sub> (110) as a function of oxygen pressure. *Physical Review B* **2001**, *65*, 035406.

- [51] Jablonski, A.; Powell, C. J. NIST Electron Inelastic-Mean-Free-Path Database. *National Institute of Standards and Technology, Gaithersburg* **2010**,
- [52] Zemann, J. Crystal structures, Vol. 1 by RWG Wyckoff. *Acta Crystallographica* **1965**, *18*, 139–139.
- [53] Tse, J. S.; Holzappel, W. B. Equation of state for diamond in wide ranges of pressure and temperature. *Journal of Applied Physics* **2008**, *104*, 043525.
- [54] Francz, G.; Kania, P.; Gantner, G.; Stupp, H.; Oelhafen, P. Photoelectron spectroscopy study of natural (100),(110),(111) and CVD diamond surfaces. *physica status solidi (a)* **1996**, *154*, 91–108.
- [55] Pandey, K. New dimerized-chain model for the reconstruction of the diamond (111)-(2× 1) surface. *Physical Review B* **1982**, *25*, 4338.
- [56] Jones, L.; Wang, S.; Hu, X.; ur Rahman, S.; Castell, M. R. Maximising the resolving power of the scanning tunneling microscope. *Advanced structural and chemical imaging* **2018**, *4*, 1–8.
- [57] VASP, INCAR. <https://www.vasp.at/wiki/index.php/INCAR>.
- [58] VASP, POTCAR. <https://www.vasp.at/wiki/index.php/POTCAR>.
- [59] VASP, POSCAR. <https://www.vasp.at/wiki/index.php/POSCAR>.
- [60] VASP, KPOINTS. <https://www.vasp.at/wiki/index.php/KPOINTS>.
- [61] VASP, CONTCAR. <https://www.vasp.at/wiki/index.php/CONTCAR>.
- [62] VASP, CHGCAR. <https://www.vasp.at/wiki/index.php/CHGCAR>.
- [63] VASP, CHG. <https://www.vasp.at/wiki/index.php/CHG>.
- [64] VASP, DOSCAR. <https://www.vasp.at/wiki/index.php/DOSCAR>.
- [65] VASP, OUTCAR. <https://www.vasp.at/wiki/index.php/OUTCAR>.
- [66] VASP, OSZICAR. <https://www.vasp.at/wiki/index.php/OSZICAR>.
- [67] VASP, WAVECAR. <https://www.vasp.at/wiki/index.php/WAVECAR>.